Modelling of hydrogen diffusion in heterogeneous materials : implications of the grain boundary connectivity

Bachir Osman Hoch

Université de La Rochelle

Laboratoire des Sciences de l'Ingénieur pour l'Environnement

UMR 7356

ÉCOLE DOCTORALE
SI-MMEA

Laboratoire des Sciences de l'Ingénieur pour l'Environnement

THÈSE

présentée par :

Bachir OSMAN HOCH

soutenue le **11 décembre 2015**

pour l'obtention du grade de Docteur de l'Université de La Rochelle

Discipline : ***Science et Génie des Matériaux***

Modelling of hydrogen diffusion in heterogeneous materials: implications of the grain boundary connectivity

Modélisation de la diffusion de l'hydrogène dans les matériaux hétérogènes: implications de la connectivité des joints de grains

---

Jury

Vigdis OLDEN	Senior Researcher, SINTEF Norway	Rapporteure
Monique GASPERINI	Professeure, LSPM, Université Paris 13	Rapporteure
Dongsheng LI	Professeur, Washington State University	Examinateur
Thierry COUVANT	Docteur ingénieur de recherche EDF, MMC	Examinateur
François WILLOT	Chargé de recherche, CMM-MS, Mines ParisTech	Examinateur
Arnaud METSUE	MCF, LaSIE, Université de La Rochelle	Examinateur
Xavier FEAUGAS	Professeur, LaSIE, Université de La Rochelle	Directeur de thèse
Jamaa BOUHATTATE	MCF, LaSIE, Université de La Rochelle	Co-Directrice de thèse

"*Crystals are like people, it is the defects in them which tend to make them interesting!*"

Colin Humphreys

Acknowledgements

First of all, I would like thank all the committee members and more particularly Dr. Vigdis Olden and Pr. Monique Gasperini who accepted to review this dissertation and contributed to its improvement. I would like to express my gratitude to Pr. Dongsheng Li who traveled a considered distance and made me the honor to chair the examination jury.

Then I would like to thank my advisors Xavier Feaugas and Jamaa Bouhattate who gave me the opportunity to work on such beautiful subject. I would like to express my sincere gratitude to both of you for your scientific guidance and more particularly for your availabilities despite your busy timetables. Xavier, it is really inspiring and rewarding to work with you.

I would like to express my deepest gratitude to Arnaud Metsue who helped me continuously and contributed so much to the improvement of this dissertation. You showed me the importance of the scientific rigor. It is thank to you also that I learned to open a terminal and handle with the "./ " without problems [Arnaud 2010].

I would like to thank Esaïe Legrand and Abdelali Oudriss who were most closely involved in this work. It has been a pleasure working with you guys. I would like to thank also Egle Conforto for her help and patience during the EBSD serial-scanning sessions.

I had a great time working in the LaSIE lab and I would like to thank all the colleagues for their kindness. I would like to give my special thanks to the past and present PhD students. I particularly want to thank Yves, Daniella, Alaric, Niusha, Felana, Coralie, Alexandre, Loic and the others. Quoting all of you would be too long, but I had wonderful moments with you in La Rochelle.

Last but not the least, I would like to thank my family and friends who were far from me but continuously encouraged me. I would like to dedicate this thesis to my mother Amina Omar who dedicated her life for its children. It is largely thanks to her if I went to school and achieved all of this.

Table of content

Chapter 1

General introduction

Introduction

In the context of today's energy crisis and the rapid climate change, hydrogen is seen as a clean, mobile energy carrier and source of fuel. A genuine 'hydrogen economy' is henceforth envisaged because this element has the great advantage of being present on the planet in endless quantity. However, there are still many obstacles to overcome before seeing a real hydrogen economy similar to the electricity economy. Some of these challenges include the development of suitable materials to the transportation of hydrogen. Indeed, a major concern with hydrogen is that it is very detrimental to the durability of materials. This problem has persisted for a while and affects the structural materials in various industries, from subsea pipelines to aircraft and nuclear reactors.

Indeed, the presence of some hydrogen in the metal can lead to a severe degradation of its mechanical properties. This degradation can manifest itself in several ways such as a decrease in tensile elongation to cause fracture, or a decrease in the static load that can be supported by the metal as an example. This phenomenon, known as hydrogen embrittlement (HE), results from a combination of different parameters related to the material characteristics, the source of the hydrogen (internal or external) and to the mechanical solicitations, as illustrated in Fig. 1. HE has been studied for several decades and several HE models have been proposed for crystalline materials **[Barnoush 2011]**. But, these models are generally focused on the upstream process, i.e. the embrittlement mechanism itself. However, to fully understand the HE phenomenon, it also important to study the downstream process, which is the transport processes involved in moving the hydrogen from its source to the locations where it reacts with the metal to cause the embrittlement.

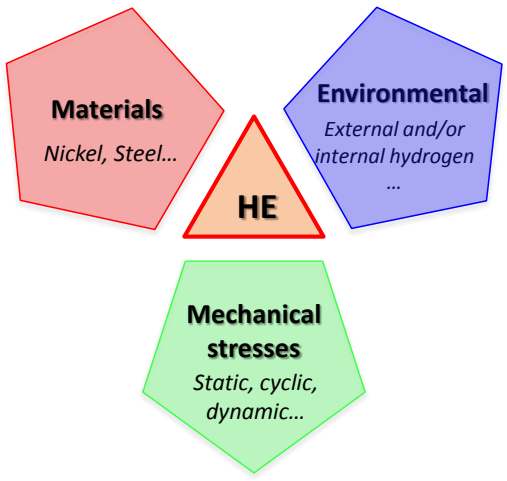

Fig. 1 - Hydrogen embrittlement due to three combined factors

Experimental data on the hydrogen diffusion and segregation in materials suffer from inconsistencies, especially the hydrogen diffusivity values in the low temperature regions **[Kiuchi**

1983]. The causes of these anomalies include the effects of microstructural defects, such as grain boundaries, dislocations or vacancies on the hydrogen transport in materials **[Kiuchi 1983, Palumbo 1991a]**. A number of studies have pointed out the determining role of grain boundaries in the hydrogen diffusion and trapping mechanisms. However, despite the large amount of work on the subject, the contribution of grain boundaries the effective diffusivity in polycrystals remains unclear. The acceleration of hydrogen diffusion along grain boundaries has been reported in several studies **[Harris 1991, Brass 1996, Oudriss 2012b]**. But, it has been suggested also that grain boundaries can reduce the overall hydrogen diffusivity under certain conditions **[Yao 1991]**. Since effective diffusivity is measured in a heterogeneous aggregate with a mixture of microstructure features, it is difficult to separate the contribution of all the microstructural parameters in the diffusion process.

Additional difficulties come from the existence of the large variety of grain boundaries and the complexity of their structure. Few studies have considered the implications of this heterogeneity of grain boundaries on hydrogen diffusion and segregation in polycrystalline materials. Recently, Oudriss *et al*. have shown that the boundary nature remarkedly influence the hydrogen diffusion and segregation, by combining diffusion measurements and microstructure characterization of polycrystalline nickel **[Oudriss 2012b]**. In addition to the boundary nature, they pointed out that the importance of taking into account the connectivity of boundaries with different characters to better describe the effects of grain boundaries on the overall diffusion. However, the studies on the correlations between the overall hydrogen diffusion and the grain-boundary character distribution are rare, even-nonexistent. This is mainly due to the experimental difficulties to explore the grain-boundary diffusion in polycrystalline materials.

In parallel, numerical approaches can bring insights of the correlations between grain-boundary character and the overall hydrogen diffusion process. To do so, it is necessary to combine different modeling tools at different scales, as shown in Fig. 2, in order to fully understand these effects. Atomistic models such as first principles calculations (DFT) or molecular dynamics can be used to study the hydrogen diffusion in individual well characterized grain boundaries, while continuum approach allows simulating hydrogen diffusion at mesoscopic and macroscopic scales.

The goal of this work is to investigate the effects of heterogeneous GB networks on the effective diffusivity in polycrystalline materials, using mainly a numerical approach based on finite elements modelling. This work is also aimed at investigating the effects of the boundary nature on the local hydrogen distribution, through an experimental analysis.

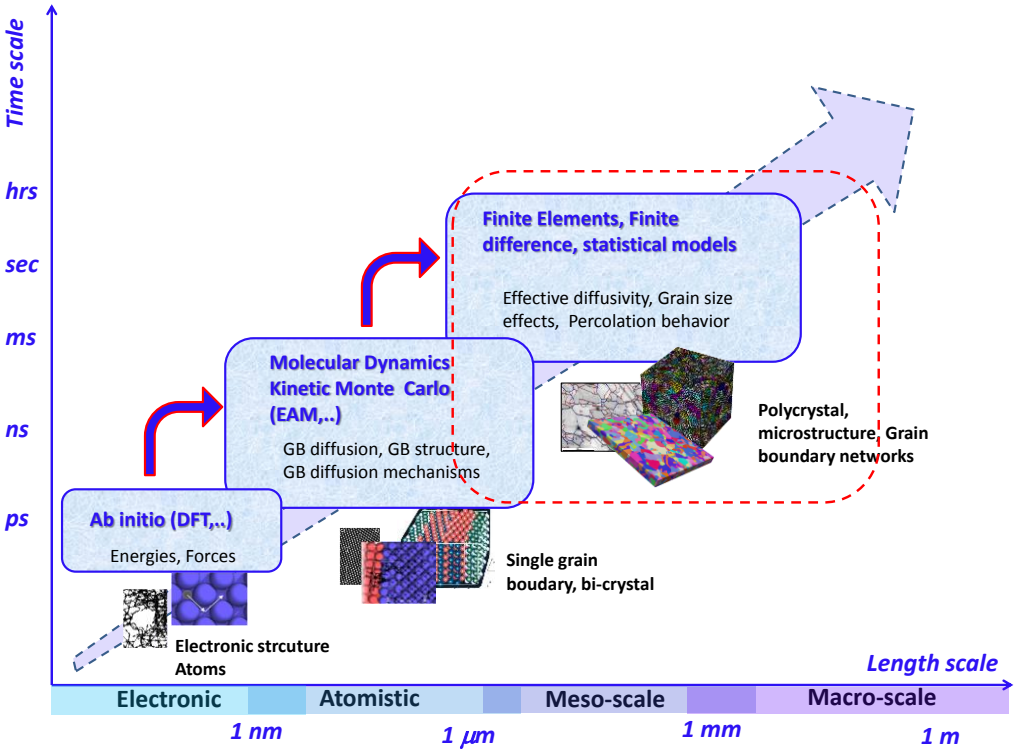

Fig. 2 - Numerical methods at different scales to investigate the diffusion in solids, the red dashed line indicates the scale considered in this work

The first part (chapter 2) of the present dissertation is aimed at providing a literature review on the hydrogen diffusion in polycrystalline materials and its interaction with microstructural defects. In particular, the role of grain boundaries in the hydrogen diffusion process is discussed. In a second part, we review the popular homogenization methods and the influence of grain-boundary connectivity on the effective material properties.

Then, we present in the third chapter a numerical study on the impact of grain-boundary connectivity on the effective diffusivity in two and three-dimensional simulated polycrystalline materials. The first part focuses on the characterization of the GB networks structure, by determining the topology and the connectivity parameters. Then, correlations between the effective diffusivity and the topology parameters of the GB networks are analyzed. In addition, the applicability of homogenization methods to predict the effective diffusivity, by considering percolation parameters, is discussed. Finally, the analysis is extended to three dimensional microstructures by using Kelvin polyhedron microstructure.

The fourth chapter of the present dissertation comprises two parts. In the first part, hydrogen diffusion is simulated on realistic microstructures based on EBSD maps. The results are discussed in regard of the GB connectivity and available experimental data. In the second part of this chapter, an

experimental study is conducted in order to understand the hydrogen segregation near grain-boundaries in polycrystalline pure nickel.

At the end of this thesis, a summary of key findings and conclusions based on the different analyses of this work are presented. Finally, different perspectives are proposed to improve the numerical approach and to move towards a multiphysics approach by coupling hydrogen diffusion and mechanical behavior.

Chapter 2

Literature review

In this chapter, I present a literature review on the hydrogen diffusion in polycrystalline materials and the effects of the microstructural defects, more particularly the grain boundaries. In the first part, after providing some background on the hydrogen embrittlement phenomenon, the hydrogen diffusion and trapping in polycrystalline materials are described. Then, fundamentals on grain boundaries and intergranular diffusion are presented. Finally, popular homogenization technics and the influence of grain-boundary connectivity on the material effective properties are reviewed.

I. Hydrogen-metal interactions

1. Generalities on hydrogen and hydrogen embrittlement

1.1. Hydrogen characteristics

Hydrogen, widely present as a water form in the earth, is one of the most abundant elements in the universe. This element is characterized by a high mobility in metals because of its small atomic size and its low mass **[Coudreuse 2000]**. In face-centered cubic (FCC) lattices, interstitial hydrogen generally prefers octahedral sites, while it is located on tetrahedral sites in body-centered cubic (BCC) and hexagonal close-packed (HCP) metals, at room temperature **[Wipf 1997]**. According to Wipf **[Wipf 2001]**, the distance between the two nearest octahedral sites for FCC metals, which is around 0.2 nm, is almost twice the distance between the two nearest tetrahedral sites in BCC lattices. As a result, the diffusivity of hydrogen is generally lower in FCC metals compared to BCC metals. In addition, the high partial volume of hydrogen can generate distortions in unstrained lattices **[Coudreuse 2000]**. Indeed, the interstitial hydrogen modifies the local electronic structure of the metal atoms, especially because of its ability to transfer all or some of its electric charge to its close neighbors. This modification may decrease the interatomic cohesion and can result in a possible embrittling effect **[Coudreuse 2000]**. This is one concept, among the several theories, developed to explain the hydrogen embrittlement (HE). Due to the complexity of the hydrogen-metal interactions and the nature of the surrounding environment, it is very difficult to formulate one concept or one theory of the HE phenomenon. However, most of the mechanisms can be classified in four major theories: Hydride-induced embrittlement, Hydrogen induced decohesion (HEDE), hydrogen induced plasticity and hydrogen-vacancy interactions.

1.2. Hydrogen embrittlement mechanisms

The hydride-induced embrittlement model, first proposed by Westlake **[Westlake 1969]**, suggests that cracking can occur by the formation of hydride near the crack tip. The hydride formation is associated with an oversaturation of hydrogen and is stabilized by the hydrostatic field at the stressed crack tip. Experiments demonstrated hydride embrittlement in niobium, titanium or zirconium **[Gahr 1977, Hirth 1980]** and some iron alloys such as austenitic steels **[Chene 1982]**. But this mechanism does not affect iron or ferritic alloys because the low hydrogen solubility does not enable hydride formation in these materials **[Coudreuse 2000]**.

The HEDE model was first introduced by Troiano and his co-workers **[Morlet 1958, Troiano 1960]** and developed by Oriani and Josephic **[Oriani 1972, Oriani 1974]**. The key point of this

mechanism is that hydrogen accumulates within the lattice and lessens the interatomic cohesion forces. The accumulation of hydrogen can be engendered by the lattice dilatation due to elastic hydrostatic stresses **[Oriani 1966]** or by trapping mechanisms which are the main origin of hydrogen segregation **[Pressouyre 1980]**. Basically, The HEDE theory postulates that cracking occurs when the local tensile stresses exceeds the maximum-local atomic cohesion strength, lowered by the presence of atomic hydrogen in the lattice, grain boundary or interfaces.

The hydrogen-dislocation interaction is the main process in the different mechanisms of the hydrogen induced plasticity theory. In the framework of this theory, two major mechanisms are generally advanced: Adsorption Induced Dislocation Emission (AIDE) **[Lynch 1988]** and the Hydrogen Enhanced Localized Plasticity (HELP) **[Beachem 1972]**. The AIDE mechanism states that the hydrogen adsorbed on the crack tip reduces the energy of dislocation formation, leading to the decrease of the stress required for the dislocations emission. As for the other mechanism, it is said that the dissolved hydrogen makes easier the dislocations mobility, which leads to a localized plastic deformation and to a decrease of the critical stress required for the crack initiation.

The Hydrogen-vacancy interaction approach, developed by Fukai, McLellan, Carr and their teams, is the most recent **[Fukai 1995, McLellan 1997, Fukai 2001, Carr 2004, Carr 2006]**. This approach is based on the hydrogen ability to create new vacancies called *Superabundant Vacancy* (SAV) and to stabilize them. This mechanism is supported by several experiments, showing vacancy concentration differences before and after hydrogen absorption **[Fukai 2001, Carr 2004, Carr 2006]**. It is suggested that the SAV vacancies formation is probably engendered by the interactions between absorbed hydrogen and the already present vacancies, mainly in grain boundaries. The multiplication of vacancies may lead to the formation of microcracks or microvoids **[Nagumo 2004, Takai 2008]**. It has been shown experimentally that the only presence of vacancies can be responsible of loss of ductility **[Takai 2008]**.

In all the mechanisms, cited above, hydrogen interactions with stress fields and microstructures play a crucial role in the embrittlement process **[Coudreuse 2000]**. However, despite the extensive studies on HE mechanisms, the kinetics associated with the diffusion and segregation of the hydrogen in metals, and their interactions with defects are not clearly understood.

2. Hydrogen diffusion in polycrystalline materials

A good knowledge of hydrogen transport and segregation in polycrystalline materials is necessary to fully understand HE mechanisms and to establish a good classification of materials according to their HE resistances. However, literature data on the solubility and diffusivity of hydrogen suffers

from inconsistencies and the role of lattice defects in the hydrogen transport is not well established **[Kiuchi 1983, Oudriss 2012a]**. From statistical analysis on literature data for the solubility and diffusivity of hydrogen in iron, Kiuchi and McLellan **[Kiuchi 1983]** have shown the existence of large degree of discrepancy at moderate and low temperatures, as represented in Fig. 3(a) and (b). As suggested by the authors, these discrepancies may due to the variety of applied technics but they also pointed out the role of H-defects interactions that are more pronounced at low temperatures.

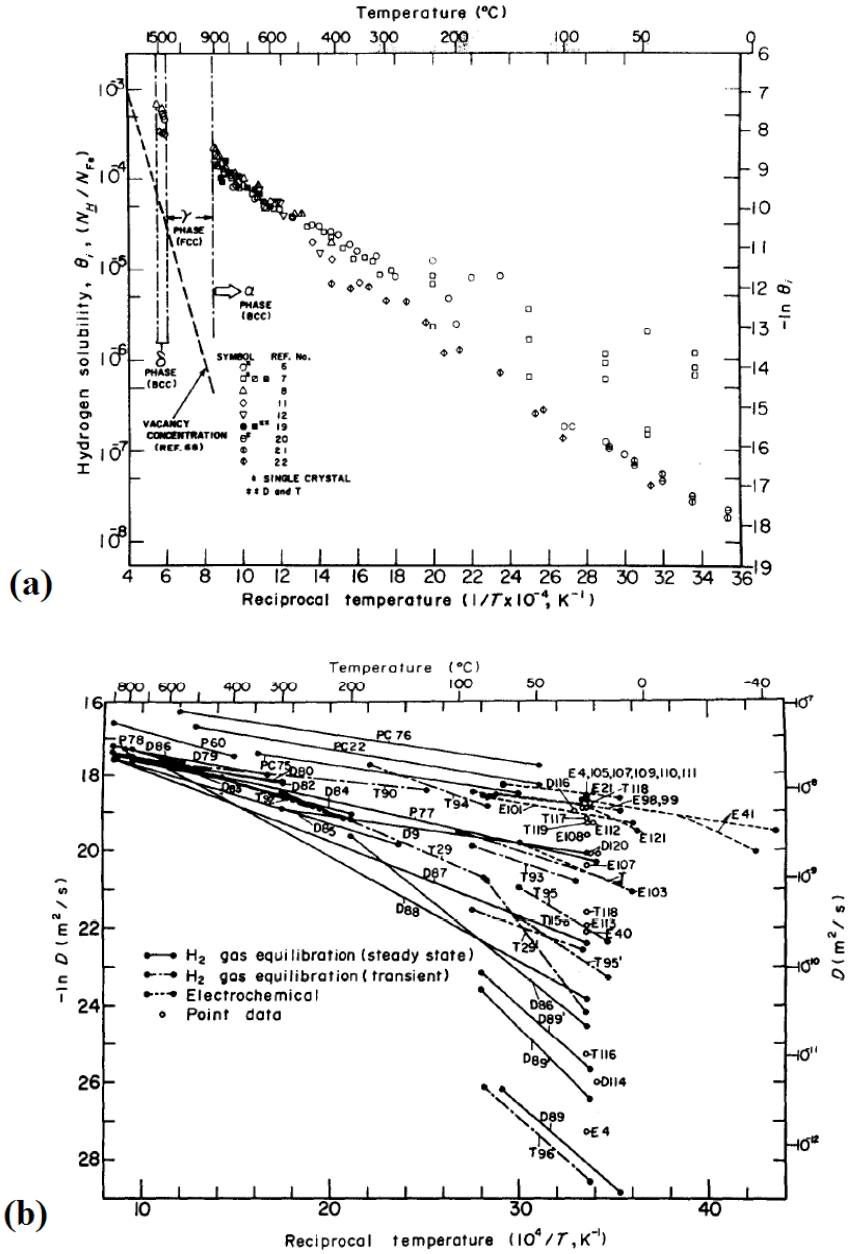

Fig. 3 - (a) Hydrogen solubility in bcc iron as a function of temperature. (b) Arrhenius representation of the data for the diffusion of hydrogen through bcc iron **[Kiuchi 1983]**.

In this section, we firstly introduce the permeation technics. These technics are the most used to determine the diffusion coefficient and the solubility of hydrogen in metals, in a wide range of pressure. Then, we review hydrogen interactions with defects in term of trapping phenomena.

2.1. Methods for characterizing hydrogen diffusion

2.1.1. Permeation technics

First developed by Devanathan and Stachurski in 1962 to quantify the hydrogen diffusion in palladium **[Devanathan 1962]**, permeation method has been widespread and applied to others materials **[Altunoglu 1996, Brass 1996, Zakroczymski 2006, Addach 2009, Frappart 2010]**. Generally, this method consists in measuring the hydrogen flux through a membrane subjected on one of its faces at a hydrogen pressure **[Brass 1996]**. The technic can be applied in different ways, depending on the objectives. In particular, hydrogen can be introduced into the metal either through a cathodic process (Electrochemical permeation) or by a gaseous charging (gaseous permeation).

Electrochemical permeation (EP)

The experimental set up is mainly composed of two cells: the charging cell and the detecting cell, separated by a thin metal membrane. Fig. 4 illustrates the electrochemical permeation mechanism, with the boundary electrochemical conditions. Hydrogen is generated on the surface of the metallic membrane by cathodic charging. The mechanism of introduction into the membrane occurs in two steps: hydrogen adsorption and hydrogen absorption. In the first phase, the cathodic polarization causes the reduction of H_20 or H_3O^+ and allows the hydrogen adsorption on the metal (M) surface, following equations (II.1) and (II.2) :

- In acid media : $$H_3O^+ + e^- + M \rightarrow H_2 0 + MH_{ads} \quad \text{(II.1)}$$
- In basic media : $$H_2O + e^- + M \rightarrow MH_{ads} + OH^- \quad \text{(II.2)}$$

Then, the absorption phase occurs by the entry of the atoms in the material, following equation (II.3):

$$MH_{ads} \rightarrow MH_{abs} \quad \text{(II.3)}$$

However, after the adsorption step, some hydrogen atoms can re-combine into dihydrogen (H_2). The absorbed hydrogen atoms diffuse through the metal and are immediately oxidized on the output surface, by applying sufficient anodic potential. Thus, a zero concentration boundary condition is created. However, the anodic polarization is not sufficient to oxidize all of the hydrogen coming out. Studies have shown the need for a palladium layer to have a better detection and avoid passivation **[Manolatos 1995]**.

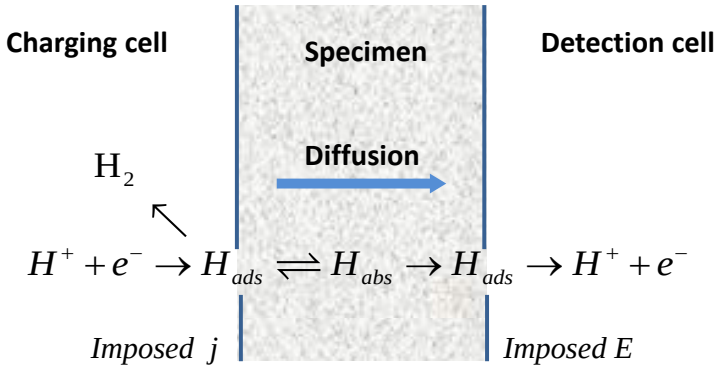

Fig. 4 - Electrochemical permeation mechanism.

From the oxidation of the coming out hydrogens, an evolution of current density as a function of time is obtained **[Brass 1996, Ly 2009, Frappart 2010]**. The hydrogen flux is proportional to this current density, following the relation (II.4):

$$J = \frac{N_A \times j}{nF} \tag{II.4}$$

With:

N_A Avogadro number ($6.02214479 \times 10^{-23}$ mol^{-1})

j Current density ($\mu A/cm^2$)

n Number of electrons in the reaction (n = 1)

F Faraday's constant (96485 $C.mol^{-1}$)

J Hydrogen flux ($at.cm^{-2}.s^{-1}$)

There are two stages in the permeation tests: the charging step and the desorption step, as illustrated in Fig. 5. The hydrogen flux increases until the steady-state is reached. Then, the hydrogen charging is stopped and desorption of diffusible hydrogen is obtained. In the desorption step, the hydrogen flux decreases and tends to zero. The hydrogen diffusion in metals is described by the Fick's laws:

1st Fick's law: $$\vec{J} = -D\overrightarrow{grad}(C) \tag{II.5}$$

2nd Fick's law: $$\frac{\partial C}{\partial t} = -div(D\overrightarrow{grad}(C)) \tag{II.6}$$

where J and C are respectively the hydrogen flux and the concentration. The hydrogen diffusion is governed by the local diffusion coefficient D, which depends particularly on the crystalline structure of the material and the temperature. From the flux curve in the charging step, one can calculate the

effective diffusion coefficient D_{eff} using a mathematical relationship derived from the analytical solutions to Fick's equations with the appropriate boundary conditions:

$$D_{eff} = \frac{e^2}{Mt} \quad \text{(II.7)}$$

where e is the membrane thickness, t the characteristic time and M a factor depending on the model applied to calculate the characteristic time. The latter is defined as the required time to reach a given percentage of the steady-state flux. There are different characteristic times depending on the selected diffusion theory **[Legrand 2013a]**. The most often used in determining hydrogen diffusion coefficients are the so called "time lag" and "breakthrough time" methods **[Daynes 1920, Chanfreau 1992]**. In the "time lag" method, the characteristic time, refers as t_{lag}, is defined as the required time to reach 63% of the steady-state flux, whereas, in the breakthrough time method, it corresponds to the time at which the flux is 10% of the steady-state flux. In accordance with previous studies, the *breakthrough time* t_b is used in this study, with a corresponding constant M=15.3 **[Brass 1996, Frappart 2010, Oudriss 2012b]**.

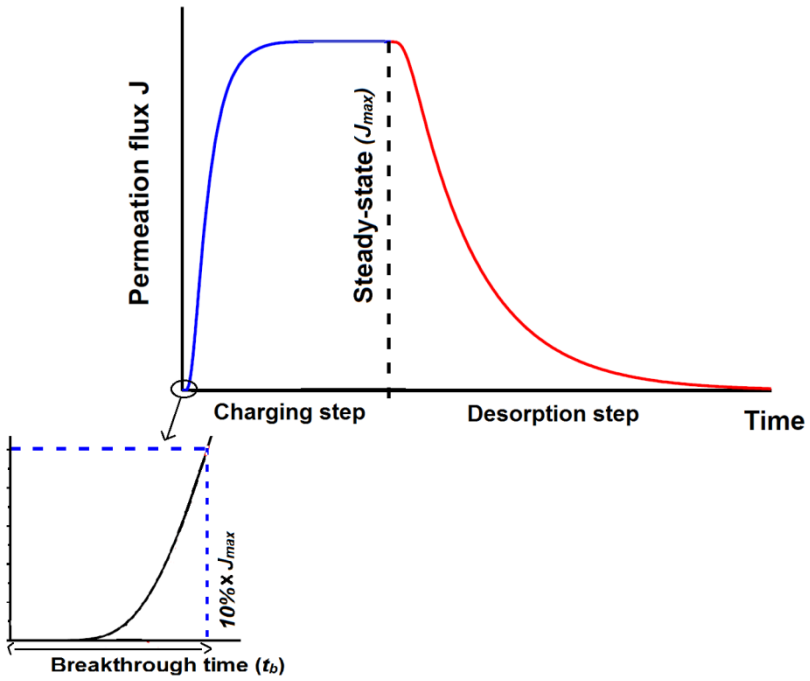

Fig. 5 - A graphical illustration of the typical flux curve and the breakthrough time.

The effective diffusion coefficient D_{eff} can also be calculated from the hydrogen desorption step, by measuring the desorbed hydrogen quantity **[Crank 1975]**. The deduced diffusion coefficient is also affected by the trapping phenomenon. Moreover, analysis of the desorption curve allows determining the concentrations of the interstitial hydrogen C_L and reversibly trapped hydrogen C_{Tr} **[Zakroczymski 2006, Frappart 2010]**. The sum of C_L and C_{Tr} is called the diffusible concentration

C_D. As an example, an experimental desorption curve and the associated theoretical curve (without trapping) are presented in Fig. 6. The desorption theoretical curve is obtained using a model based on the resolution of Fick's laws **[Frappart 2011a]**. The area under the experimental desorption curve represents the diffusible hydrogen concentration C_D, whereas the theoretical one gives access to the lattice hydrogen C_L. Thus, the reversibly trapped hydrogen concentration can be deduced, using the following relation (II.8):

$$C_{Tr} = C_D - C_L \tag{II.8}$$

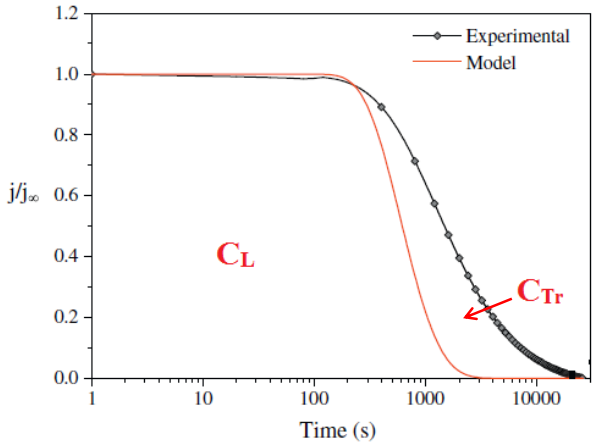

Fig. 6 - An experimental desorption curve and the associated theoretical curve (without trapping) **[Oudriss 2012b]**.

Gaseous permeation

Gaseous permeation has been applied also in several studies to investigate hydrogen diffusion in materials **[Yamanishi 1983, Tanabe 1992, Brass 2006, Horinouchi 2013]**. Hydrogen is introduced into the samples by gaseous charging at high temperature and high hydrogen pressure **[Brass 2006]**. Despite the similarity of two charging processes, the mechanisms of hydrogen penetration are quite different. The Fig. 7 illustrates a simplified diagram of gaseous permeation process. On the charging side, gaseous hydrogen is maintained at a predetermined pressure higher than that at the output side. Then the hydrogen atoms diffuse through the specimen and are detected on the exit surface to determine the permeation rate.

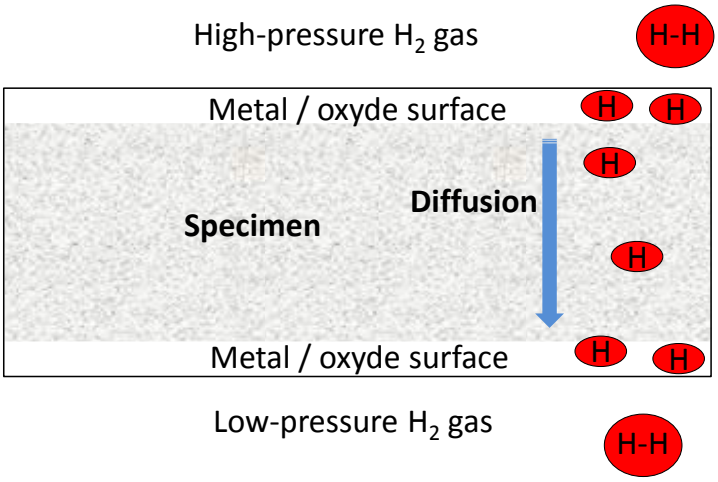

Fig. 7 - Gaseous permeation mechanisms **[Feng 2007]**.

Unlike the EP, the adsorption phase occurs directly on the metal surface, in three steps: physisorption of dihydrogen molecules at the surface, dissociation of these molecules and chemisorption of the hydrogen atoms. In sum, the adsorption can be described by equation (9):

$$H_2 + 2M \rightarrow 2MH_{ads} \tag{II.9}$$

The amount of hydrogen that diffuses through the metal can be detected by using thermal desorption spectroscopy **[Frappart 2011b]**. The permeation flux is proportional to the practical pressure of the permeating gas and the effective diffusion can be deduced using the "time-lag" method.

Permeation technics are efficient to evaluate the hydrogen effective diffusivity. However, these technics do not allow the localization of hydrogen at the microstructure scale, which is an important factor affecting HE. Alternative technics consist in charging metals with hydrogen or deuterium and analyzing their distribution at the surface using Secondary Ion Mass Spectroscopy (SIMS).

2.1.2. SIMS analysis for hydrogen diffusion measurements

Several studies have used the SIMS technic in order to characterize hydrogen transport and segregation at the microstructure scale **[Ladna 1987a, Ladna 1987b, Brass 2006, Kawamoto 2007, Saintier 2011]**. Briefly, this technic consists in sputtering the specimen surface with a focused primary ion beam and detecting the secondary ions subsequently ejected. The primary ion is generally Cs^+, which can achieve high sensitivity to hydrogen and deuterium **[Takai 2002]**. SIMS enables direct visualization of the hydrogen distribution in deep regions from the surface and the comparison of the hydrogen concentration among different microstructure components. This technic has been used to investigate the effect of the grain boundary structure on the H distribution in Ni bicrystals **[Ladna**

1987a]. Park **[Park 2010]** has also applied the SIMS technic to evaluate segregation of deuterium in grain boundaries.

2.1.3. Factors impacting experimental data

The experimental data extracted from EP can be affected by many factors. In addition to the electrochemical processing parameters, such as cathodic current density, charging solution or temperature, hydrogen permeation can also be affected by materials factors. These factors can be dimensional characteristics of the metallic membrane **[Frappart 2011a]**, but also microstructural parameters such grain size, grain boundaries volume fraction or dislocations. In order to decouple the effects of these different parameters on the EP results, Legrand *et al*. conducted analysis on the trapping effects and the presence of a thin layer at the surface (oxide, coating,…), by using FEM modeling **[Bouhattate 2011, Legrand 2012]**. In these studies, the authors proposed analytical equations to adjust the values of experimental data, such as effective diffusivity or the subsurface concentration, depending on the characteristics of the material and its environment. In an another study from the same authors, it has been shown the existence of a critical membrane thickness, below which the scale effects can alter the calculated diffusion coefficient **[Legrand 2013b]**. In this study, grain boundaries were modeled by a homogeneous phase and considered as fast diffusion paths. However, grain boundaries can also trap hydrogen, as the majority of metal defects. The trapping phenomenon, as a result of defect-metal interactions, is the main cause of the discrepancy of "apparent" diffusivities experimentally measured at low temperatures (20°C < T < 150°C) **[Coudreuse 2000]**.

2.2. Hydrogen diffusion and trapping effects

2.2.1. Lattice diffusion

Hydrogen diffuses by moving along interstitial sites (octaedric and tetraedric), due to its small size. The principle of the lattice diffusion consists in series of jumps from one site to another interstitial site. This jump requires sufficient activation energy E_a to overcome the energetic barrier, as illustrated in Fig. 8.

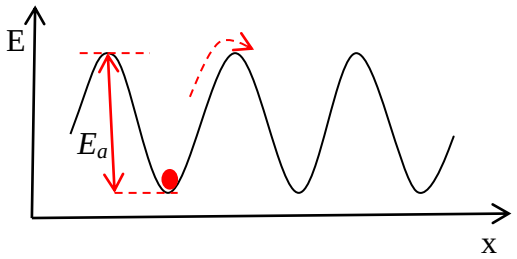

Fig. 8 - Schematic representation of the lattice diffusion mechanism.

However, the hydrogen diffusion in metals is affected by the trapping phenomenon and others models of diffusion were developed in the past to approximate the experimental data.

2.2.2. Models with trapping

a) Definition of hydrogen trapping

The mechanism of trapping was first suggested by Darken and Smith in 1949 **[Darken 1949]** in order to understand the decrease of the hydrogen diffusivity in steels. From a thermodynamic point of view, a trapping site is a site where the hydrogen chemical potential is lower than that in an interstitial site. The different microstructural defects (vacancies, dislocations, etc.) act as hydrogen traps **[Ly 2009]** and the required activation energy to pass the energetic barrier increases. To illustrate this, the energy differences between lattice sites and trap sites are schematically presented in Fig. 9. Consequently, the hydrogen diffusion in the material is delayed, and conventional analytical methods to determine the diffusion coefficient, lead to an effective or "apparent" diffusion coefficient D_{eff} **[Brass 2000]**.

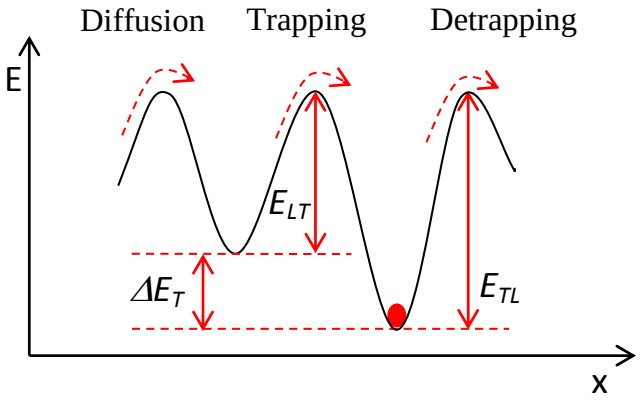

Fig. 9 - Illustration of the diffusion mechanism with the presence of trap sites. E_{LT} is the actvation energy of lattice diffusion, referring to Fig. 8 $E_{LT} = E_a$. E_{TL} is the activation energy for moving from a trap site to a lattice site and ΔE_T is the trap binding energy, defined by $\Delta E_T = E_{TL} - E_{LT}$ **[Krom 2000]**.

b) Hydrogen trapping models

Most of the theoretical models describing the hydrogen diffusion and trapping phenomena are based on the model of McNabb and Foster **[McNabb 1963]**. Oriani **[Oriani 1970]** then Krom **[Krom 2000]** reformulated this model. We present here the formulations of Oriani and Krom.

In this model, a modified Fick's law is proposed, by distinguishing the hydrogen concentrations in lattice sites and trapping sites, respectively noted C_L and C_T:

$$\frac{\partial C_L}{\partial t} + \frac{\partial C_T}{\partial t} - D_L \nabla^2 C_L = 0 \tag{II.10}$$

where D_L is the usual bulk diffusivity in a perfect lattice. By assuming that the hydrogen concentration in trap sites C_T depends only on the hydrogen concentration in lattice sites, the equation can be reformulated as:

$$\frac{\partial C_L}{\partial t} - D_{eff} \nabla^2 C_L = 0 \qquad \text{with} \qquad D_{eff} = \frac{D_L}{1 + \frac{\partial C_T}{\partial C_L}} \tag{II.11}$$

We consider here saturable traps. Saturable traps can retain a finite number of atoms. A dislocation is a saturable trap while a void and crack are insaturable. In this case, the following trapping reaction can be considered:

$$[H]_L \rightleftarrows [H]_T \tag{II.12}$$

Where $[H]_L$ is the hydrogen atom in a lattice site and $[H]_T$ is the hydrogen atom in a trap site. Since the solubility of hydrogen is very low and by assuming a very low trap density N_T compared to lattice sites density N_L ($N_T \ll N_L$), the derivative of the trapped hydrogen concentration C_T is given by:

$$\frac{\partial C_T}{\partial t} = \kappa \theta_L N_T (1 - \theta_T) - \lambda C_T \tag{II.13}$$

where θ_L is the occupancy of lattice sites: $\theta_L = C_L / N_L$; θ_T is the occupancy of trap sites: $\theta_T = C_T / N_T$; κ is the frequency of hydrogen atoms jumping from lattice sites to a trap site and λ is the frequency for the reverse case.

Oriani **[Oriani 1970]** assumed that there is a chemical equilibrium between lattice hydrogen and trapped hydrogen, *i.e.*, the same chemical potentials for the two types of atoms: $\mu_L = \mu_T$. The chemical potentials of the lattice hydrogen and trapped hydrogen are given by equations (II.14) and (II.15), respectively.

$$\mu_L = \mu_L^0 + RT \ln \frac{\theta_L}{(1-\theta_L)} \approx \mu_L^0 + RT \ln \theta_L \quad \text{(II.14)}$$

$$\mu_T = \mu_T^0 + RT \ln \frac{\theta_T}{(1-\theta_T)} \quad \text{(II.15)}$$

μ_L^0 and μ_T^0 are the chemical potentials of the lattice hydrogen and trapped hydrogen, respectively, in a reference state.

Hence by equalizing, equation (II.14) and (II.15), one can deduce easily an expression of the trap equilibrium constant K_T :

$$\frac{\theta_T}{\theta_L(1-\theta_T)} = \frac{\kappa}{\lambda} = e^{-\Delta E_T/RT} = K_T \quad \text{(II.16)}$$

where $\Delta E_T = \mu_T^0 - \mu_L^0$ is the trap binding energy. From this equation, by substitution of θ_T and θ_L by C_T /N_T and C_L /N_L, respectively, we obtain:

$$C_T = \frac{N_T}{\left(1 + \frac{N_L}{K_T C_L}\right)} \quad \text{(II.17)}$$

If the trap density and temperature remain constant and with the assumption of very low occupancy ($\theta_T << 1$), the effective diffusivity in equation (II.11) becomes:

$$D_{eff} = \frac{D_L}{1 + K_T \frac{N_T}{N_L}} \quad \text{(II.18)}$$

This trap model is based on many assumptions. It is assumed that traps are isolated and that transport between traps occurs by lattice diffusion **[Krom 2000]**. Another limitation of this model is that only reversible traps sites are considered. Indeed, trap sites are generally classified into **[Pressouyre 1979]**:

- *Irreversible trapping sites*, characterized by high binding energy (above 0.5 to 0.6 eV). In this case, the probability that hydrogen get out of the trap site is almost null.
- *Reversible trapping sites*, characterized by low binding energy (between 0.2 and 0.45 eV). In this case, there is a local equilibrium between concentration of lattice hydrogen and the concentration of trapped hydrogens.

This classification, based on the trap binding energy, is convenient but stays subjective because of its dependence on different parameters such as temperature **[Jérôme 2003]**. Others theoretical models,

that consider irreversible traps or a combination of both categories have been developed **[Leblond 1983a, Leblond 1983b]**. However, there is not a unique approach because of the variety of defects (dislocations, vacancies…) which are potential source of trapping.

2.2.3. Defects in metal: trap sites for hydrogen

As said above, the hydrogen transport is affected by the microstructural defects which are energetically favorable for hydrogen trapping. Fig. 10 shows possible defects acting as trap sites for hydrogen.

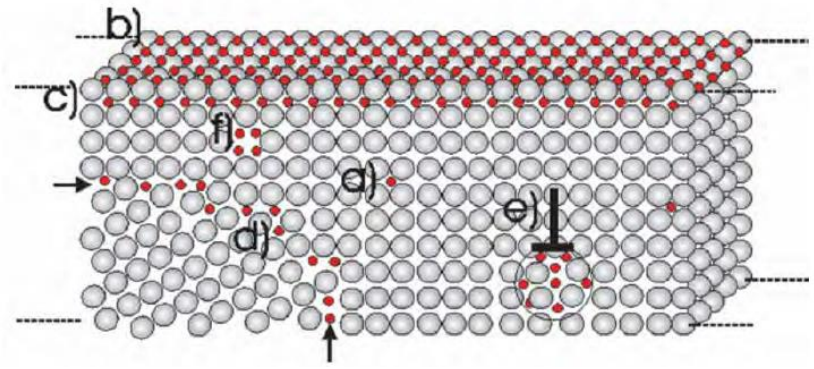

Fig. 10 - Schematic representation of defects in metal. Trap sites for hydrogen can be localized in: surface (b), subsurface (c), grain boundaries (d), dislocations (e) or vacancies (f). (a) Corresponds to a lattice site. **[Pundt 2006]**.

Vacancies

Known as the simplest type of point defects, vacancies interact strongly with interstitial hydrogen in most of metals. The Hydrogen trapping at vacancies has been highlighted in a number of studies, using both experimental and theoretical methods **[Besenbacher 1990, Birnbaum 1997, Liu 2009]**. The entrance of hydrogen in this type of defect is promoted by the attractive character of the interaction between interstitial hydrogen and the vacancy. The binding energy for a single H atom to be trapped in Ni by a single vacancy is estimated between 0.4 and 0.8 eV **[Oudriss 2012a]**.

From experiments on hydrogen-metal system, it was pointed out that hydrogen can induce superabundant vacancy formation **[Fukai 2001, Carr 2004, Carr 2006]**, indicating that hydrogen promotes and stabilizes vacancies. As a result, it was reported that several (three to six) H atoms can be trapped by a single vacancy **[Lu 2005]**. These findings are supported by ab-initio calculations results **[Sugimoto 2014, Zhang 2014]**. According to simulations works, the hydrogen trapping at vacancies may decrease H diffusion coefficients by several orders of magnitude **[Hickel 2014]**. However, this effect mainly depends on the vacancy concentration which is relatively low at room temperature **[Oudriss 2012a]**.

Dislocation trapping

Dislocations are linear defects produced in metals by plastic deformation and grain growth processes. Treated within the framework of continuum mechanics, except in the regions of the dislocation core, these defects cause distortions of the crystal lattice. As a result, hydrostatic stresses are developed in proximity to the dislocation core **[Hirth 1978]**, implying a range of binding energy **[Barnoush 2011]**.

Described by trapping models, dislocations generate a number of trap sites, with different trapping energies. According to different works **[Choo 1982, Thomas 2002, Frappart 2010, Oudriss 2012c]**, the binding energy around edge dislocation is estimated around 0.3 to 0.4 eV, corresponding to a reversible trapping. While in the dislocation core, it is estimated around 0.6 to 0.7 corresponding to high and irreversible trapping **[Taketomi 2008]**. As a result of the attractive interaction of dislocations, the mobility of dissolved hydrogen is substantially reduced, leading to segregation of hydrogen in the core and in the dislocations.

Grain boundary traps

It is largely acknowledged that interactions of hydrogen with grain boundaries play a predominant role in the HE mechanisms **[McMahon Jr 2001]**. But the understanding of these interactions is limited, due mainly to the structural complexity of these entities. Morever, some grain boundaries, depending on their misorientations, may contain intrinsic defects such as geometrical necessary dislocations or vacancies **[Priester 2006]** and as a result provide trap sites to hydrogen. Trapping of hydrogen in grain boundaries is supported by experimental and numerical works **[Aucouturier 1982, Yao 1991, Pedersen 2009, Oudriss 2012b]**. Yao **[Yao 1991]** suggested that grain boundaries would have a retardation effect on the hydrogen transport, because of their trapping capacity. More recently, Oudriss *et al*. **[Oudriss 2012b]** have shown that the decrease in grain size induced a slowdown of the hydrogen diffusion and an increase in the concentrations of irreversibly and reversibly trapped hydrogen. They concluded that this slowdown of hydrogen diffusivity was associated to an increase of trapping sites density, provided by a category of grain boundaries with low misorientations. In this study, trap binding energies associated mainly to geometrically necessary dislocations stored in the GBs were estimated between 0.3 and 0.63 eV.

On the other hand, grain boundaries are believed to provide high diffusion paths for hydrogen, more particularly those with high misorientations. A number of experimental works have pointed out the acceleration of diffusion in grain boundaries **[Harris 1991, Arantes 1993, Doyle 1995, Brass 1996, Oudriss 2012b]**. This dual effect of grain boundaries may explain controversial interpretations and conclusions found in the literature about the grain boundary influence on hydrogen diffusion.

In summary, hydrogen diffusion is strongly influenced by hydrogen-defects interactions which may explain inconsistencies in experimentally measured data. Among all the defects, grain boundaries

have a crucial impact on macroscopic diffusivities, particularly because of their structure complexity and their preponderant volume fraction for nanocrystalline materials **[Palumbo 1990b, Marte 1997]**. In the next section, we present an introduction to fundamentals on grain boundaries and to grain boundary diffusion.

II. Fundamentals on grain boundaries and intergranular diffusion

In a polycrystalline material, the interfaces between two grains with the same structure and composition, but with different crystallographic orientation, are called grain boundaries. It is largely agreed that these entities impact material's properties. Studies on grain boundaries are difficult due to the large variability in their structure but also of their very fine scale which hamper the direct observation of their properties. However, the dependence of grain boundary properties on their structure has been highlighted in several works, in the past. This motivated the development of different theory and classifications of grain boundaries.

1. Grain boundary structure

Grain boundary geometry is defined at least by five macroscopic independent parameters (degrees of freedom, DOFs) **[Lange 1967, Wolf 1989, Sutton 1995, Priester 2006]**. Three parameters are needed to specify the orientation of one grain with respect to the other and two others to specify the boundary plane. Considering the configuration presented in the Fig. 11, the five degrees of freedom can be detailed as:

- the rotation angle θ between the two grains **A** and **B** (1 DOF)
- the rotation axis *o* between the two lattices (2 DOFs)
- the normal ***n*** to the grain boundary plane (2 DOFs)

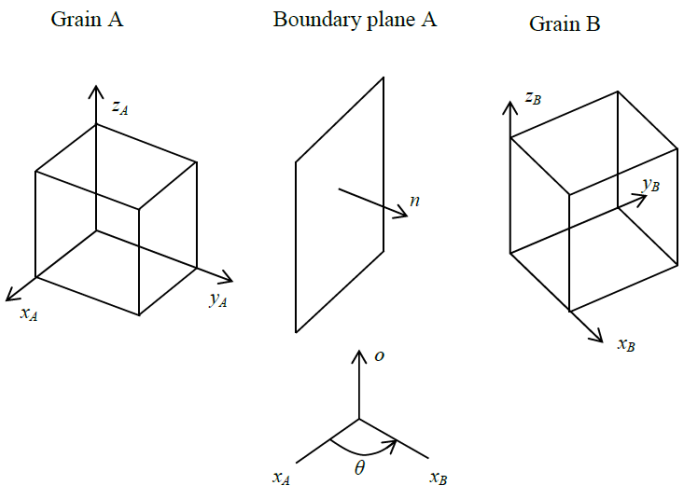

Fig. 11 - Geometric variables that define a grain-boundary

It is difficult to take into account all the five parameters when modeling material properties as a function of grain boundary character. Therefore, grain boundaries are classified in different categories. The most generally used is based on the relationship between the rotation axis o, and the grain boundary normal n. A grain boundary is denoted ***twist*** boundary if the rotation axis *o* is perpendicular to the boundary plane (Fig. 12a) or ***tilt*** boundary if the rotation axis o lies in the boundary plane (Fig. 12b). In the latter case, if the boundary plane represents the plane of the mirror symmetry of the crystal lattices of two grains, it is called symmetrical; otherwise it is asymmetrical.

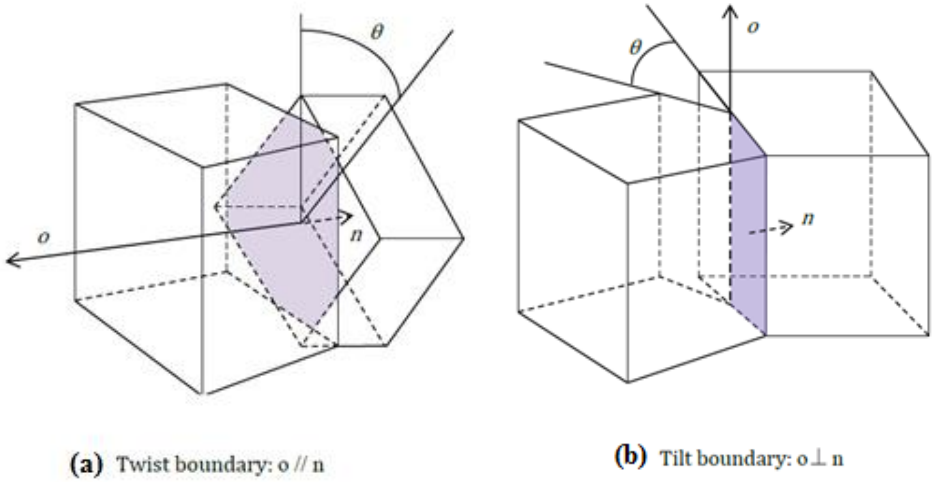

Fig. 12 - Representation of twist (a) and tilt (b) grain boundaries

However, most of the boundaries are a mixed of the two types. In that case, it is suitable to decompose the rotation into two successive rotations in order to find the tilt and twist components of the mixed relationship **[Sutton 1995]**. In addition to the classification described above, grain boundaries can be grouped into two categories depending on the misorientation angle between the adjoining grains:

- Low-angle boundaries (LAGBs) with misorientations smaller than about 15 degrees.
- High-angle boundaries (HAGBs) with misorientations larger than 15 degrees.

1.1. Low-angle boundaries

In the case of Low-angle boundaries, the misorientation is generally accommodated by an array of dislocations **[Sutton 1995, Priester 2006]**. Tilt boundaries consist of edge dislocations and the simplest case is a low-angle symmetric tilt grain boundary, illustrated in Fig. 13a. An example of LAGB where one can see a set of edge dislocations is as well presented in Fig. 13b. The spacing *d* of the dislocations is related to the angle θ and the size of the Burgers vector b, by the expression **[Read 1950]**:

$$d = \frac{b}{2\sin(\frac{\theta}{2})} \approx \frac{b}{\theta} \qquad \text{(II.19)}$$

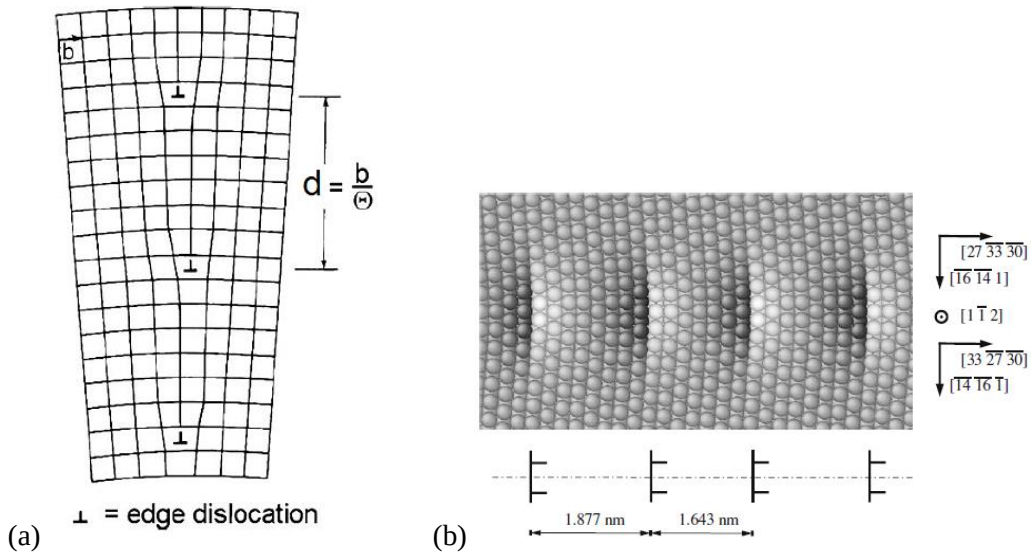

Fig. 13 - (a) Structure of a low-angle boundary after Burgers **[Burgers 1940]**. (b) Example of LAGB produced by atomistic simulations: a symmetrical [**1 1̄ 2**] tilt GB in Al with a tilt angle of 9.34°**[Cheng 2009]**.

Generally, there is a limit beyond which the grain boundary structure cannot be described by the dislocation model. This limit is conventionally assumed to be between 13° and 15° **[Brandon 1966]**. However, this transitional angle is not clearly defined and recent studies on aluminum **[Winning 2005]**, based on the mobility energy differences of LAGB and HAGB, reported a range between 8.6° and 14.4° (Fig. 14). The authors observed particularly that the transition depends on the rotation axis of the grain boundary and on the grain boundary plane.

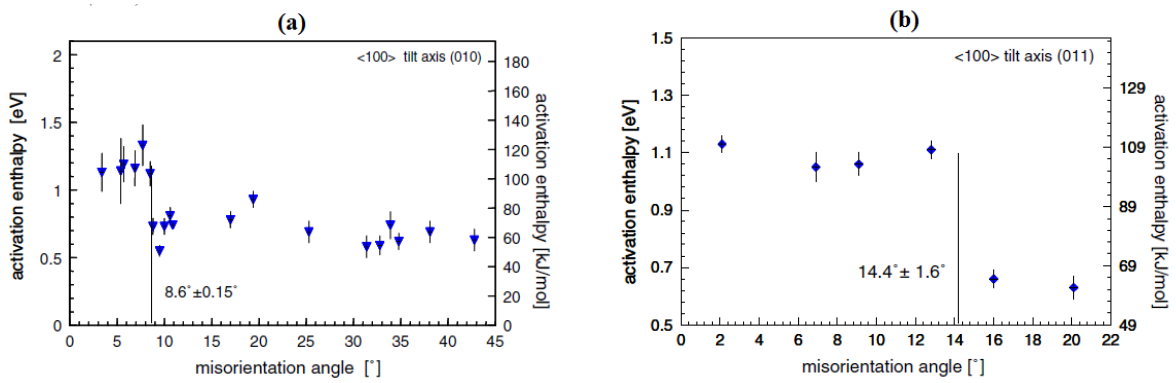

Fig. 14 - Activation enthalpy vs. misorientation angle for the motion of all investigated planar, symmetric (a) <1 0 0> (0 1 0)-tilt grain boundaries and (b) <1 0 0> (0 1 1)-tilt grain boundaries **[Winning 2005]**.

For misorientations above this limit, the dislocation spacing is so small that the dislocation cores overlap. It should be noted that LAGBs are characterized by a good fit of atoms in both lattices, except for dislocations cores, and by consequence, a little free volume.

1.2. High-angle boundaries

In contrast to the LAGBs, there is a large variety of boundaries in HAGBs. Thus, different classifications inside this group have been proposed. The most commonly used method is based on the theory of coincidence site lattice (CSL).

- *Coincidence-Site Lattice Model*

The coincidence-site lattice model was first proposed by Kronberg and Wilson in 1949 **[Kronberg 1949]**. In this model, the grain boundaries are classified in function of their Σ value. This parameter Σ is defined as the inversed density of coincident sites of the two grains. In other words, considering an elementary cell, the value of Σ can be expressed as:

$$\Sigma = \frac{\text{Number of coincidence site in an elementary cell}}{\text{Total number of all lattice site in an elementary cell}}$$

Two examples of CSL relationship are illustrated in Fig. 15. One can observe a site out of three is common between the two lattices for the Σ3 (Fig. 15a), while it is a site out of five for the Σ5 (Fig. 15b).

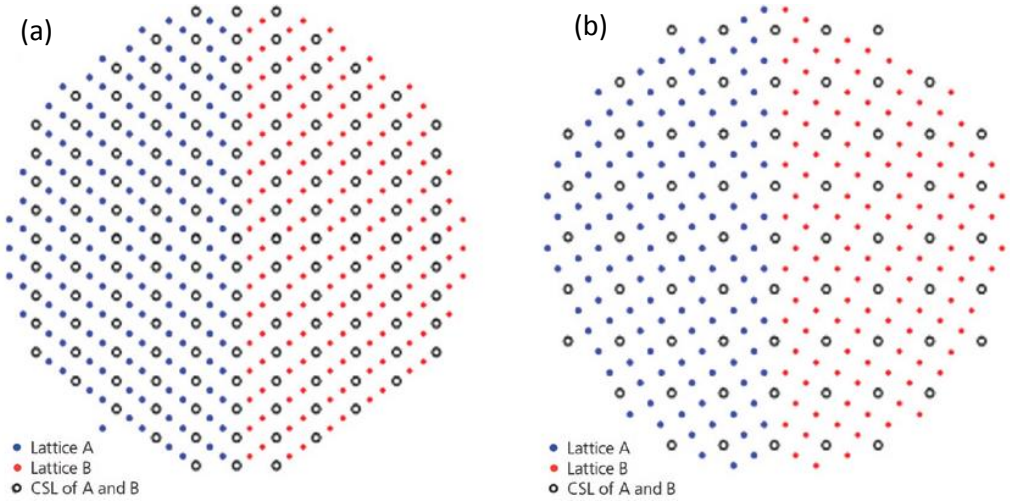

Fig. 15 - (a) The Σ3 boundary (twin boundary) is a 60° rotation about the [111] direction. (b) The Σ5 boundary is a 36.9° rotation about the [100] direction **[Instruments]**.

In reality, it is rare to find boundary with exact CSL relationship. Therefore, there is a maximum deviation to accept the boundary as belonging to the CSL of type Σ **[Grimmer 1974]**. This maximum deviation θ_x is given by:

$$\theta_x = \theta_t \Sigma^w \tag{II.20}$$

where $\theta_t \approx 15°$ corresponds to the limit of low angle grain boundaries (for Σ=1) and the exponent *w* varies from 0.5 to 1**[Brandon 1966, Déchamps 1987, Palumbo 1990a]**.

The boundaries with a low value of Σ (Σ<29) are called CSL or special boundaries. In fact, those boundaries, which present a high density of coincident sites lattice, exhibit improved properties. Boundaries with a high value of Σ (Σ>29) are named general (or random) boundaries. This classification is generally used in the field of engineering grain boundary (GBE). But the relationship between the crystallographic characteristics and the boundary properties is not still well established **[Priester 2006]**. The different classifications are summarized in Fig. 16.

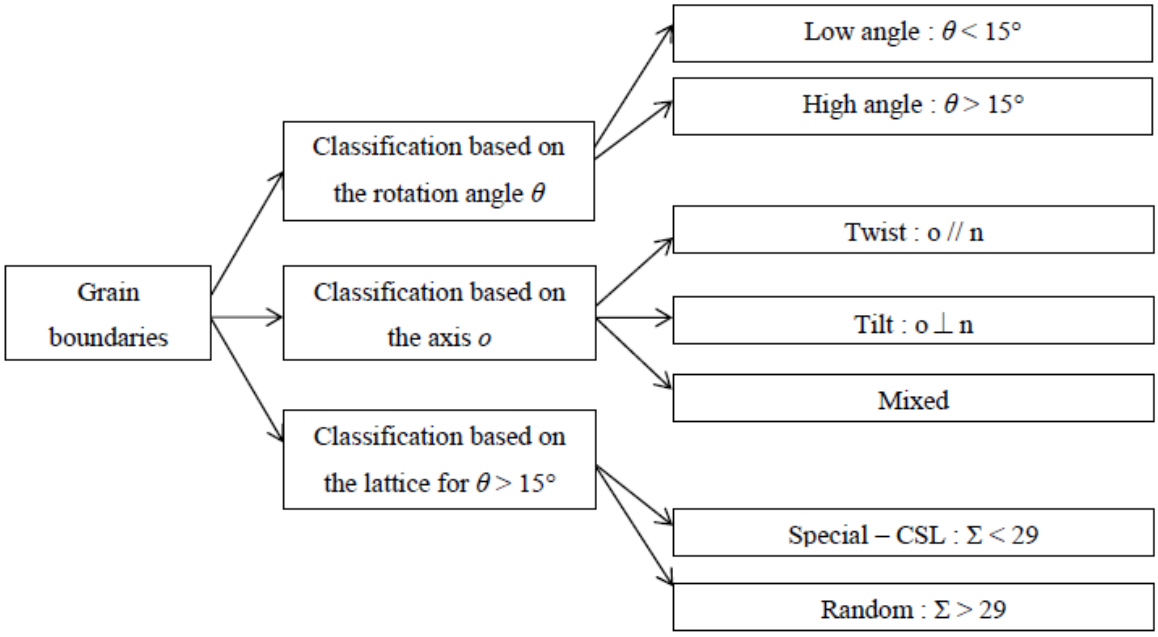

Fig. 16 - Classification of grain boundaries.

1.3. Intersections of grain boundaries: Triple junctions

In a polycrystal, three grains can meet at a line, called triple junction or triple line. This one-dimensional defect is poorly studied despite its importance in many material properties **[Priester 2006]**.

The geometrical description of triple junctions is much complex than that of grain boundary. In general, it requires eleven independent macroscopic parameters **[Priester 2006]**. However, due to geometrical and energetical considerations, the product of the three grain boundary misorientations matrices is equal to identity matrix, when expressed in the same reference **[Priester 2006]**. This results in a combination rule which applies at the triple junction between the three CSL- boundaries **[Miyazawa 1996]**:

$$\Sigma_1\Sigma_2 = d^2\Sigma_3 \tag{II.21}$$

where Σ_1, Σ_2 and Σ_3 are the CSL-types of boundaries 1, 2 and 3, respectively. d is a common divisor of Σ_1 and Σ_2.

Triple junctions are often classified into “random” or special depending on the type boundaries that form it **[Schuh 2003b]**.

2. Grain boundary diffusion

2.1. Analytical models of grain boundary diffusion

Most of theoretical models describing grain boundary contribution to diffusion are derived from the Fisher model **[Fisher 1951]**. In this model, the grain boundary is considered as a semi-infinite isotropic slab of high diffusivity.

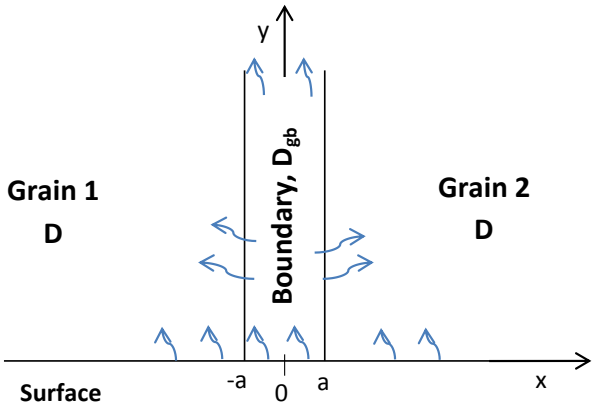

Fig. 17 - Fisher's model of an isolated grain boundary.

As illustrated in Fig. 17, the grain boundary is perpendicular to a reference surface and is embedded in a low-diffusivity isotropic crystal. The grain boundary is described by two parameters: its thickness *2a* and diffusivity D_{gb}. The latter is generally much larger than the lattice diffusion D ($D \ll D_{gb}$). Atoms can diffuses along the GB but can also leave it and continue their diffusion in the grains. To describe mathematically the diffusion, the Fick's second law is applied to diffusion inside the grains (Eq. 22) and inside the grain boundary slab (Eq. 23):

$$\frac{\partial C}{\partial t} = D\nabla^2 C \tag{II.22}$$

$$\frac{\partial C_{gb}}{\partial t} = D_{gb}\frac{\partial^2 C_{gb}}{\partial y^2} + \frac{D}{a}\frac{\partial C}{\partial x}\bigg|_a \tag{II.23}$$

C and C_{gb} are the concentrations in the grains and the grain-boundary, respectively. For the Eq. 23, the term in the right side comprises two causes of variation in the concentration of the diffusing element: the first part represents the flux divergence in the direction of the boundary and the second describes the interaction between the boundary and the grains. In this model, a uniform concentration in the normal direction to the boundary is assumed. Eq. 23 is valid only if the thickness of the boundary is very small (2a ~ 0.5 nm) and the frequency of jumps of atoms in the x direction is high **[Martin**

1975]. It also assumed the continuity of the concentrations and the diffusion fluxes across the interfaces between grain-boundaries and grains. With these assumptions, Fisher has calculated an approximate analytical expression of the concentration C:

$$C(\xi,\eta,\beta) = C_0 \exp(-\frac{1}{\pi^{1/4}}\frac{\eta}{\beta^{1/2}})erfc(\frac{\xi}{2}) \qquad \text{(II.24)}$$

where C_0 is the initial concentration on the free surface (y=0), which is assumed constant, and ξ, β and η are respectively defined by :

$$\xi = \frac{x-a}{\sqrt{Dt}} \qquad \beta = \frac{D_{gb}a}{2D\sqrt{Dt}} \qquad \eta = \frac{y}{\sqrt{Dt}}$$

This solution only works for sufficiently large values of β (β>10^2). Thus, a sufficiently low temperature is assumed ($D \ll D_{gb}$).

A more accurate solution of the Fisher model has been formulated by Whipple, keeping the same assumptions **[Whipple 1954]**. This allows wider possibilities in the range of the considered temperatures. The exact analytical solution of the concentration, proposed by Whipple is in the form of an integral and it is not practical to determine the data on the grain boundary diffusion. Some simplifications of the exact solutions are possible for a more convenient expression for experimental measurements **[Levine 1960, Le Claire 1963, Kaur 1995]**. The exact solution of Suzuoka **[Suzuoka 1961]** is quite close to that of Whipple. The only difference is the grain boundary behavior at the initial time (t=0). It is assumed that a finite amount of diffusing element is deposited on the surface at y = 0, so that the initial concentration C_0 does not remain constant over the time.

The applicability of these various analytical solutions to describe experiments depends mainly on the experimental conditions, such as the temperature and the initial conditions. One should refer to **[Martin 1975, Kaur 1995]** for a detailed critical review on their applicability and limitations. It is particularly useful to know the kinetic regime of the studied problem to choose the correct analytical model. Harrison **[Harrison 1961]** was the first to classify the different types of diffusion behavior along grain boundaries.

2.2. Harrison kinetics

In a polycristal, the grain boundary diffusion and the lattice diffusion can rarely be dissociated. The leakage of diffusant elements through the interfaces grains/grain boundaries depends mainly on the relative magnitudes of the lattice diffusion coefficient D and the grain boundary diffusion coefficient D_{gb} and thus on the experimental conditions such as the annealing temperature and the annealing time **[Kaur 1995, Mehrer 2007]**. Therefore, different kinetics of diffusion can be observed depending on the experimental conditions, which will determine the shape of the diffusion profile.

Harrison **[Harrison 1961]** classified the various possible types of diffusion behavior for polycrystals. He defined three diffusion regimes referred to as types A, B and C (Fig. 18).

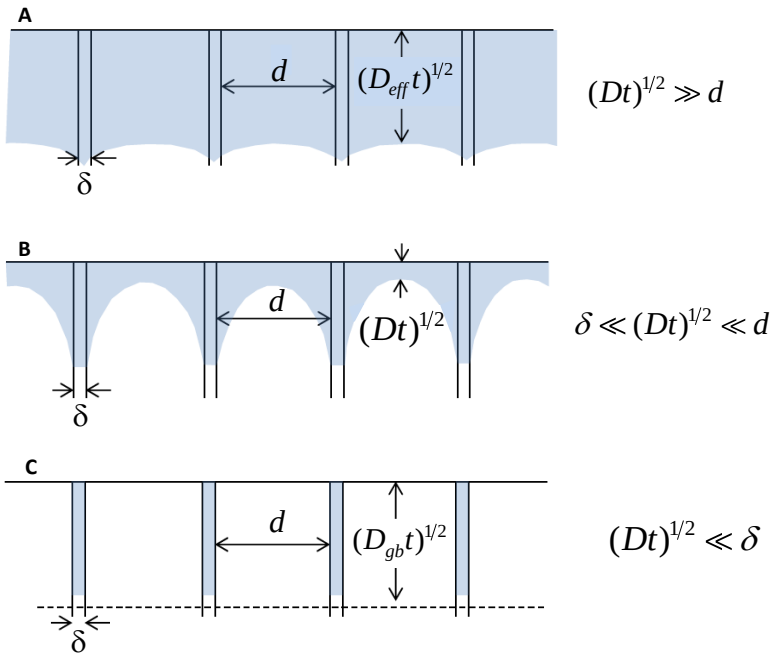

Fig. 18 - Schematic illustration of the types A, B, and C diffusion regimes in a polycrystal after Harrison **[Harrison 1961]**, d is the spacing between GBs, δ is the grain boundary width, and t is the diffusion time.

- Type A

In the A regime, the diffusion occurs in the grains and along grain boundaries at the same time. This regime is characterized by a lattice diffusion length $(Dt)^{1/2}$ larger than the spacing d between the GBs so that the diffusion from adjacent GBs into crystal overlaps. This is the case for nanocrystalline materials, high temperatures, or/and very long diffusion anneals. On the macroscopic scale, the system can be approximated by a homogenized equivalent system with an effective diffusion coefficient D_{eff}. The latter can be determined by the Hart's formula:

$$D_{eff} = f_{gb}D_{gb} + (1 - f_{gb})D \qquad \text{with} \quad f_{gb} = q\delta/d \tag{II.25}$$

With f_{gb} the volume fraction of GBs in the polycrystal and q a numerical factor depending on the grain shape (q=1 for parallel GBs).

- Type B

In the kinetic regime B, the GB diffusion is accompanied also by the lattice diffusion. But, in contrast to the regime A, atoms diffuses faster along the GBs than inside the grains and the diffusion from adjacent GBs into the crystal do not overlap. The regime B is the most appropriate to the experimental

diffusion measurements because it happens for a wide range of annealing temperatures, in comparison to the A and C regimes.

- Type C

In the C kinetic regime, the diffusion takes place only along GBs and the lattice diffusion is assumed to be insignificant. This corresponds to a situation where the lattice diffusion length is much smaller than the GB thickness (δ). This is the case for extreme conditions such as low annealing temperatures or/ and very short anneal times.

Even though others classifications were proposed in the following years, Harrison's classification of diffusion kinetics is still widely used for polycrystalline materials **[Kaur 1995]**.

In the mathematical models of diffusion, described above, the diffusant concentration is assumed continuous at the interfaces between GB and the grains. In other words, it is stated that at the interface:

$$c_b = c_g \tag{II.26}$$

where c_b is the concentration in the boundary and c_g the concentration in the grain adjacent to the boundary. However, this condition is not valid in the case of heterodiffusion **[Kaur 1995]**, because of the intergranular segregation.

2.3. Effects of GB segregation on GB diffusivity

Grain-boundary segregation can be defined as the local solute enrichment in the GB following a redistribution of this solute between bulk and GB **[Priester 2006]**. In general, the segregation phenomenon can be explained by the presence of attractive sites for the atoms within the GBs, due to their environment that differs from the lattice. Grain-boundary segregation is known to affect grain-boundary properties and can contribute to the hydrogen embrittlement.

The importance of considering the effects of GB segregation in mathematical diffusion models was first highlighted by Bokshtein **[Bokshtein 1958]** and then confirmed by Gibbs **[Gibbs 1966]**. According to Gibbs, the presence of equilibrium solute segregation was taken into account by replacing the GB width δ by $s\delta$ with s the segregation factor defined by:

$$s = c_b / c_g \tag{II.27}$$

where c_b is the concentration in the boundary and c_g the concentration in the grain adjacent to the boundary. This equation is based on two main assumptions **[Mishin 1999]**:

- A local thermodynamic equilibrium is assumed between the solute atoms in the GB and the atoms in lattice adjacent to the boundary.

- The GB segregation follows a Henry-type isotherm. That means $c_b = s \times c_g$, s being a function of the temperature only.

This factor *s* is generally determined from the values of the product $s\delta D$ measured from sectioning experiments in B-regime and C-regime. As the GB diffusion, the solute segregation follows an Arrhenius relation, increasing when the temperature decreases **[Mehrer 2007]**:

$$s = s_0 \exp(\Delta H_{seg} / k_B T) \quad \text{(II.28)}$$

where ΔH_{seg} is the segregation enthalpy. s_0 is a pre-exponential factor related to segregation entropy.

If it is widely accepted that the solute segregation affects the GB diffusion rate, the correlations between the kinetics of segregation and the effective diffusivity are not still well understood. According to Sutton and Balluffi **[Sutton 1995]**, the effects of GB segregation on diffusivity depends on the GB atomic sites that are altered by the segregation phenomenon. If a strong segregation occurs on the boundary sites that are responsible for fast diffusion, this can lead to a "blockage" of the GB diffusion. As a result, the GB diffusion can slow down. However, this retarding effect of GB segregation depends on the solute concentrations, as pointed out By Mütschele and Kirchheim **[Mütschele 1987]**. According to their study, a retarding effect of GB segregation on GB diffusivity was observed at low concentrations of H while the opposite effect was detected for high H concentrations. It should be noted also that the energy of segregation can be different for different sites in the GB and the values obtained from experiments are averaged quantities **[Kirchheim 1993]**. Thus, the effect of GB segregation on the rate of GB diffusion depends on many parameters such as the solute concentrations or the GB structure. Furthermore, the segregation phenomenon is anisotropic as the GB diffusion, which complicates more the situation.

2.4. Anisotropy and orientation dependence of GB diffusion

The anisotropy of GB diffusion was first investigated by Hoffman **[Hoffman 1956]**, by analyzing self-diffusion along [001] tilt GBs in Ag. According to this study, low misoriented boundaries exhibit strong anisotropy, with diffusion along boundaries being a factor of 15 faster than diffusion across them. This anisotropy has been explained by the presence of dislocations in small angle boundaries. However, diffusion in high angle boundaries was found also to be anisotropic but with a lower degree. These results suggest that even high angle boundaries have some kind of structure and thus rejecting the idea of amorphous boundaries. Sommer *et al.* **[Sommer 1989]** have found similar results by measuring self-diffusion in Ag bi-crystal with a [001] symmetrical tilt GB. As shown in Fig. 19, the diffusion in the direction parallel to the tilt axis is faster than that in the direction perpendicular to it.

This study confirmed also the GB orientation dependence of GB diffusion, as shown first by Hoffmann.

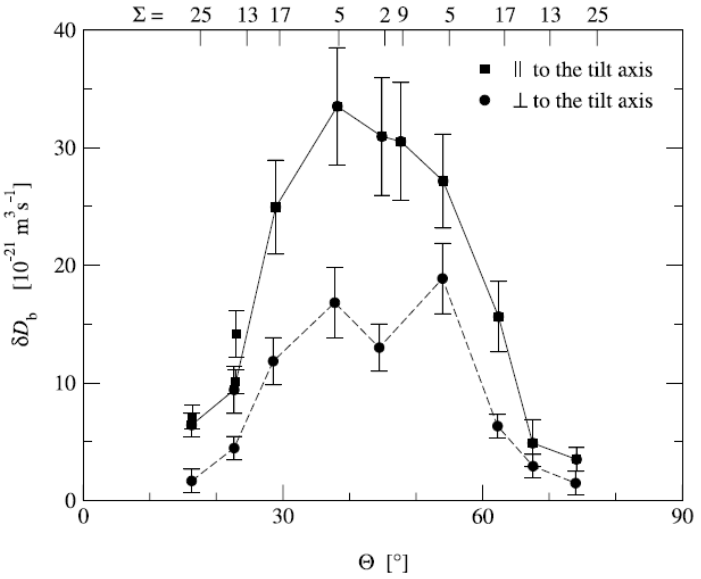

Fig. 19 - Orientation dependence of self-diffusion in [001] symmetrical tilt grain boundaries in silver at T = 771K **[Sommer 1989]**.

The anisotropy and the orientation dependence of GB diffusion are both related to the GB structure and the atomic mechanisms of GB diffusion. Experimental investigations on well characterized bi-crystals have been generally conducted to understand the structure dependence of GB diffusion **[Budke 1996, Surholt 1998, Klugkist 2001]**. However, it is difficult to determine experimentally the implicated GB diffusion mechanisms at the atomic scale. With the exponential growth of computer power, atomistic computer simulations can be an alternative to gain such information.

2.5. Atomistic computer simulations of GB diffusion

Atomistic methods such as Molecular Dynamics (MD) or Kinetic Monte Carlo have been used for both understanding the diffusion mechanisms in GB and calculating diffusion coefficients within the GB **[Ma 1993, Sørensen 2000, Suzuki 2003, Pedersen 2009, Liu 2011]**. In these methods, semi-empirical interatomic potentials based on *embedded-atom method (EAM)* are implemented to model atomic interactions **[Daw 1993]**. With the development of these potentials and the fast increasing of

computers power, it has become possible to perform MD or Monte Carlo simulations for systems containing up to millions of atoms **[Mishin 2005]**.

The atomistic modeling of GB diffusion has provided insights on the mechanisms of GB diffusion. It has been reported that GB diffusion can be dominated by either vacancy or interstitial-related mechanisms depending on the GB structure **[Sørensen 2000, Suzuki 2003]**. According to Suzuki **[Suzuki 2003]**, the anisotropy of GB diffusion depends on the GB structure and the diffusion in the direction parallel to the tilt axis can be faster or slower than in the direction perpendicular to it. This is contrary to experimental findings that have suggested that diffusion in the direction parallel to the tilt axis should always be faster.

More recently, Pedersen **[Pedersen 2009]** investigated the effect of the grain-boundary structure on the hydrogen diffusion mechanism and the hydrogen diffusion rate in aluminum, using KMC method. It was found that the hydrogen diffusion is slightly increased in the twist boundary parallel to the diffusion, due mainly to the configuration. It was observed that twist+tilt boundaries reduce the hydrogen diffusion, because of the trapping effects. However, in this study, the diffusion of only one H atom was considered. Correlations can be expected when the diffusion involves more than one H atom.

Till now we described individual properties of grain-boundary. However, a polycrystal comprises a heterogeneous ensemble of GBs with different structures and properties. Thus the experimental diffusion measurements on polycrystalline materials are affected by the whole ensemble of GBs and it is therefore more complex to understand the real contribution of grain boundaries to the effective diffusivity in the materials.

3. The effects of grain boundaries on the hydrogen effective diffusivity in polycrystalline materials

The contribution of grain boundaries to the effective diffusivity of hydrogen in polycrystalline materials is still a controversial subject. The acceleration of hydrogen diffusion along grain boundaries has been reported in several studies **[Tsuru 1982, Harris 1991, Palumbo 1991a, Brass 1996, Oudriss 2012b]**. Tsuru and Latinsson used SIMS analysis of hydrogen at GBs on the exit side of a nickel specimen cathodically pre-charged. They observed an increase of hydrogen concentrations at GBs and interpreted it as enhanced GB diffusion. The concentration profile is depicted in the Fig. 20a. This increased concentration could also be interpreted as trapping effects **[Oudriss 2012a]**. Ladna and Birnbaum **[Ladna 1987a]** used the same technic to investigate the effect of the grain boundary structure on the H distribution in Ni bicrystals and have shown the dependence of H diffusion on the

nature of grain boundaries They observed enhanced diffusion only along high energy (Σ9) but not along low energy symmetric tilt boundaries.

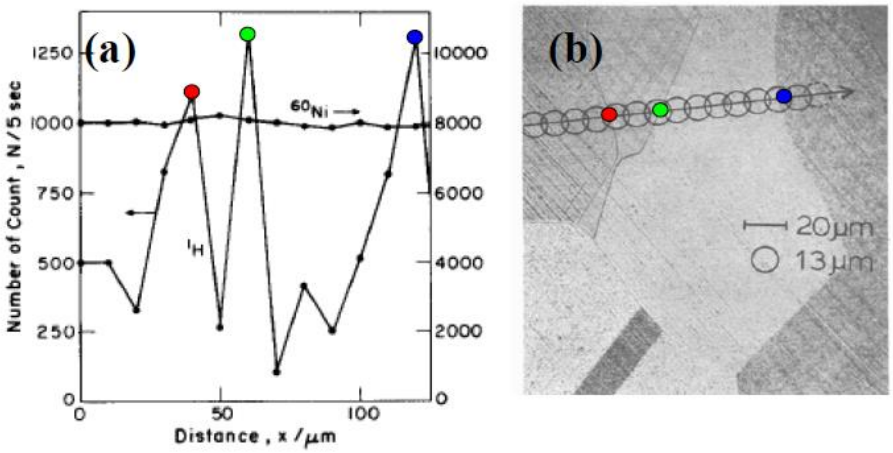

Fig. 20 - (a) Hydrogen concentration profile on the exit surface of a nickel, measured by SIMS, (b) Optical micrograph of the scanned surface.

Nevertheless, Yao *et al*. have also challenged the occurrence of fast diffusivity along grain boundaries **[Yao 1991]**. According to experimental works conducted on polycrystalline Nickel, they have concluded that GBs are not high diffusivity paths for hydrogen in nickel. In this study, it is even suggested that GBs can slow down the hydrogen transport, due to their trapping effects. These opposite behaviors can be interpreted in terms of the dependence of the GB diffusion on the structure of the boundary. The opposite contributions of GBs to the effective diffusivity could be also explained by the concentration dependence of the diffusion coefficient **[Mütschele 1987]**. The reduction in diffusivity observed by Yao **[Yao 1991]** could be due to the low hydrogen contents, whereas the increase in diffusivity noticed in the works of Harris **[Harris 1991]** could be explained by the high contents.

In order to correlate GB diffusion character and the boundary nature, Oudriss *et al*. **[Oudriss 2012b]** have conducted experiment investigations performed on polycrystalline nickel, with a large number of membranes with different grain size. In this study, it has been shown that general (or random) boundaries with high value of Σ (Σ>29) are high diffusivity paths. This high diffusivity along general boundaries is associated with their structural arrangement which gives them an excess of free volume. In other side, it has been suggested also that some LAGBs and special boundaries with low coincidence can contribute to the hydrogen diffusion enhancement, depending on their configuration and energy **[Ladna 1987a, Pedersen 2009, Liu 2011]**.

In summary, grain boundaries present a wide spectrum of local diffusivities due mainly to the large variety of their structure. This can explain the controversial interpretations of the GB contribution to the hydrogen effective diffusivity. However, it is very difficult to consider all the local diffusivities of microstructural elements when determining the macroscopic diffusivity of

heterogeneous materials. One solution is the bridging between local microstructure properties and the macroscopic behavior of heterogeneous materials, using multiscale methods. For problems in which scales are separated, multi-scale transitions are conducted using homogenization schemes. In the next section, we review the most used homogenization technics, in the framework of diffusion in polycrystalline microstructures.

III. Homogenization technics

1. Effective coefficient bounds

Homogenization methods aim to model the heterogeneous medium by an equivalent continuous medium, which is simpler and gives a good description at the macroscopic scale (Fig. 21). These methods are also tools for scale transition.

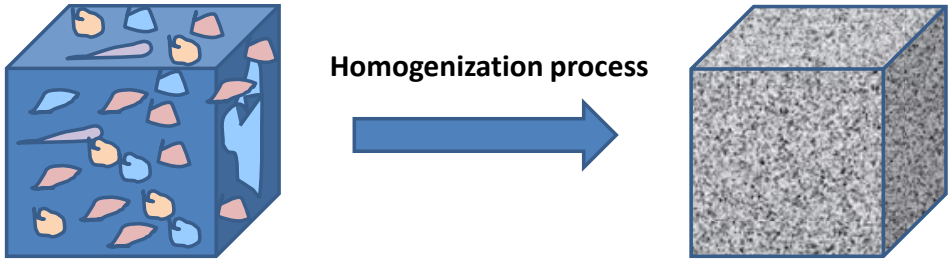

Fig. 21 - Illustration of the homogenization principle.

It is generally impossible to predict the exact analytical solutions of the effective properties for random media of an arbitrary microstructure. However, there are models of homogenization using a theoretical powerful tool, to bound the effective properties. These methods are derived using variational principles, which are based on minimizing the power dissipation in the system **[Torquato 2002, Auriault 2009]**. There are some cases with specific geometric arrangement among the phases, where the effective diffusivities can be determined.

1.1. 1st orders bounds

It can be shown (see appendix A), by applying the *Hill principle* **[Hill 1965]**, the theorem of *minimum potential energy* and considering the diffusion tensor D_{eff} homogenous and isotropic, that the effective diffusivity is bounded from above by the arithmetic mean of the phase diffusivities and from below by the harmonic of the phase diffusivities **[Auriault 2009]**:

$$\left\langle \frac{1}{D} \right\rangle^{-1} \leq D_{eff} \leq \langle D \rangle \tag{II.29}$$

These bounds are referred to as *one-point bounds* or *1st order bounds* because they depend solely on the volume fraction. They are termed generally as Voigt-Reuss bounds in the elasticity fields and Wiener bounds in the conductivity fields. For a binary composite with homogenous components of respectively volume fractions p_1 and p_2, the expression of the bounds is:

$$\frac{D_1 D_2}{p_2 D_1 + p_1 D_2} \leq D_{eff} \leq p_1 D_1 + p_2 D_2 \tag{II.30}$$

- **Upper bound: Voigt bound**

The Voigt bound **[Voigt 1887]** is reached, when the diffusion is parallel to the direction of the layers, as represented in Fig. 22.

$$D_{eff} = p_1 D_1 + p_2 D_2 \tag{II.31}$$

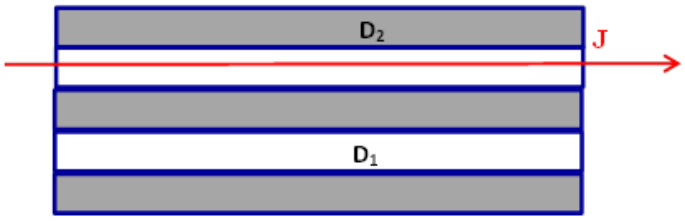

Fig. 22 - Voigt model for two phases.

- ***Lower bound: Reuss bound***

The Reuss bound **[Reuss 1929]** is realized, when the diffusion is perpendicular to the direction of the layers, as represented in Fig. 23:

$$D_{eff} = \frac{D_1 D_2}{p_2 D_1 + p_1 D_2} \tag{II.32}$$

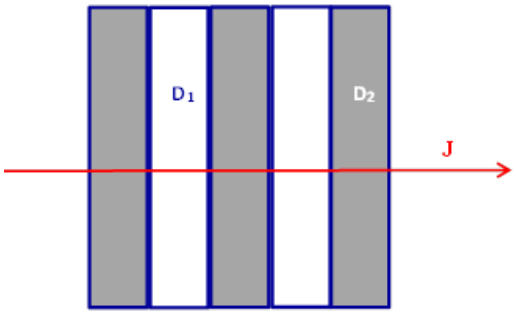

Fig. 23 - Reuss model for two phases.

1.2. 2[and] order bounds: Hashin - Shtrikman bounds

The Voigt-Reuss bounds, described above, are generally far apart from each other and their efficiency is limited in the case of laminate microstructures. Later, Hashin and Shtrickman **[Hashin 1963]** derived tighter bounds on the effective conductivity of two phase isotropic three-dimensional composites using variational principles. In analogy, the effective diffusivity D_{eff} for two-phase isotropic composite media in which $D_2 \geq D_1$, is bounded by upper and lower HS bounds:

$$D^{HS-} \leq D_{eff} \leq D^{HS+} \tag{II.33}$$

where:

$$D_{eff}^{HS^+} = D_2 + \frac{1-p}{\frac{1}{D_1 - D_2} + \frac{p}{dD_2}} \tag{II.34}$$

$$D_{eff}^{HS^-} = D_1 + \frac{p}{\frac{1}{D_2 - D_1} + \frac{1-p}{dD_1}} \tag{II.35}$$

These bounds explicitly require only the volume fractions, but are actually two-point bounds because they involve information about the microstructure **[Torquato 2002]**. The Hashin –Shtrikman bounds are reached when the type of geometry is composed of spheres embedded in a matrix, as illustrated in Fig. 24. By equivalence, grains can be represented by spheres and grain boundaries the matrix phase.

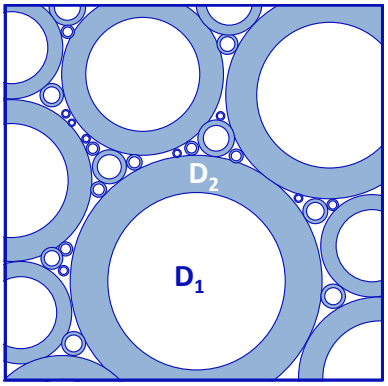

Fig. 24 - Hashin-Shtrikman model.

More rigorous bounds that incorporate nontrivial information about the microstructure have been developed in order to make the bounds narrower. A detailed description of all methods and their limitations is provided in the book of Torquato **[Torquato 2002]**. These bounds become progressively narrower as more microstructural information is included. However, terms on the microstructure are rather difficult to calculate. Therefore, an alternative solution is the popular *effective-medium approximations.*

2. Effective Medium theory

The Effective medium theory (EMT) is another class of analytical method for estimating the effective properties of heterogeneous materials. These approximations involve only simple microstructural information, such as volume fractions and inclusions shape. Here, two essential types of EMT (Maxwell's approximations and self-consistent methods) are described, in the framework of mass transport. Both methods require the resolution of the problem for a single inclusion embedded in an infinite matrix **[Torquato 2002]**. As an example, let us consider a spherical inclusion α of radius R, with a diffusion coefficient D_α. As illustrated in Fig. 25, the inclusion is placed in an infinite matrix of volume V and diffusivity D_{eff}. A concentration gradient G_0 is applied to the whole. A spherical coordinates system is considered, with *r* the radial position vector and the center of the inclusion as origin.

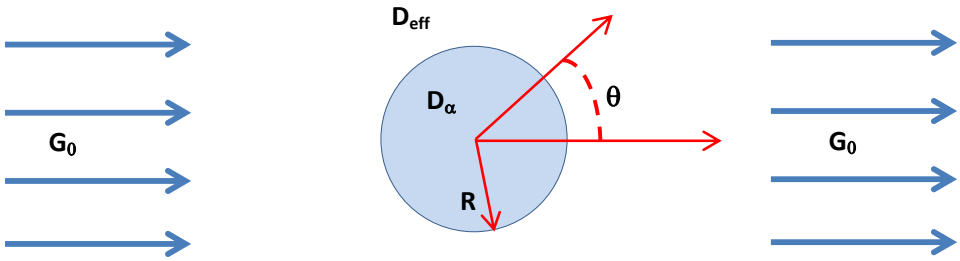

Fig. 25: Problem of single inclusion α in an infinite matrix

It can be shown (Appendix B) that the induced perturbation ΔC in the concentration field, outside the inclusion, is given by:

$$\Delta C(r) = -\frac{D_\alpha - D^{eff}}{D_\alpha + (d-1)D^{eff}} \left(\frac{R}{r}\right)^d C_0(r) \tag{II.36}$$

Where $C_0(r)$ is the concentration far from the inclusion ($r \to \infty$), d the dimensionality.

2.1. Maxwell approximations

To describe this approach, we consider a large sphere of radius R_0 composed of N smaller spheres of radius R and diffusivity D_2, as shown in Fig. 26a. The volume fraction of small spheres *p*, relative to the composite sphere, is sufficiently small, so that the interactions between them can be neglected. The composite sphere is placed in an infinite medium of the matrix material with a diffusivity D_1 and a uniform concentration gradient ∇C. The total induced perturbations in the matrix material are given by:

$$\Delta C(r) = -p\frac{D_1 - D^{eff}}{D_1 + (d-1)D^{eff}} \left(\frac{R}{r}\right)^d C_0(r) \tag{II.37}$$

with *r* the distance from the composite sphere.

If now we suppose the composite sphere as an effective single inclusion in the material matrix (Fig. 26b) and we neglect the microstructural details, the induced perturbation is given by:

$$\Delta C(r) = -\frac{D_2 - D_1}{D_2 + (d-1)D_1} \left(\frac{R}{r}\right)^d C_0(r) \tag{II.38}$$

Thus, we can deduce, by equivalence between Eq. 37 and Eq. 38, the Maxwell-Garnett's approximation for biphasic material:

$$\frac{D^{eff} - D_1}{D^{eff} + (d-1)D_1} = p\frac{D_2 - D_1}{D_2 + (d-1)D_1} \tag{II.39}$$

To summarize, this model suppose that the inclusionary phase acts as a single effective inclusion in a matrix. This method requires the existence of a matrix phase. There is no requirement of size distribution of the spherical inclusions.

It can be generalized to multiphase system, with M-1 different inclusions:

$$\frac{D^{eff} - D_1}{D^{eff} + (d-1)D_1} = \sum_i^M p_i \frac{D_i - D_1}{Di + (d-1)D_1} \tag{II.40}$$

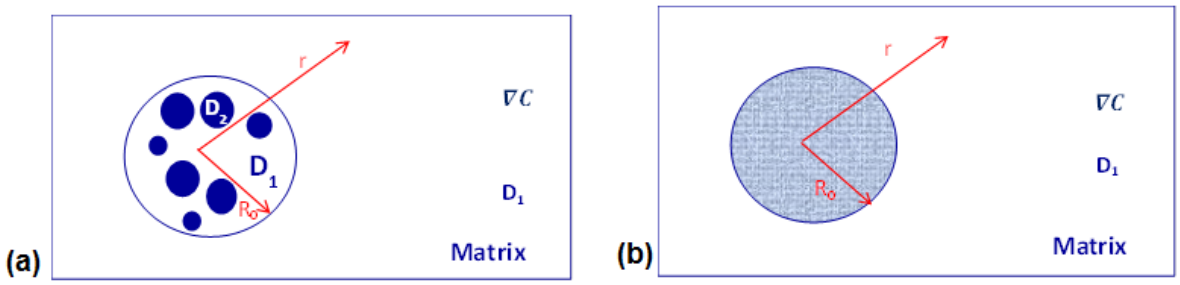

Fig. 26 - Illustration of Maxwell principle. (a) The inclusion is a large sphere of radius R_0 composed of N smaller spheres of radius R and diffusivity D_2. (b) The large composite sphere is considered as a single effective inclusion of radius R_0 in a matrix.

2.2. Self-consistent Approximations

To describe the self-consistent method, we consider a macroscopically isotropic composite aggregate composed of M different types of spherical inclusions with volume fractions p_1 and p_2, and diffusivities D_1 and D_2. The system is illustrated in Fig. 27. The idea is that each inclusion (1 or 2) sees the rest of the material as a homogenous medium (matrix) whose effective diffusivity D_{eff} is the unknown to be calculated.

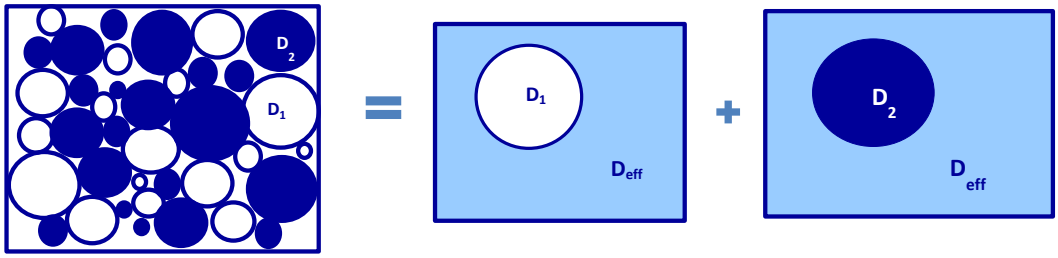

Fig. 27 - Illustration of the self-consistent principle.

The average perturbation induced by the inclusions is the superposition of the perturbation induced by individual particles:

$$\Delta C(r) = \left[(1-p)\frac{D_1 - D^{eff}}{D_1 + (d-1)D^{eff}} + p\frac{D_2 - D^{eff}}{D_2 + (d-1)D^{eff}} \right] \left(\frac{1}{r^d} \right) C_0(r) \tag{II.41}$$

Another requirement of the self-consistent method is that the average perturbation induced by all particles vanishes:

$$\Delta \overline{C}(r) = 0 \tag{II.42}$$

Thus, we can deduce the Self-consistent equation for a two components composite:

$$(1-p)\frac{D_1 - D^{eff}}{D_1 + (d-1)D^{eff}} + p\frac{D_2 - D^{eff}}{D_2 + (d-1)D^{eff}} = 0 \tag{II.43}$$

By contrast to the Maxwell-Garnet method, this is an implicit method, i.e., it requires solving an implicit equation for the effective diffusivity. It is symmetric (it is invariant to simultaneous interchanges of properties and fractions), while the previous method is asymmetric.

This equation can be generalized to multicomponent composites, containing M different phases:

$$\sum_i^M p_i \frac{D_i - D^{eff}}{D_i + (d-1)D^{eff}} = 0 \tag{II.44}$$

The different bounds of the models, described above, are compared in Fig. 28. A binary composite, with diffusivities D_2 and D_1 ($D_2 > D_1$) is considered, with p_1 the volume fraction of the phase 1. For the low contrast of diffusivities, the different bounds are closer and can give useful information on the effective diffusivity. Hashin-Shtrickman bounds are restrictive and tighter than the Voigt/Reuss bounds in all cases. We notice that the self-consistent prediction is located inside the bounds. For the high contrast diffusivities, the different bounds are distant and thus their utility is limited in that case.

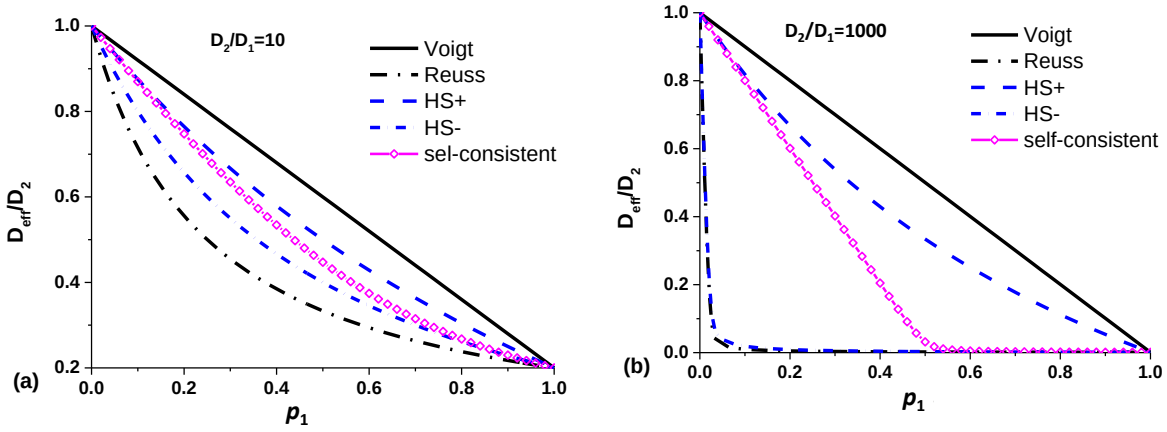

Fig. 28 - Effective diffusivity bounds for two different cases: (a) low and (b) high phase diffusivity ratio.

In summary, the applicability and the efficiency of the classical homogenization technics depend mainly on the type of geometry considered and also the contrast of different phase properties. These models are practical but for complex microstructures their predictions are not efficient. However, in the framework of the effective medium theory, more sophisticated approximations that incorporate microstructural details can be established **[Torquato 2002]**. But their use is not practical because of their complex analytical expressions that are almost impossible to compute **[Torquato 2002]**. An alternative idea proposed by Chen **[Chen 2008]** is to improve the classical effective medium approximations by including concise information about the topology of the heterogeneous microstructures. For that, grain-boundary networks characterization is a key point to achieve more realistic description of the macroscopic effective diffusivity. In the next section, we present a review on the GB network characterizations and the most applied tools.

IV. Grain-boundary networks and effective properties

Beyond the role played by individual boundary, it is important to analyze the grain boundary network effect on the effective diffusivities of polycrystalline materials. Many studies have shown that the grain boundary characters distribution strongly influence the mechanical and functional properties of polycrystalline materials **[Watanabe 1984, Wells 1989, Lehockey 1997, Watanabe 1999, Yamaura 2003, Tsurekawa 2006]**. In the early 1980s, Watanabe **[Watanabe 1984]** proposed the concept of the grain boundary engineering (GBE) for the development of high performance polycrystalline materials. In the framework of this concept, Watanabe has introduced statistical factors, such as the grain boundary character distribution (GBCD) and the grain boundary connectivity, as criterions for classifying microstructures. Since then, the control of GBCD, by increasing the population of special boundaries, using thermomechanical process, has been used in order to improve mechanical and functional properties of polycrystalline materials **[Lehockey 1997, Tsurekawa 2000, Shimada 2002, Kobayashi 2005]**. However, it was pointed out that the connectivity of grain boundaries can be a key factor, such as GBCD, in order to fully understand and control the grain boundary related phenomenon **[Watanabe 1994]**. Several studies have been devoted to the characterization of the grain-boundary connectivity in polycrystals, using different parameters, such as percolation metrics, triple junction types or twin clusters **[Wells 1989, Palumbo 1991b, Romero 1996, Minich 2002, Frary 2004]**. In this section, we first introduce the percolation theory which has been used to evaluate quantitatively the grain boundary characters distribution. Then we review the grain boundary connectivity characterization.

1. Basic concept of the percolation theory

1.1. Definition of the percolation theory

Percolation is the study of the macroscopic connectivity of discrete objects randomly connected to each other **[Broadbent 1957]**. It is applied in different domains like phase transitions (physics), forest fires, epidemics, fracture etc... To introduce the concept, the example in two dimensions, in Fig. 29, is used. Some cells of the grid are populated by dots. Some of these fall into neighboring cells. A cluster is a set of sites connected by a nearest-neighbor relationship. If occupied neighboring cells are connected (vertical or horizontal links) they form clusters (red, green). These clusters have different sizes. This example is called site percolation.

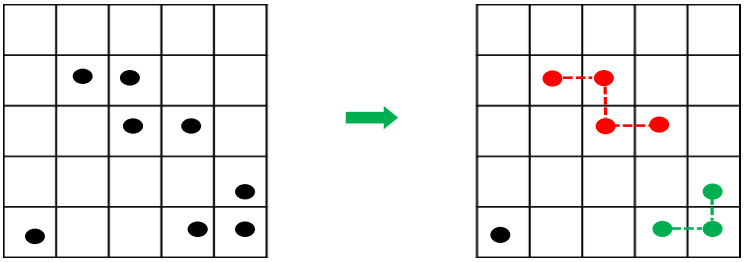

Fig. 29 - Illustration of the formation of clusters in a square lattice.

There are two types of percolation based on the nature of the sites. When the sites are bonds or lines, as shown in the Fig. 30a and Fig. 30b, it is called bond percolation. Each bond has a probability *p* to be "closed" or "opened", "resistant" or "susceptible". The terms depend on the field of enquiry.

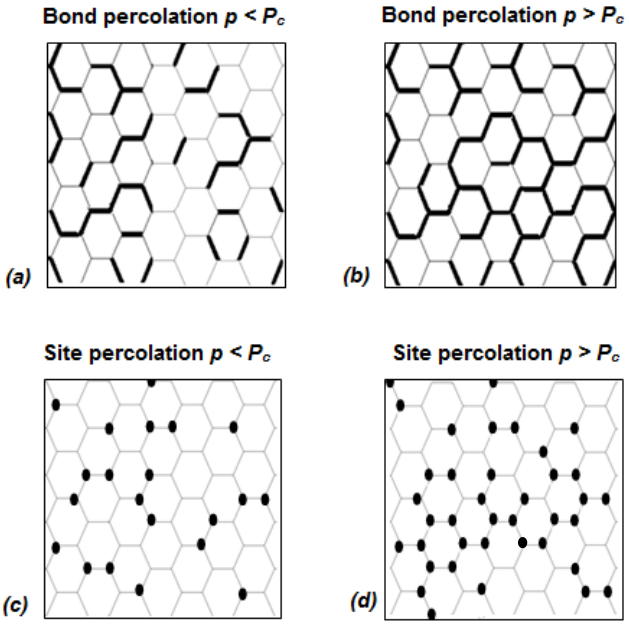

Fig. 30 - Illustration of discrete lattice percolation on a hexagonal lattice. (a) and (b) show a bond percolation connectivity (occupied bond are in black lines) below and above percolation threshold P_c, respectively. (c) and (d) illustrate a site percolation connectivity (occupied sites are in black) below and above percolation threshold P_c, respectively.

1.2. Percolation threshold P_c

There is a critical concentration P_c (of occupied sites or opened bond) above which a cluster exists that spans the domain. This critical concentration or fraction is referred to as the geometric percolation threshold. As illustrated in Fig. 30, when *p* is low (lower than P_c), there are only some disconnected small clusters and when p is sufficiently high ($p>P_c$), a large tortuous cluster which connects opposite sides, emerges. It is called a percolating cluster. Again, the percolation threshold corresponds to the fraction $p=P_C$ at which the percolating cluster appears for the first time. This threshold is directly linked to the system connectivity and its numerical value depends on many parameters such as the

correlation type (bond or site) or the lattice type for a given dimensionality. The numerical values of the percolation threshold are determined for an infinitely large system with random occupations and they are only approximations, except for few two-dimensional lattices (Table I). For a hexagonal 2D lattice, the percolation threshold P_c=0.6527 for bond percolation and P_c=0.6962 for site percolation **[Stauffer 1994]**. The *percolation threshold* for site percolation is always larger than for bond percolation.

Table I : Numerical values for percolation threshold

Lattice	Bond percolation	Site percolation
Honeycomb	2sin(π/18)* (~= 0.65271)	0.69620
Square	1/2 *	0.59275
Triangular	1-2sin(π/18)* (~= 0.34729)	1/2 *

* Exact results

For finite size system, such as ones simulated on computer, the determined numerical value of the percolation threshold is not the exact value. This difference is due to the finite size effect. In order to rid from this effect and get the universality of the results at the critical fraction, one must increase the size of the system. As shown in the experimental works of Clerc **[Clerc 1983]** on electrical percolation, when the system size is not sufficiently large, there is not one definite percolation threshold but instead several values at which a percolating cluster can be obtained. In Fig. 31 is shown the conduction probability $F_n(p)$ and the transition zone (the range of the possible values of percolation threshold) as a function of the network size N. As the system size is increased towards infinity, the width of the transition zone decreases to zero and the calculated value approaches the theoretical threshold P_C.

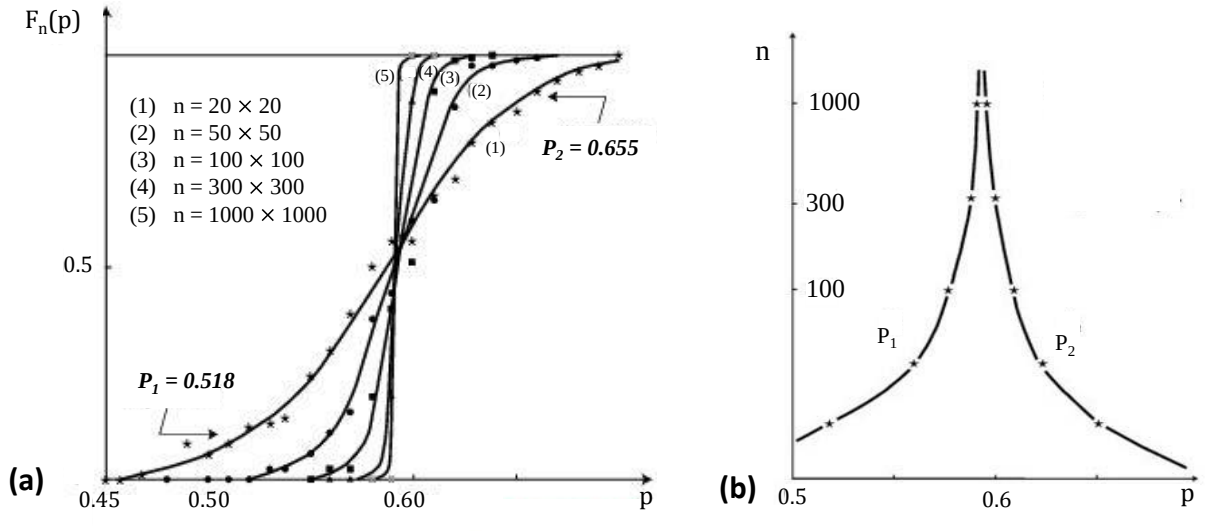

Fig. 31 - (a) Conduction probability as a function of the network size. (b) Transition zone and the network size **[Clerc 1983]**.

1.3. Percolation quantities and scaling laws

In addition to the percolation threshold, several other quantities were defined in order to characterize the topological properties of the percolation networks **[Stauffer 1994]**. Two of the most important quantities are:

- The percolation probability *P(p)*. This quantity is the probability that a given site belongs to the percolating cluster, with *p* the fraction of occupied bonds.
- The correlation length ξ(*p*). This is the typical radius of the connected clusters for $p < P_c$ and the maximum size of the "holes" inside the percolating cluster for $p>P_c$.

Like most of the percolation quantities, these two quantities obey scaling laws, around the percolation threshold P_c. This means that they are insensitive to the networks structure and its microscopic details. This insensitivity leads to scaling laws, near P_c:

$$P(p) \propto (p - P_c)^{-\beta} \tag{II.45}$$

$$\xi(p) \propto (p - P_c)^{-\upsilon} \tag{II.46}$$

The parameters β and υ, referred as to *universal exponents*, are independent of the microscopic details of the system and depend only on the dimensionality, for sufficiently large system **[Sahimi 1994]**.

Table II : Values of universal exponents β and υ for different dimensions

Exponent	d=2	d=3
β	5/36	0.41
ν	4/3	0.88

Percolation theory provides powerful tools to study the connectivity of a network, with a random distribution of properties. However, this is a probabilistic approach and its application on grain-boundary networks is not automatic because of the possible correlations in polycrystalline materials **[Priester 2006]**.

2. Characterization of grain-boundary network topology and connectivity

A number of numerical and experimental studies have been devoted to the characterization of grain-boundary networks distribution and connectivity of polycrystalline materials, using different tools such as percolation metrics, triple junction types or homology metrics **[Wells 1989, Romero 1996, Kumar 2000, Minich 2002, Alexandreanu 2003, Schuh 2003a, Schuh 2003b, Frary 2004,**

Rohrer 2010]. Wells *et al.* **[Wells 1989]** determined a percolation threshold of 77% for 3D grain boundary networks modeled by tetrakaidecahedrons, using random bond percolation. From experimental observations, the same authors have found that intergranular failure was possible when the proportion of sensitized (active) grain boundaries reached 23% for the 304 stainless steel. However, Schuh *et al.* **[Schuh 2003b]** have shown that the use of the percolation theory with the assumption of random distribution of GB characters was not appropriate. By considering crystallographic constraints on 2D and 3D grain boundary networks, they have found that the percolation threshold for resistant grain boundaries was much higher than in randomly assembled networks. They have calculated a percolation threshold of resistant boundaries above 50%, whereas in random percolation theory the predicted value is around 35% **[Stauffer 1994]**. Thereafter, they have also shown that the fraction of special boundaries is not a reliable predictor of the connectivity. Instead, they have found that the distribution of triple junctions was a more appropirate criterion for the classification of grain boundaries in the framework of the GBE. According to the nature of the grain boundaries which form a triple junction can be classified into four types: 0-CSL, 1-CSL, 2-CSL and 3-CSL **[Fortier 1995, Fortier 1997]**. The probabilities of formation of these four types of triple junctions, termed as to J_0, J_1, J_2 and J_3, respectively, are given by:

$$J_0 = (1 - f_\Sigma)^3 \tag{II.47}$$

$$J_1 = 3 f_\Sigma (1 - f_\Sigma)^2 \tag{II.48}$$

$$J_2 = 3 f_\Sigma^2 (1 - f_\Sigma) \tag{II.49}$$

$$J_3 = f_\Sigma^{\,3} \tag{II.50}$$

Schuch *et al.* proposed Monte Carlo model that relates the fraction of special boundaries ($\Sigma 3^n$ type) f_Σ and the proportion of different types of triple junctions **[Schuh 2003b, Frary 2004]**. In this model, a parameter A, termed as "constraint parameter", is introduced. This parameter represents the ratio between the fraction of Σ3 grain boundaries $f_{\Sigma 3}$ and the total fraction of Σ grain boundaries ($f_\Sigma = f_{\Sigma 3}/A$). In the Fig. 32, the analytical predictions of this model with different values of the correlation factor A and experimental data **[Randle 1999, Kumar 2000, Schuh 2003a, Oudriss 2012b]** are compared.

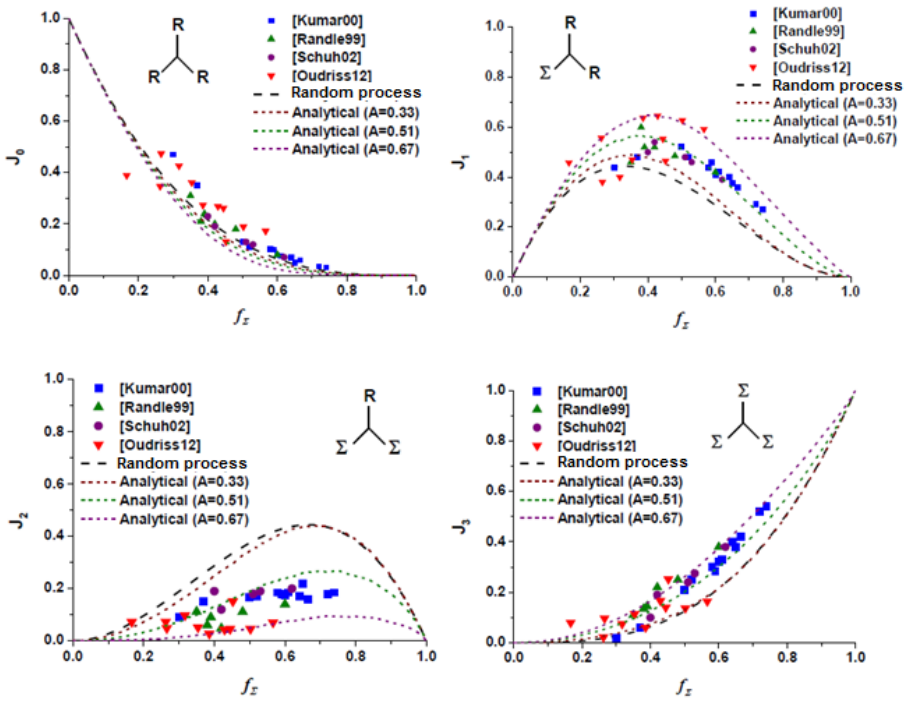

Fig. 32 - Probability J of presence of each triple junction type as a function of the special grain boundary fraction. **[Oudriss 2012a, Legrand 2013a]**

The experimental triple-junctions distributions are relatively well described, depending on the value of the parameter A. The latter, which is measure of twin-boundary prominence, depends on the processing history and the material properties.

More recently, Wanner **[Wanner 2010]** introduced a new approach, by using homology metrics, to characterize GB networks connectivity in simulated networks. Rohrer *et al.* **[Rohrer 2010]** applied this method to characterize real materials and to evaluate the connectivity of boundaries in plan sections of cubic materials. In this study, the authors used two topology metrics, referred as to B_0 and B_1. In two dimensions, B_0 measures groups of GBs not connected to the rest of the networks and B_1 measures continuous, closed paths of grain boundaries. As an example, three insets of disconnected GB cluster, which are counted in B_0, are shown in Fig. 33.

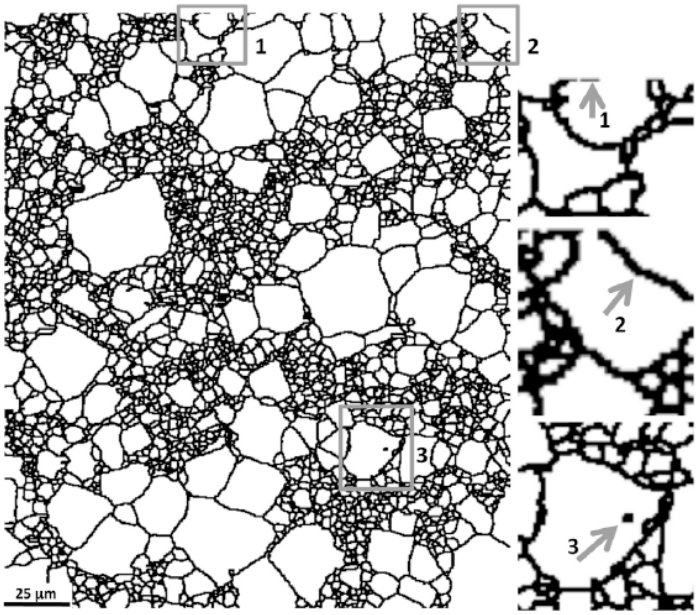

Fig. 33 - Grain boundary map for the bimodal $SrTiO_3$. The three insets show details that create disconnected pieces of the network and increase B_0 above one. (1) A tangential boundary on the edge, (2) a boundary crossing a corner of the image, (3) an island grain **[Rohrer 2010]**.

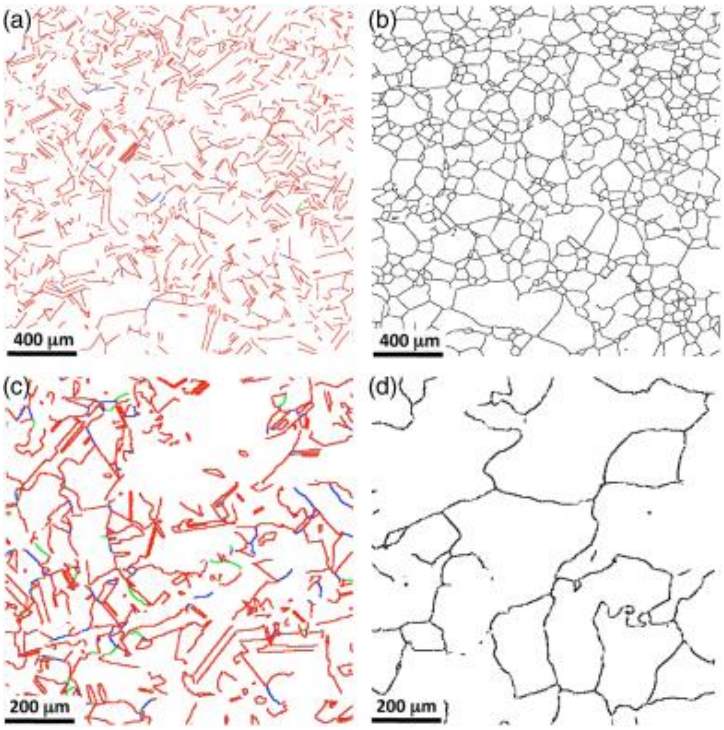

Fig. 34 - Grain-boundary maps for the Ni samples. (a) All of the $\Sigma 3^n$ boundaries in the low $\Sigma 3$ Ni, β_{01}=3.1, (b) all of the non-$\Sigma 3n$ boundaries in the low $\Sigma 3$ Ni, β_{01}=0.12, (c) all of the $\Sigma 3^n$ boundaries in high $\Sigma 3$ Ni, β_{01}=0.53, (d) All of the non $\Sigma 3^n$ boundaries in high $\Sigma 3$ Ni, β_{01}=8.6. In (a) and (c) the $\Sigma 3$ boundaries are colored red, the $\Sigma 9$ boundaries are blue and the $\Sigma 27$ boundaries are green **[Rohrer 2010]**.

By analyzing four different microstructures, they demonstrated that the ratio of B_0 to B_1, termed the inverse connectivity β_{01}, can be an accurate metric parameter for the network connectivity. As an example, the comparison of two different Ni microstructures (reference and grain-boundary engineered) is shown in Fig. 34. In the reference sample, the network of Σ3 boundaries (Fig. 34a) is highly disconnected, that is reflected in a value of the inverse connectivity greater than one. In contrast, the network of non- Σ3 boundaries (Fig. 34b) are relatively well connected which is characterized by an inverse connectivity smaller than one. It is the reverse for the grain-boundary engineered sample (Fig. 34c and Fig. 34d). In addition to the connectivity, this parameter is sensitive to the grain size, the presence of twins or to the misorientation distributions. However, this method requires knowledge of the crystal orientations, unlike previous methods. Hence a 3D analysis is necessary in order to correlate with material properties **[Rohrer 2011]**.

In summary, different tools have been applied to characterize grain-boundary network topology and connectivity in simulated or real microstructures. But studies that correlate grain-boundary structure with the effective diffusivity are rare. Chen and Schuh **[Chen 2006]** have proposed a composite model, with two types of boundaries, that predict effective GB diffusivity in connection with GBs network structure. However, their approach, by neglecting the volume diffusion, is limited to the grain-boundary effective diffusivity, corresponding to one type (Regime C) of Harrison kinetics **[Harrison 1961]**. Mass transport in real materials is more complex because diffusants can travel from the grain boundaries to the grains and vice versa. A realistic model needs to consider both, the diffusion in the volume and in the GBs and the GB connectivity.

V. Summary

In this chapter, we introduced the important role of hydrogen in the HE mechanisms. Then we reviewed the hydrogen diffusion in polycrystalline materials and its interaction with microstructural defects. We pointed out that the extracted data from permeation experiments can be influenced by the microstructure parameters, such as the trapping or the presence of grain boundaries. The latter present a wide variety of diffusion properties, depending on their structure and can influence strongly the hydrogen effective diffusivity in polycrystalline materials. However, their contribution to the macroscopic diffusivity is not fully understood and can lead to some controversial effects on the experimentally measured diffusivities. As highlighted in this chapter, the volume fraction and spatial positions of different families of grain boundaries are both important parameters for the understanding and the good evaluation of the GB diffusion contribution to the macroscopic diffusivity.

Chapter 3

Hydrogen diffusion in simulated heterogeneous aggregates

In the second chapter, it has been pointed out that grain boundaries can exhibit different behavior, depending on their structure. It has been highlighted particularly that the diffusivity is higher along random HAGBs than along LAGBs and CSL HAGBs. This chapter is aimed at investigating the effects of grain-boundary networks topology and connectivity on the macroscopic diffusivity. To do that, hydrogen permeations through polycrystalline aggregates are simulated, in two and three dimensions. Then the correlations grain-boundary connectivity and the macroscopic diffusivities are investigated. In addition, a homogenization approach that considers the percolation behavior of the diffusion is proposed.

Introduction

There are an important number of studies concerning the prediction of the effective diffusivity in heterogeneous materials **[Hart 1957, Bokshtein 1958, Levine 1960, Belova 2003, Chen 2006, Chen 2007, Legrand 2013b, Deng 2014, Jothi 2014, Lacaille 2014]**. However, in most of them, the intergranular region is modeled by one single homogeneous phase, characterized by an effective intergranular diffusivity. To our knowledge, studies that consider the influence of GB variety on the effective diffusivity are rare **[Chen 2006, Deng 2014]**.

Chen and Schuh **[Chen 2006]** investigated the influence of GB connectivity on the macroscopic diffusivity, using a two-dimensional honeycomb lattice. In their work, the authors have shown that, when the diffusivity contrast between grain boundaries of different characters is greater than four orders of magnitudes, the macroscopic diffusivity is governed by the percolation behavior of high-diffusivity boundaries. However, in their approach, only type-C kinetics **[Harrison 1961]** is considered, by neglecting mass transport through the grains.

More recently, Deng *et al*. **[Deng 2014]** conducted a similar study in three-dimensions, using kinetic Monte Carlo model. They confirmed the results obtained by Chen and Schuh **[Chen 2006]** in two-dimensions, the only difference being that the dimensionality affects the percolation threshold. In addition, they found that in the kinetic limit when GB diffusion is the dominant transport mechanism, the effective diffusivity through a polycrystalline sample does not depend on the grain size.

In both studies, the established correlation between the GB network connectivity and the effective diffusivity is based on an assumption that the diffusion takes place only along the GBs. However, this does not stand in reality: diffusion process is not restricted within the GBs. It only happens at very low temperatures or for extremely short times of diffusion, which is rarely the case for the experimentally determined hydrogen effective diffusivities in polycrystalline materials. In addition, it is has been shown that the diffusion in GBs can be reduced by more than one or several order of magnitude compared with the crystal, because of the trapping **[Pedersen 2009]**. Therefore, polycrystalline materials can be regarded as a composite media with heterogeneous GBs networks embedded in intragranular matrix.

To study hydrogen diffusion in heterogeneous polycrystalline materials, our approach consists of modeling microstructures by a ternary continuous composite that contains a grain phase and two types of boundaries: random grain boundaries (RGBs) and special grain boundaries (SGBs). Compared to the bulk diffusivity, the RGBs are attributed a higher diffusivity, while the SGBs are characterized by a slower diffusivity in order to take account of the retarding effect of the trapping.

The purpose of this chapter is to examine the influence of the GB networks on the macroscopic diffusivity, by modelling H-permeations in simulated 2-D and 3-D polycrystalline aggregates. We first

describe the computational procedure used in this work. Then, a morphological characterization of the 2-D GB networks is presented, by determining the topology and connectivity parameters. Finally, the correlations between the GB connectivity and the macroscopic diffusivity are analyzed in 2-D and 3-D.

I. Computational procedure

To study hydrogen diffusion through a metallic membrane, permeations tests were simulated, using the finite elements method (FEM) software Comsol Multiphysics © associated with the computing code Matlab®.

1. Introduction to the FE simulation with Comsol Multiphysics©

The Comsol module for the transport of diluted species interfaces was used to solve the hydrogen diffusion in the modelled polycrystalline microstructure. This module provides a predefined modeling environment for studying the evolution of chemical species transported by diffusion and convection. As most of the multiphysic simulations, the transport phenomenon of chemical species is governed by partial differential equations (PDEs). By default, the PDE equation is implemented in Comsol as a weak form PDE. This consists in transforming the PDE into an integral form, which is less strict than the PDE and more practical with the FE method. This derivation procedure involves the use of arbitrary functions, called test functions.

After defining the boundary conditions of the problem and the geometry meshing, the model is ready to be solved. To do that, Comsol first proceeds to the spatial discretization, using the FE method. This means that any arbitrary function defined in the geometry is approximated by a set of local functions referred to as shape functions. The FE discretization is based on a particular choice of the shape functions. These functions are defined using polynomials on each element of the mesh. They are associated with the nodes of the elements and must verify some properties such as to be continuous and non-zero only on the elements containing their attachment node. The Lagrange shape functions are used by default in this Comsol module. The FE discretization results in a system of equations that, once resolved, give an approximation of the exact solution of the PDE. Comsol assembles the system of equations to be solved in a matrix. The size of this matrix determines the number of degrees of freedom (DOFs) of the model.

To solve the linear system of equations, Comsol chooses the optimized solver by default, depending on the physics, space dimensions and the type of study. However, one can choose different solver. There are two types of solvers available in Comsol: iterative solvers and direct solvers. The main advantage of iterative solvers is the memory use, which is low compared to others methods. Direct methods generally offer a very

good robustness but their computation cost and memory use can be high. In this work, the default direct solvers were used, namely PARDISO and MUMPS.

The accuracy of the FE results depend on many parameters, such as the mesh size, the type of elements or the order of the shape functions. A key point in the FE method is *the quality of the mesh:* the finer the mesh is, the higher fidelity FE solution has. However, the increase of the mesh elements leads to a high number of DOFs. This implies significant computation cost, especially for very large 3D models.

2. Diffusion in simulated microstructures

2.1. Polycrystalline microstructures modeling

2.1.1. 2-D hexagonal geometry

The microstructure is modeled with hexagonal grains surrounded by grain boundary phases (Fig. 35). For computational convenience, it was considered necessary to define a representative volume element (RVE) of the macroscopic heterogeneous microstructure, as shown in Fig. 35. The dimensions of the RVE membrane are the thickness e_m and the height h_m. The ratio between the RVE membrane size e_m and the grain size λ is taken high enough to avoid the membrane size effects. Indeed, it has been shown by Legrand *et al*. **[Legrand 2013b]** that, below a critical value of the ratio e_m / λ, the effective diffusivity is determined by the membrane thickness.

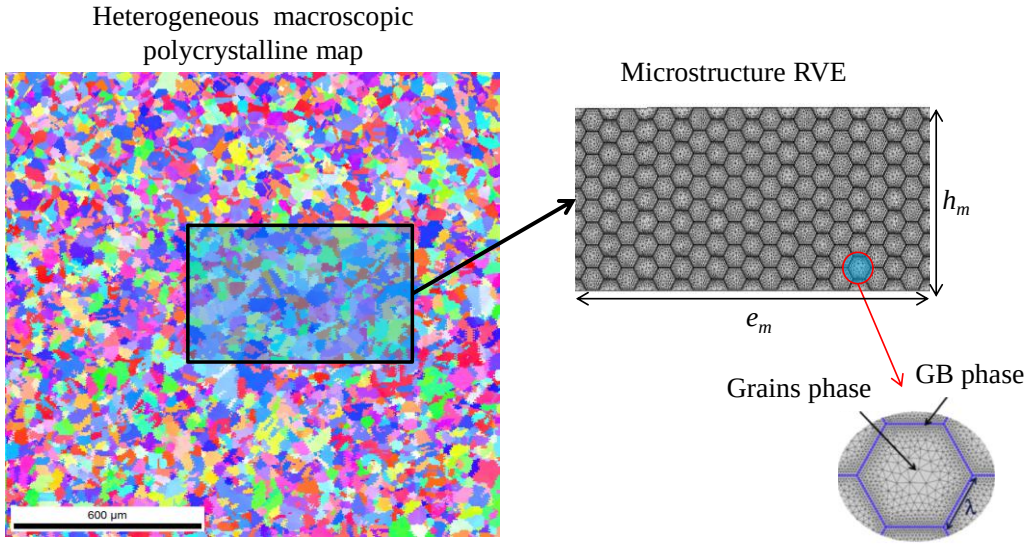

Fig. 35 - Heterogeneous polycrystalline EBSD map and the RVE model with grains of hexagonal shape. e_m and h_m are the thickness and height of the microstructure RVE and λ the grain size.

2.1.2. 3D geometry

The microstructure is simulated by grains with truncated-octahedron shape, surrounded by an intergranular phase. A 3-D unit cell is first constructed, as shown in Fig. 36. This unit cell is then repeated in the three different directions to form the membrane. Two different polycrystalline aggregates were considered in this study. In one (Unit cell A in Fig. 36), the grain boundaries are modeled by one single homogenous phase with high diffusivity, while in the other (Unit cell B in Fig. 36), the intergranular phase is composed by different entities that can be assigned different diffusion properties (grain boundaries, triple junctions). Models built with the unit cell B require a larger amount of mesh elements than those built with the unit cell A to reach statistical stability. This point will be discussed in the next section. The size of membrane is controlled by the number of unit cell in each direction (n_x, n_y, n_z). The Fig. 37 illustrates the geometry of the different components of the simulated microstructure.

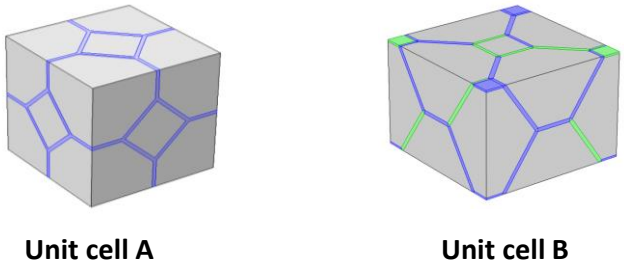

Fig. 36 – Unit cells of the two pollycristalline aggregates models

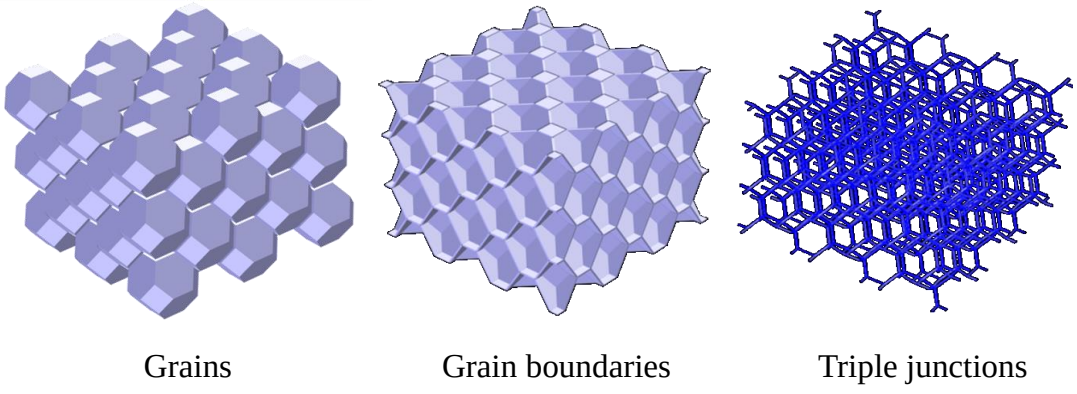

Fig. 37 – Illustrattion of the different microstructural entities modelled in this study

2.2. Hydrogen permeation modeling

2.2.1. Problem setting

The diffusion problem with the boundary conditions is illustrated in Fig. 38 and Fig. 39. To simulate hydrogen permeation tests, we impose a constant hydrogen concentration C_0 at the entry side of the membrane, and zero at the exit side. Thus a concentration gradient is established from the left to the right. We consider a transient diffusion and C_0 remains constant during the permeation process. The initial hydrogen concentration inside the membrane is zero.

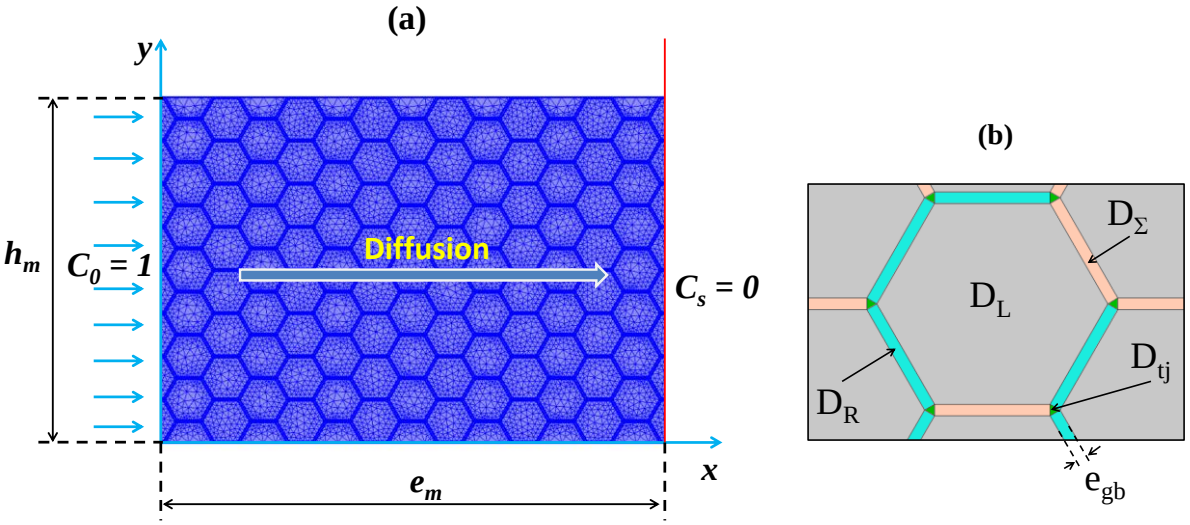

Fig. 38 – (a) - Scheme of the model with the boundary conditions and the parameters of the model. (b) – Spatial distribution of diffusion coefficients.

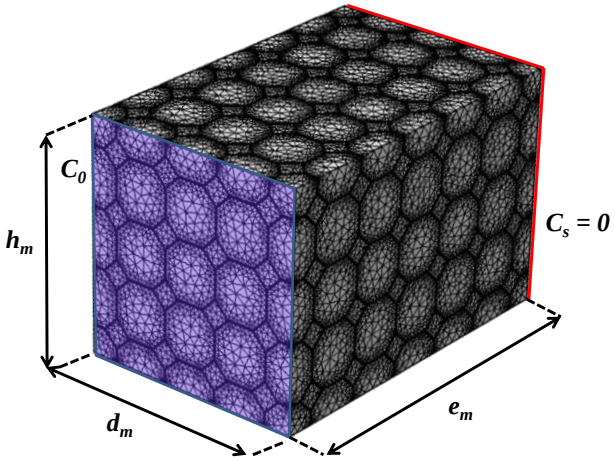

Fig. 39 - Scheme of the model with the boundary conditions and the geometric sizes

The hydrogen diffusion is governed by the classical Fick's equation (III.1), with a diffusion coefficient D_i, depending on the phase. The membrane is considered isotropic, so that the diffusivity tensor can be reduced to a single diffusion coefficient for each phase.

$$\frac{\partial C}{\partial t} = \nabla \cdot (D_i \nabla C) \tag{III.1}$$

We assume that the hydrogen concentration is symmetric at the top and bottom lines of the membrane. That means no mass flux in the normal direction *n* across the boundary:

$$-n \cdot (-D_i \nabla C) = 0 \tag{III.2}$$

The grain boundary diffusivity depends on the boundary type. First, the boundaries are randomly classified into RGBs and SGBs by defining the fraction of RGBs f_R as input parameter. The Mersenne twister algorithm implemented in Matlab has been used as a random number generator. Then, RGBs are assigned a high diffusion coefficient D_R and SGBs a low diffusion coefficient D_Σ. The subscripts R and Σ are associated respectively with RGBs and SGBs. All the grains have the same diffusivity D_L. For simplicity, we considered that the diffusivity of a triple junction is determined by the types of GBs surrounding it. For instance, a triple junction surrounded by at least two RGBs, is assigned a high diffusivity D_R.

2.2.2. Extracted data

To calculate the effective diffusion, the same method as the experimental measurements is applied. This method has been described in the second chapter. The aim is to obtain the characteristic time $t_{10\%}$ that is required to reach 10% of the steady-state flux J_{max}. For that, the evolution of the flux at the exit side of the membrane as a function of time is calculated. As the membrane is heterogeneous, an average flux over all points at the exit side is determined using equation (III.3) in 2-D and equation (III.4) in 3D:

$$\overline{J_{exit}(t)} = \frac{1}{h_m} \int_0^{h_m} J_{exit}(y,t)\,dy \tag{III.3}$$

$$\overline{J_{exit}(t)} = \frac{1}{d_m \times h_m} \int_0^{d_m} \int_0^{h_m} J_{exit}(y,z,t)\,dz\,dy \tag{III.4}$$

From the evolution of the average flux as function of the time, one can estimate the characteristic time $t_{10\%}$, which then allows to calculate the effective diffusivity with the relation (III.5) :

$$D_{eff} = \frac{e_m^2}{15.12 \times t_{10\%}} \quad \text{(III.5)}$$

2.3. Meshing

2.3.1. Meshing of the 2D hexagonal aggregates

The grain phase was meshed by triangle elements and the GB phase by quadrilateral elements, as shown in Fig. 40. The mesh was refined near the GB phase and a minimum of two elements has been imposed on the thickness of every GB. The total number of elements depends on the contrast between GB thickness and the grain size. A total number of 4.24×10^6 elements were reached for the highest contrast.

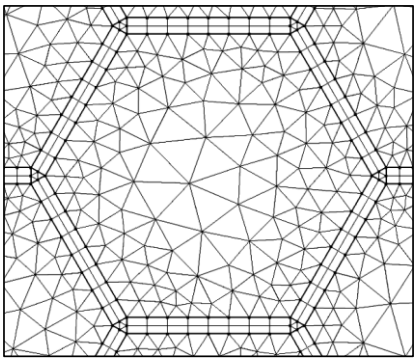

Fig. 40 - Illustration of the applied mesh.

2.3.2. Meshing of the 3D aggregates

To build the mesh, Comsol uses by defaults a physic-controlled mesh with predefined parameters. This is the simplest way when one is working on 3D complex geometry. If the mesh is not good enough, some of the predefined parameters can be modified such as the mesh size. The latter can be controlled using a scale parameter with nine levels, going from extremely fine to extremely coarse mesh. Comsol provides also mesh statistics that allows making a balanced choice between the element quality and the number of elements. Among the different parameters, the minimum element quality statistic is an indicative of the mesh quality. A value greater than 0.1 is generally sufficient.

However, the default mesh algorithm uses the same settings for all elements within the model. This solution does not provide optimal mesh for complex geometries with some edges or surfaces that have largely different sizes relative to the other edges and surfaces defining a domain. This is the case for the models built with the unit cell B, where the different intergranular entities, such as the grain-boundary and the triple junction networks, are composed by edges and surfaces with high contrast dimensions. Depending on the grain size, dimensions of some edges of surfaces can differ over one hundred times. This results in a bad

meshing quality. To illustrate this point, we present, in Fig. 41, a comparison of the mesh characteristics between the patterns of the unit cells A and B. It can be seen that the mesh is less optimized in the unit cell B. To go further, the minimum element quality distribution of the mesh in the unit cell is depicted in Fig. 42. We observe that the element quality is poor in the intergranular regions. This is due mainly to the high difference in the dimension sizes of the edges and surfaces but also to the presence of quadruple nodes that have sharp and narrow corners. To improve the mesh, one option is to adapt the mesh parameters around the regions with small size domain. However, it is complex and it might not lead to a very optimal mesh, due to the extremely large number of domains in our model. Thus we decided to use an overall refinement of the model. This option results in a very large amount of finite elements for large size models and thus an important memory use for the computation.

Unit cell A

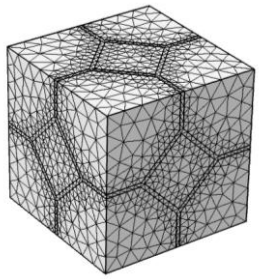

Number of tetrahedral elements: **46782**

Minimum element quality: 0.1061

Unit cell B

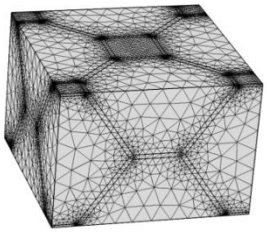

Number of tetrahedral elements: **143707**

Minimum element quality: 0.0131

Fig. 41 – Comparison of the mesh characteristics of unit cells A and B

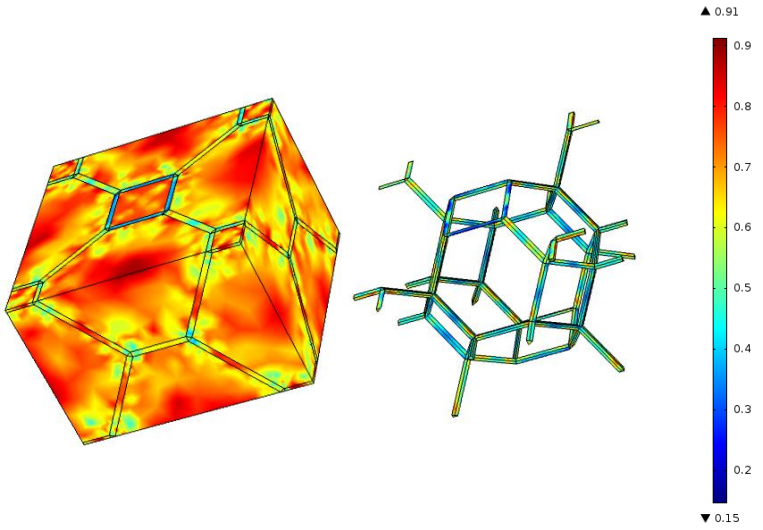

Fig. 42 – Element quality of the mesh for the unit cell B

To be able to solve large size models with high mesh density, we have opted to use a cluster computing in order to benefit from more memory than one single machine. For that, we have access to a multi-node cluster computing composed of six machines with sixteen processors each. However, this option has not been completely successful because of a large memory requirement in the meshing step. Indeed, when a problem is solved in Comsol, there are three main steps that require an intensive memory use: the meshing, the assembly and the solving. In this work, we noticed that the meshing step was requiring more memory than the solving step. In addition, we have found that the memory use of Comsol in the meshing was just limited to the memory available in one machine and thus we went out of memory for large models, before even the solving step. Because of this limitation in memory use, we were not able to perform studies on very large size models, particularly for the case of heterogeneous intergranular phase. In addition, we have analyzed the mesh sensitivity of the effective diffusivity in order to find an appropriate mesh size.

2.3.3. Mesh sensitivity

Permeation simulations have been performed on 3-D models with different mesh sizes, in order to check the convergence of the results and more particularly the effective diffusivity. The normalized effective diffusivity as a function of the overall mesh sizes is shown in Fig. 43. The total number of elements and the DOFs corresponding to each parameter size is summarized in Table III. It can be seen that the mesh size affects the effective diffusivity. However, this effect is not significant. The difference in diffusivity between the normal mesh and the extra-fine mesh is around 3%. As a result, we decided to use a normal or fine overall mesh size for the large size models.

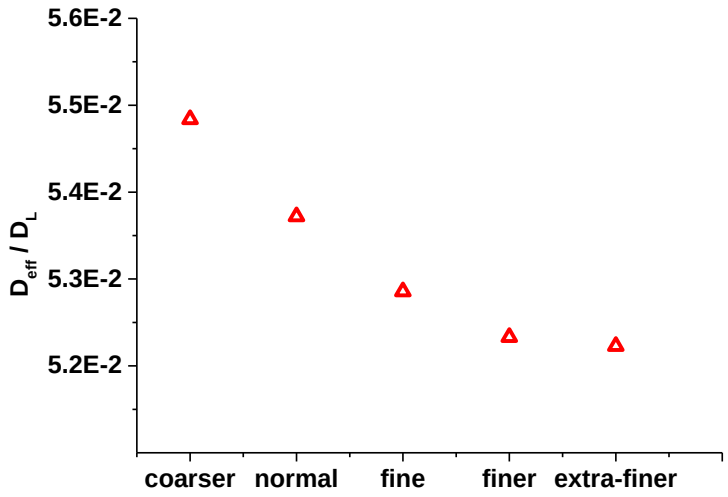

Fig. 43 – The effective diffusivity as a function of the overall mesh size

Table III – Number of elements and DOFs for the different mesh sizes. The 3-D membrane, used for the calculations, was compsed of 10×1×1 patterns B, corresponding to a thickness of e_m =1.99 µm.

	Number of elements	DOFs
coarser	16949	16221
normal	44965	31783
fine	100299	55280
finer	644388	2.40E+05
extra-fine	1684660	5.43E+05

II. Characterization of the 2-D simulated GB networks

The random distribution of diffusivities leads to the formation of different networks of RGBs and SGBs depending on the proportion f_R. Fig. 44 illustrates three networks corresponding to three different proportions of RGBs (only RGB clusters are shown). To evaluate and quantify RGBs connectivity and their spatial distribution, two methods are used in this work:

- The first method counts the paths inside every cluster and measures their lengths. Then statistical distributions of theses lengths are analyzed.
- The second method uses the mathematical theory of percolation and its tools for characterizing the population of clusters for every proportion f_R.

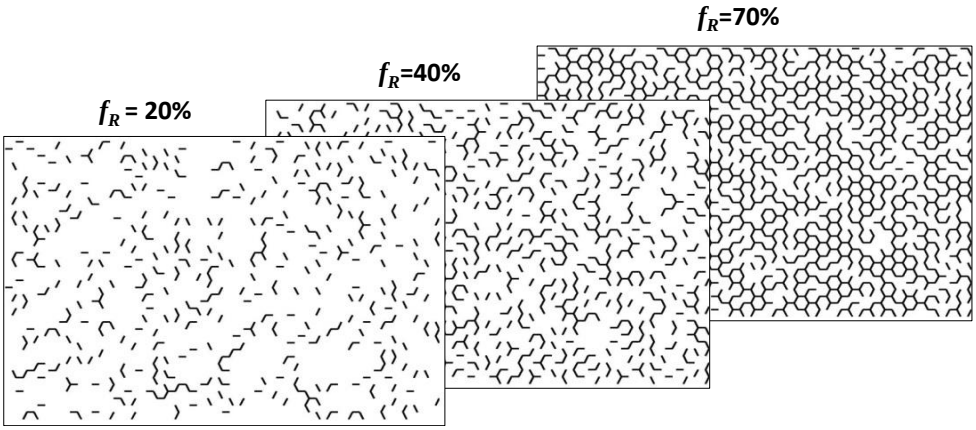

Fig. 44 - RGB networks for different RGB fractions f_R.

1. Distribution of RGBs path lengths

Each network of RGBs is composed of a number of clusters that changes with the proportion of RGBs. As illustrated in Fig. 45, each cluster consists of one or several paths with different lengths. The goal is to obtain a statistical distribution of the RGBs path lengths (L) as a function of f_R, volume fraction of RGBs.

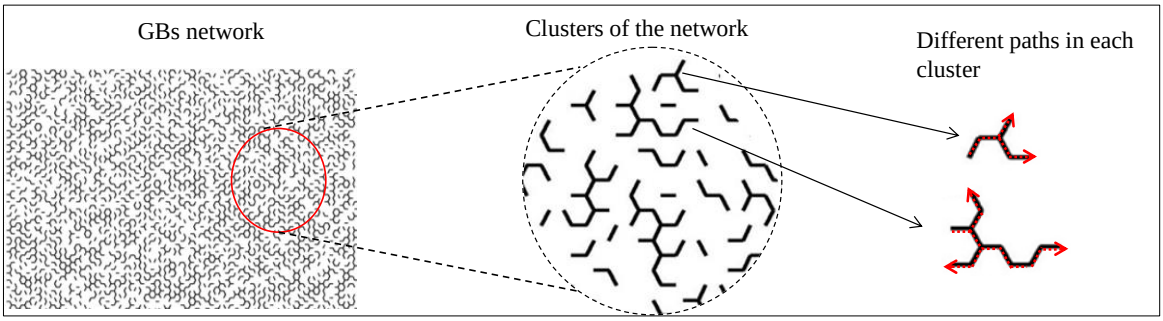

Fig. 45 - Illustration of RGBs clusters and paths.

1.1. Procedures of counting paths

To quantify the length (L) of different paths in each cluster, we set up an algorithm based on a modified random self-avoiding walk **[Slade 1994]**, implemented on Matlab. This algorithm browses the different clusters of RGBs from the left to the right and quantifies the different paths inside, as shown in Fig. 46. The unit distance is defined as one boundary length. Then, the path length is determined by the number of boundaries. Clusters are traversed from the left to the right. To eliminate the finite size effect, only interior paths, in clusters away from the edges of the simulated membrane, are considered in this analysis. The

proportion of the interior paths represent more than 85% of the total paths for f_R <0.5. The study on the path length is limited to the non-percolating networks.

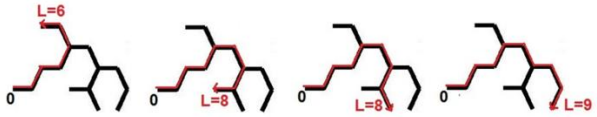

Fig. 46. Illustration of counting procedure of paths in a cluster, with the value of the path length L. The start point is always the same for each cluster, here it is noted 0.

1.2. Number of necessary realizations

As mentioned above, we adopted a random distribution of the two types of GBs on the networks. Thus, in order to achieve statistical representative of the RGBs paths length, which is a morphological property the microstructure, we may either increase the membrane size or repeat the procedure N times. However, it should be noted that the concept of the RVE depends on the considered property and there is not one single possible minimal RVE **[Kanit 2003]**. As we fix the RVE size with respect to the effective diffusivity, the only option to improve the precision of the RGB path length distributions was to repeat N times the procedure. The first approach was to increase realization number to a finite number, N, until the convergence of average length path in RGB fraction is reached. Fig. 47 presents the mean values and the intervals of confidence on the average length path of the RGBs, for different RGB fractions. This was successful but not all networks. As shown in Fig. 47, the minimal number of necessary realizations increases sharply for the fractions of RGBs greater than 0.5. In addition, when fR is larger than 0.55, the convergence is not reached even the realization number is as large as 20000. The main limitation of this approach was that we could not estimate in advance a magnitude of the number of necessary realizations and for computation cost and time, it was not possible to increase indefinitely the number of realizations.

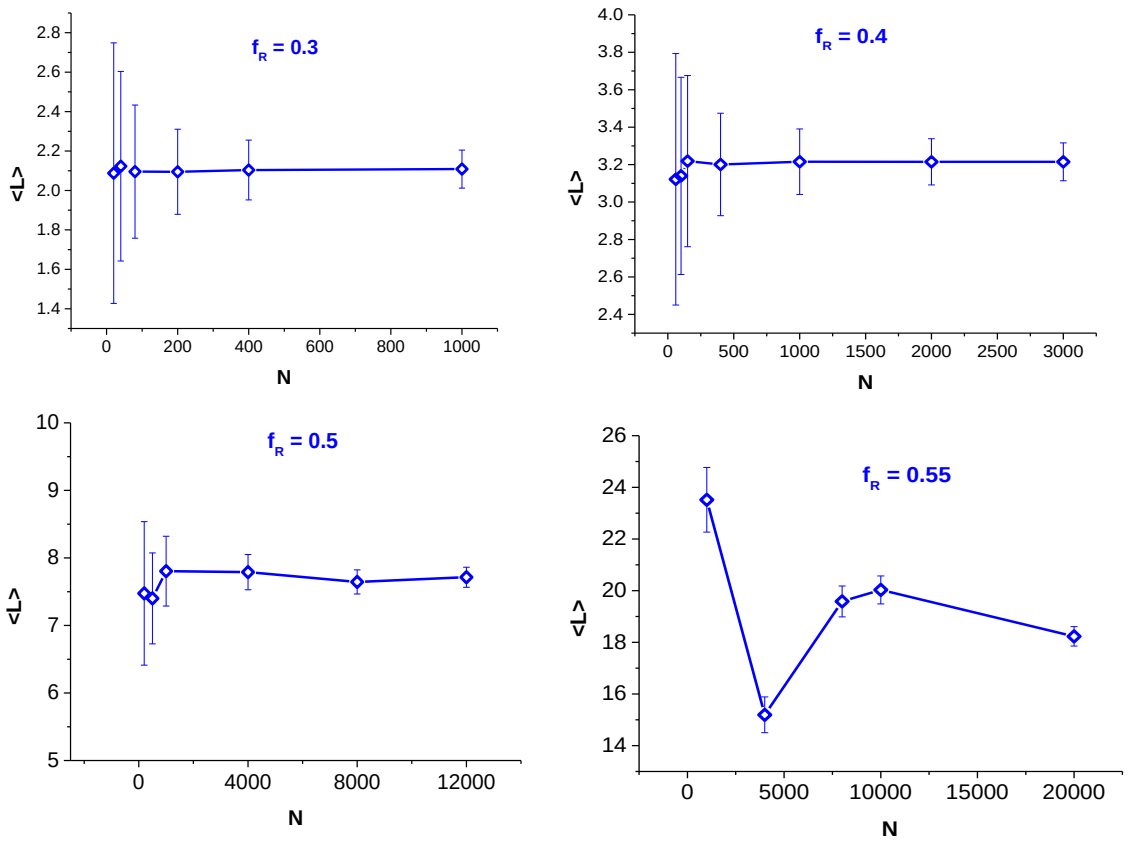

Fig. 47 - The mean values and the intervals of confidence on the average RGB path lengths, for different RGB fractions

As an alternative, we used the approach developed by Kanit *et al.***[Kanit 2003]**. Their approach allows to predict the minimal number of realizations required for a given volume size in order to estimate the effective property for a given relative precision ε_{rela}. However, this method requires to know at least an accurate estimation of the variance and the exact mean. To determine accurate values of the variance and the mean of the average path length, calculations of the RGB path length were performed on a large size membrane (10 times the size of the current RVE membrane). Then, the necessary number of realizations on the current RVE membrane with respect to RGB path length L for each RGB fraction was determined using equation (III.6) **[Kanit 2003]**:

$$N = \frac{4 * \sigma_l^2}{< L >_l^2 \ \varepsilon_{rela}^2} \qquad \text{(III.6)}$$

where σ_l^2 and $< L >_l^2$ are the variance and the average path length calculated on a large size membrane.

Fig. 48 shows the necessary number of realizations N to obtain relative precisions of 1% and 10% on the average RGB path length, as a function of the RGB fraction. It can be observed that N increases sharply for the RGB fraction above 0.4. As an example, for the RGB fraction of 0.6, N= 2×10^8 realizations are necessary to obtain a relative error of 1% on the average RGB path length.

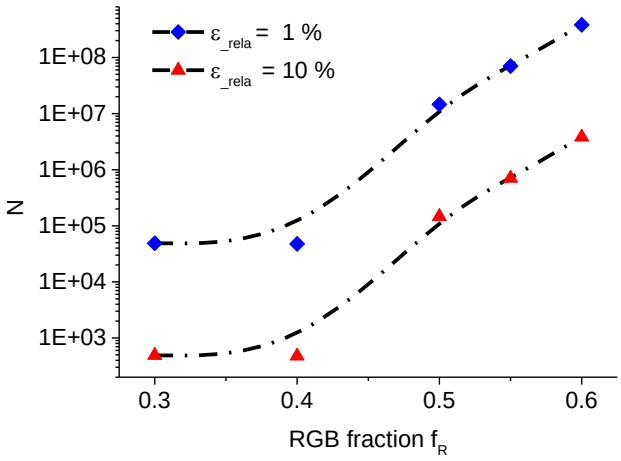

Fig. 48 : Necessary number of realizations N to obtain relative precisions of 1% and 10% on the average path length as function of the RGB path length

In the present study, it has been decided to achieve a relative error of 1% of the average path length but only for the networks with a RGB fraction below 0.5. Above this limit, a higher relative error was accepted for reasons of computing cost and convenience. To get more accurate measurements of the morphology of the GB networks within this range, the second method has been applied.

2.3. Path length distributions of RGBs

To estimate the probability distribution of the different path lengths for each fraction of RGBs, frequency histograms were constructed. To do that, a data binning process, with a chosen width of $<L>/3$, was used. $P(L, L+\Delta L)$ was defined as the probability of any RGB path length laying between L and $L+\Delta L$. Fig. 49 shows frequency distributions of path length for two RGB fractions f_R.

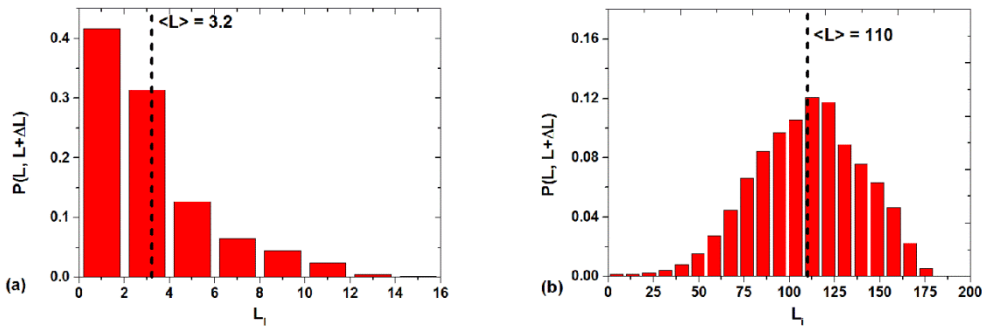

Fig. 49 - Results of the probability distributions of the path length for two different RGBs fractions, (a): f_R=0.4 and (b): f_R=0.6

The shape of the probability distributions changed with the increase of f_R. For small fractions, the heterogeneity of the path length is very wide, in contrast to high fractions where the path lengths are characterized by a homogeneous distribution. In order to compare different probability distributions, a scaling hypothesis has been applied in many cases **[Hughes 1997, Feaugas 2007]**. The same approach was used in the current work. The probability density functions, normalized by the average path length, $<L> P(L, L+\Delta L)$, are plotted as a function of $L/<L>$ in Fig. 50a.

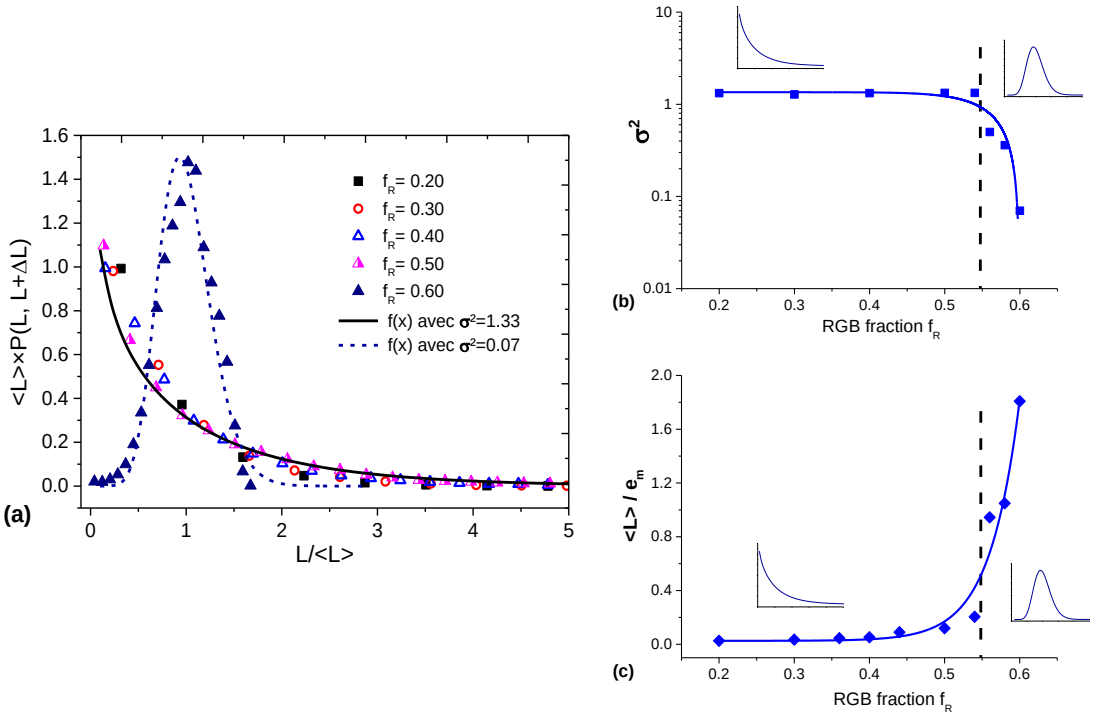

Fig. 50 – (a) The probability density functions of path lengths for different fractions of RGBs, the distributions are fitted by a gamma distribution function with parameter σ². (b) The variance of the probability density function and (c) the average path length, as a function of RGB fraction.

The resulting discrete distributions are well described by a two variate gamma distribution (equation (III.7)) **[Lienhard 1967, Feaugas 2007]**:

$$f(x) = \frac{1}{\Gamma(\alpha+1)\beta^{\alpha+1}} x^{\alpha} \exp(-x/\beta) \quad with \quad x = \frac{L}{<L>} \tag{III.7}$$

Γ is the Euler integral, α and β represent the shape and scale of the distribution respectively. In our case, the distributions were normalized, thus we can write $\beta = 1/(\alpha+1) = \sigma^2$. The gamma function's variance σ^2 *versus* the RGB fraction f_R is plotted in Fig. 50b. Depending on the values of σ^2, we could distinguish two types of networks. For the networks corresponding to a fraction f_R, below 0.5, the path length distributions are characterized by a high variance ($\sigma^2 \approx 1.3 \pm 0.1$). This large variance is probably due to the diversity in the

populations of small clusters. We call this type of network a system of paths because of the low clustering of RGBs. For the distributions corresponding to a fraction above 0.5, we observed a decrease in the variance. For this range of f_R, the clustering of RGBs was more important and we systematically observed the emergence of large clusters which contain over one hundred of RGBs. In other words, as we used a finite size system, the total number of clusters tends to decrease. Thus, the diversity and therefore the variance of the path lengths decreases when f_R is greater than 0.5. This is consistent with the results in reference **[Tsang 2000]**, where it has been shown that the cluster size diversity, in a square lattice system, decreases above a probability of 0.5. In Fig. 50c, we plotted the average path length $<L>$, normalized by the membrane size e_m, as a function of RGB fraction f_R. From $f_R = 0.5$, the average path length began to increase. Changes in the average path length $<L>$, depending on the RGBs fraction f_R, also confirm the existence of two groups of networks. Whether it's the variance or the average path length, the results clearly show the existence of two groups of RGB networks depending on the fraction of the RGBs.

2. Characterization of clusters

To study the topology of GB networks, 2-D binary images of the RGB networks are produced from the FE model, as illustrated previously in Fig. 44. Individual RGB clusters are then identified and characterized using image processing tools available in Matlab. The labeling procedure consists in assigning each pixel to a cluster if it is a neighbor to any other member pixel of the cluster. The neighboring relationship can be defined in two different ways: the 4 nearest neighbors or the 8 nearest neighbors, as shown in Fig. 51. In this work, we consider the second definition.

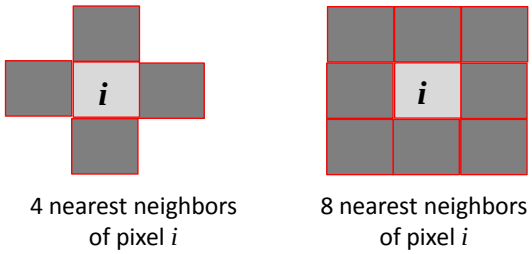

Fig. 51 - Neighboring relationship of the pixels

Standard measures from the percolation theory **[Stauffer 1994]** are then used to classify all the clusters. The first measure is the mass of the cluster *s*, which represents here the number of boundaries contained in the cluster. A cluster mass close to unity means the cluster is a single isolated boundary. The second important measure is the number of clusters of mass *s* per unit area n_s. The radius of gyration R_s, defined as the average distance between the center of mass and any boundary of the cluster, is determined using equation (III.8) :

$$R_S^2 = \frac{1}{2s^2}\sum_i^s |r_i - r_0|^2 \quad \text{(III.8)}$$

Where r_i is the vector pointing at the center of the i^{th} boundary and r_0 points the center of masse of the cluster. The radius of gyration can also be determined using the moment of inertia I_s, for an equivalent ellipse (as illustrated in Fig. 52) around an axis perpendicular to its plane and going through the intersection of the ellipse principal axis **[Hoshen 1998]**. It can be shown, using cartesian components in two dimensions, that R_s and I_s are related by equation(III.9):

$$R_s^2 = \frac{I_S^2}{s} \quad \text{(III.9)}$$

with $I_s = (s/4)(b^2 + a^2)$, where *s*, *a* and *b* are, respectively, the mass, the principal axis and the minor axis of the ellipse. We applied this formula to calculate the gyration radius R_s.

Using n_s and R_s, the squared correlation length ξ^2 is calculated with equation (III.10). This parameter gives a general view on the connectivity. It can be defined as the mean squared distance between two grain boundaries belonging to the same cluster averaged over all clusters **[Hoshen 1997]**.

$$\xi^2 = \frac{2\sum_s < R_s^2 > s^2 n_s}{\sum_s s^2 n_s} \quad \text{(III.10)}$$

The summation is over all clusters in the network. $<R_s^2>$ is the average squared radius of gyration of all clusters of mass s.

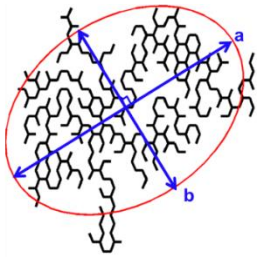

Fig. 52 - Cluster and the equivalent ellipse with a and b the principal and the minor axis

2.1. Correlation length

Fig. 53 presents the evolution of the correlation length ξ, normalized by the membrane thickness e_m, as a function of the proportion of RGB fraction f_R. Three separate domains are clearly visible: two groups of networks before percolation and a group of percolated clusters. The grain boundary network is considered

percolated when the first cluster spans the membrane. In the transition range, the correlation length ξ increases sharply. That means that the general connectivity of random boundaries is evolving quickly from a disconnected state to a high connected state. In accordance with other studies in the literature **[Clerc 1983, Stauffer 1994]**, we found that the width of the transition range depends on the size of the membrane, as discussed in the next paragraph.

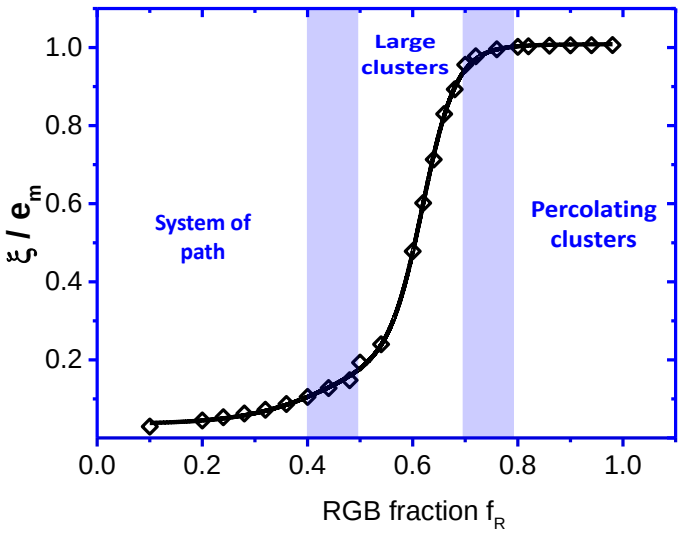

Fig. 53 - Correlation length ξ normalized by the membrane size e_m, as a function of random GB fraction f_R

2.2. Finite size effect and percolation threshold

To illustrate the finite size effect, the evolution of the normalized correlation length ξ with the fraction of RGBs is plotted in Fig. 54 for three networks of different sizes. The results are an average of 100 realizations and the correlation lengths are normalized by the membrane size. We clearly observe the size effect on the correlation length. When the membrane size is increased, the evolution of ξ tends to a typical behavior of percolation system. The relative errors due to size effect are more important around the percolation threshold which is $P_c \approx 0.655$ for our system. This value, determined by the intersection point of the three curves, is very close to theoretical one ($P_c^{th} = 1 - \sin(\frac{\pi}{18}) \approx 0.653$) calculated for an infinite system. The width of the transition zone is all the smaller as the size of the network is high. But, in order to capture the impact of GB clusters on the effective diffusivity, it was deemed appropriate not to consider very large composite membranes. Indeed, most of the experimental measurements of the effective properties are performed on finite size membranes **[Schuh 2003a, Basinger 2005, Oudriss 2012b]**.

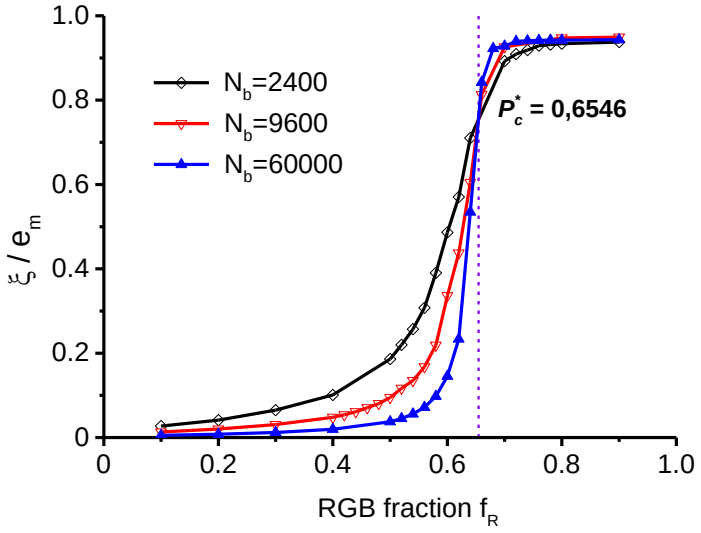

Fig. 54 – The correlation length ξ, normalized by the membrane size e_m, as a function of RGB fraction for membranes with different sizes. N_b is the total number of grain boundaries.

III. Hydrogen diffusion in 2-D polycrystalline aggregates

1. Parameters of the model

In the previous section, we did not consider the grain size effect because connectivity quantities were normalized. However, the grain boundaries contribution to the macroscopic diffusivity becomes increasingly significant as grain size is refined to the nanoscale **[Doyle 1995]**. Therefore, the topology and geometry of GB networks will have more effect on nanocrystalline materials. To investigate the effect of grain boundary networks on the macroscopic diffusivity of membranes, five heterogeneous polycrystalline composites with grain sizes λ, of 500, 200, 100, 50, and 20 nm were modeled in 2-D. The corresponding volume fractions of intergranular phase f_{GB}, are respectively 1.1%, 2.8%, 5.5%, 10.6%, 23.6%. A GB thickness of 5 nm has been used. This corresponds to an effective thickness of enhanced diffusion rate or the "segregational" zone **[Prokoshkina 2013]**. To simulate hydrogen permeation, the constant hydrogen concentration at the entry side of the membrane was set at 1 mol/m^3 and that of the exit side at 0 mol/m^3.

The following values of the diffusivity parameters have been used for FEM calculations: lattice diffusivity $D_L = 10^{-13}$ m²/s, RGBs diffusivity $D_R = 10^{-10}$ m²/s, SGBs diffusivity $D_\Sigma = 10^{-16}$ m²/s. The orders of magnitude of the lattice and RGBs diffusivities, used in this study, are those of hydrogen diffusivity in nickel, experimentally determined in **[Oudriss 2012b]**. The hydrogen diffusivity along SGBs was deduced from

these two diffusivities, using a homogenization approach. The details of the calculation can be found in appendix C. The parameters of the model are summarized in Table IV.

Table IV: List of parameters used in the model

Parameter	Description	Values
e_m	Thickness of the membrane	1.4 – 30.2 μm
h_m	Height of the membrane	0.79 – 17.4 μm
e_{gb}	Thickness of the grain boundaries	5 nm
λ	Grain size	20 – 500 nm
C_0	Entry side hydrogen concentration	1 mol/m^3
C_S	Exit side hydrogen concentration	0 mol/m^3
D_L	Diffusions coefficients in grains	10^{-13} m^2/s
D_R	Diffusion coefficient in RGBs	10^{-10} m^2/s
D_Σ	Diffusion coefficient in special SGBs	10^{-16} m^2/s

2. Effective diffusivity

The effective diffusion coefficient D_{eff}, normalized by the lattice diffusion D_L, is plotted in Fig. 55 as function of the fraction of RGBs f_R, for different volume fractions of intergranular phase f_{GB}. With an increase in f_R, D_{eff}/D_L increases nonlinearly. We can distinguish a curve inversion for all f_{GB}. When $f_R < 0.5$, D_{eff} is lower than D_L, which means that the special boundaries impede the hydrogen diffusion. When $f_R > 0.5$, D_{eff} is higher than D_L, which means that random boundaries act as fast diffusivity paths. This threshold value corresponds to percolation threshold of the effective diffusivity in the homogenized system and depends on the ratio between diffusivities of the different components. The meaning of this threshold is discussed in the next section (IV.2).

The effect of RGB proportion f_R, becomes more considerable as the GB volume fraction f_{GB}, is increased. To better capture this effect, numerical differentiation of D_{eff} relative to f_R, has been performed. Results of the numerical differentiation were fitted by a logistic function **[Seber 2005]**, described by equation (III.11):

$$y(f_R) = \frac{A}{1+e^{-k(f_R - f_i)}} \tag{III.11}$$

where $k > 0$ and $0 < y < A$. This equation is purely empirical and generally used to describe the growth of a quantity in different situations (population study, chemical reactions…) **[Seber 2005]**. Fig. 56a illustrates the fitted curves. The amplitude A defines the maximum value reached by $y(f_R)$. A high value of the amplitude A means there is a large gap between the values of the derivative of D_{eff} for low fractions f_R, and those for high fractions f_R.

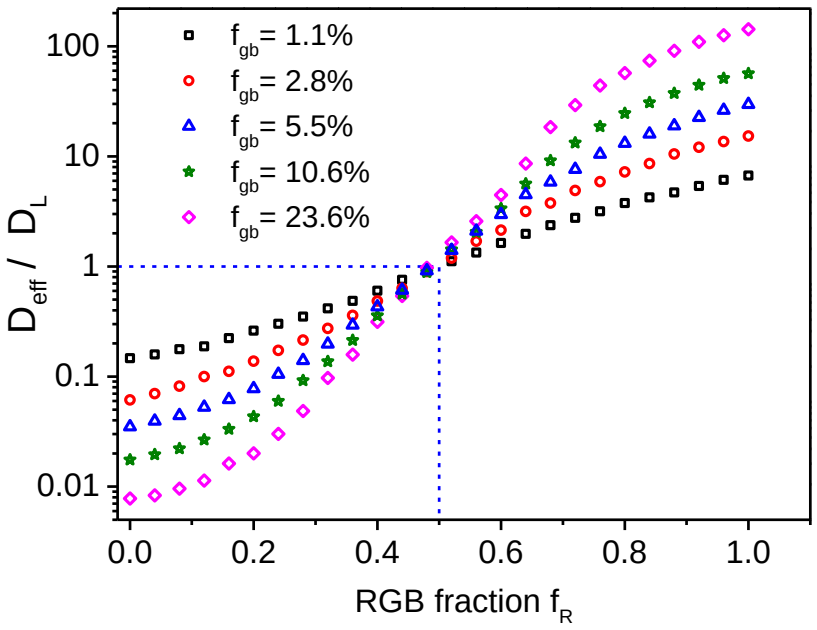

Fig. 55 - Effective diffusivity D_{eff}, normalized by the lattice diffusion D_L, as a function of RGB fraction, f_R, for different intergranular fractions f_{GB}.

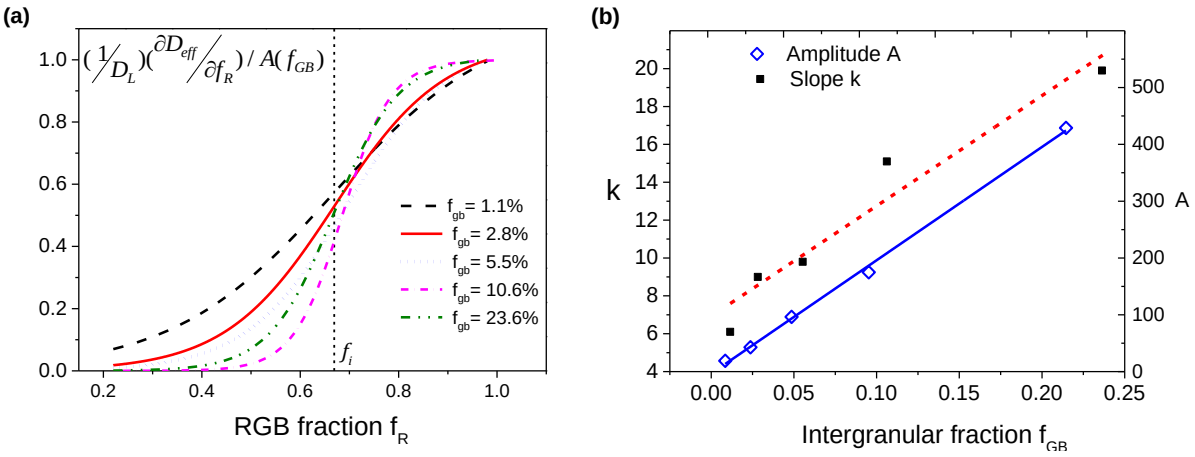

Fig. 56 – (a) The fitting curves of the 1st derivative of D_{eff} relative to f_R for different intergranular fractions. (b) The slope of the transition range of the fitting curves (in dashed line) and the amplitude of the fitted curves (in sold line) as a function of the intergranular fraction.

Fig. 56b shows the evolution of the amplitude A as a function of the intergranular fraction f_{GB}. We observe that the amplitude increases linearly with f_{GB}. It is important to notice that there is a difference of 2 orders of magnitude between the highest and the lowest amplitude, respectively corresponding to a grain size of 500 nm and 20 nm. This illustrates the higher impact of grain boundary characters distribution on the effective diffusivity in nanoscaled membranes, compared to fine grained membranes.

We note also that the shape of the 1st derivative of D_{eff} is very sensitive to the grain size, as shown in Fig. 56a. Two parameters (k and f_i) describe the form of a logistic function. The parameter k describes the slope of the logistic function when it passes by the inflection point f_i. In concrete terms, k acts as a scale parameter on f_R, thus controlling the slope of the 1st derivative of D_{eff}. We plotted in Fig. 56b the parameter k *versus* the intergranular fraction f_{GB}. It is seen that k increases linearly with f_{GB}. This means that the rate of increase of D_{eff} in the transition zone, is linearly correlated to the intergranular fraction. However, the increase in D_{eff} is actually related to the formation of large RGB clusters. Therefore, it can be concluded that the impact of GB networks structure on the effective diffusivity is linearly dependent on the intergranular fraction. This suggests that the percolation behavior of the effective diffusivity would be progressively marked as the intergranular fraction increases. Hence, it is important to take into account the GB connectivity in the evaluation of the effective diffusivity in nanocrystalline materials.

The other important parameter in a logistic model is the inflection point f_i. This point corresponds to the fraction at which the slope is at its maximum. Here the inflection point f_i is almost the same for all the membranes ($f_i \approx 0.64 \pm 0.04$). This fraction is close to the geometrical percolation threshold of 2-D RGB networks ($P_c^* \approx 0.65$) **[Stauffer 1994]**. This last point confirms that the rate of increase of D_{eff} is correlated to the RGB network parameters.

3. Correlation between effective diffusivity and connectivity parameters

The effective diffusion coefficient D_{eff}, normalized by the lattice diffusion D_L, is plotted Fig. 57 as function of the correlation length ξ of RGB networks, for different volume fraction of GB phase f_{GB}. D_{eff} increases nonlinearly with the correlation length ξ. The trend of D_{eff} follows a three step behavior corresponding to the 3 groups of networks previously defined with the connectivity parameters (system of paths, large clusters and percolated clusters). First, one must remember that the system of paths corresponds to the range f_R below 0.4. In terms of number of grain boundaries, clusters contain a maximum of fifteen GBs. The average path length of RGB is less than 4 GBs. That means that the RGB network is composed of a lot of isolated RGB. They contribute to break the percolated special GB cluster and thus reduce its blockage effect. In order to analyze the correlation between the effective diffusivity and the RGB clusters we zoomed on this range and we considered suitable to use the path length instead of the correlation length.

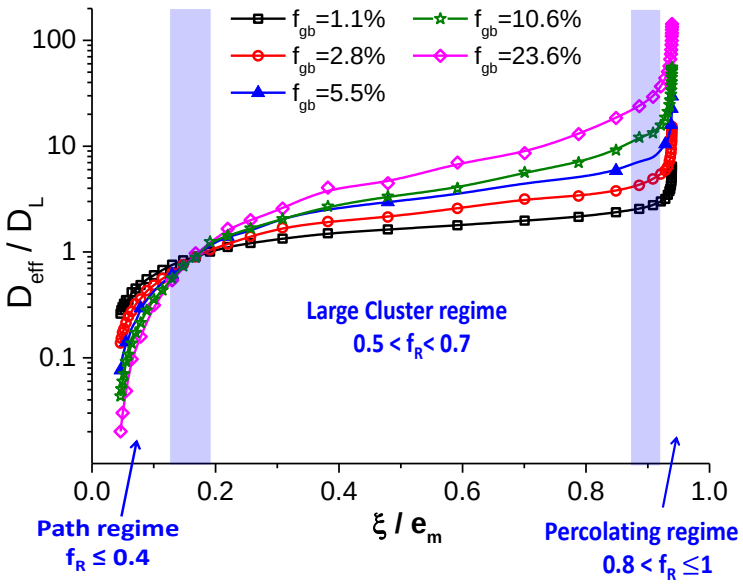

Fig. 57 - Effective diffusion coefficient D_{eff} normalized by the lattice diffusion D_L as function of the correlation length ξ normalized by the membrane size e_m.

Fig. 58a shows the effective diffusivity D_{eff} as a function of the RGB path length. D_{eff} increases linearly with the average path length of RGBs. However the slope of D_{eff} is the same for the different intergranular fractions. This may be linked to the low connectivity of RGBs in this range. The linear relationship between D_{eff} and the average path length <L> was fitted with equation (III.12):

$$\frac{D_{eff}}{D_L} = \alpha_1 + \beta_1 \frac{< L >}{e_m} \qquad if \qquad < L > \; > \; L_c \approx 1.5\lambda \tag{III.12}$$

α_1 and β_1 are the intercept and slope of the fitting curve, respectively. A new parameter α_c, is defined as $\alpha_c = D_{eff} / D_L(L_c)$.[1] To better capture the impact of the connectivity parameter on the effective diffusivity, we analyzed the evolution of the parameters α_c and β_1 for different intergranular fractions in the path regime. In the framework of a homogenized system, the effective properties are carried by the term which depends on the intergranular fraction f_{GB}, i. e., α_c here. The evolution of the absolute value of α_c *versus* the intergranular fraction f_{GB} is plotted in Fig. 59a.

[1] *The domain of definition of this regime depends on the definition of diffusion path. The minimum diffusion length must exceed a grain size, in order to cross a junction (a triple junction) and keep a symmetry relationship. L_c satisfies these two conditions.*

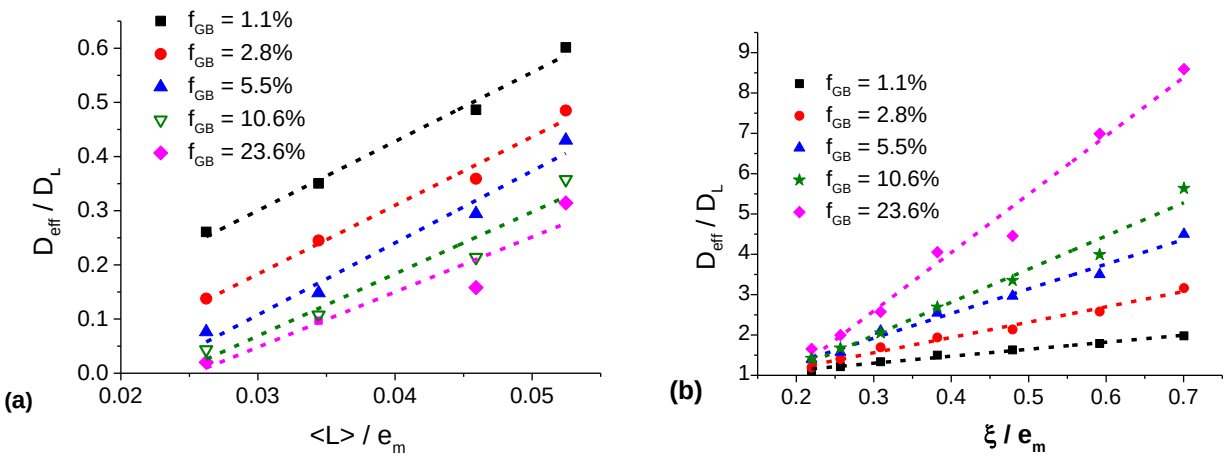

Fig. 58 - Effective diffusion coefficient D_{eff} normalized by the lattice diffusion D_L (a) as function of the average path <L> normalized by the membrane size e_m for the path length regime (f_R<0.4) and (b) as function of the correlation length ξ normalized by the membrane size e_m for the clusters regime.

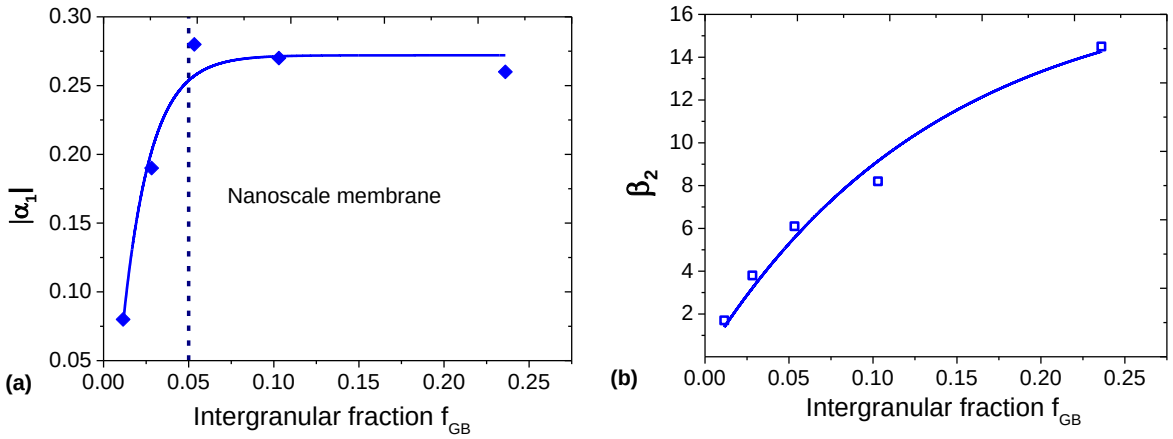

Fig. 59 - (a) Evolution of the intercept α_c in equation (III.12) and (b) the slope β_2 in equation (III.13) as a function the intergranular fraction f_{GB}.

Initially, α_c decreases with f_{GB} and then tends to a steady state for the fractions above 5%. According to the evolution of α_c, two cases are distinguished. For f_{GB} < 5.5 % (which corresponds to fine grained membranes), the intergranular fraction influence the properties of the homogenized system. This result confirms the idea that RGB act like small isolated inclusions, in this interval of RGB fractions. For f_{GB} higher than 5.5 % (which corresponds to nanoscaled membranes), as α_c tends to a constant value, D_{eff} increases because only <L> is increasing. That means the average path length <L> is the most relevant parameter to describe the effective diffusivity. We believe that the second term β_1, which is characteristic of the connectivity effect on the slope of D_{eff}, is less sensitive to f_{GB}. We think that the little gap between the points for f_{GB}=10.6% and f_{GB}=23.6% (that should be coincident) in Fig. 58(b) is due to the statistical variation of the data. Thus, the effect of the

GB path length can be considered independent of the GB volume fraction in this interval. In other words, information on the RGB connectivity would not be necessary for the prediction of the effective diffusivity, in the framework of homogenization.

We performed the same analysis in the second range ($0.5< f_R <0.7$) defined in Fig. 53, the clusters regime, but this time we kept the correlation length to characterize the grain boundary structure. In Fig. 54b, the normalized effective diffusivity is plotted as function of the correlation length ξ, normalized by the membrane thickness. We noted the linear increase of D_{eff} when the correlation length ξ increases but unlike the first regime, the slope of D_{eff} increases with the intergranular fraction. This may be explained by the emergence of larges clusters which occupy more volume fraction. The evolution of D_{eff} was fitted by linear curves, described by the equation (III.13) for the different GB volume fraction.

$$\frac{D_{eff}}{D_L} = \alpha_2 + \beta_2(f_{GB})\frac{\xi}{e_m} \tag{III.13}$$

In this range, the slope of the linear curves β_2, increases with the intergranular fraction f_{GB} (Fig. 59b). The intergranular fraction f_{GB} directly impact the sensitivity of the effective diffusivity to the GB clusters sizes. In term of homogenization, this suggests that it is important to consider the GB clusters properties and no longer the properties of isolated boundaries, in order to have a better description of the effective diffusivity. The intercept α_2 has no physical meaning, as it is out the domain. The membrane can be seen, macroscopically, as a ternary composite with large clusters of two types (random or special) in a phase of grains. This result shows that information on GB networks connectivity is essential for establishing homogenization models describing the effective diffusivity of the macroscopic membrane. This is consistent with the conclusions of Chen and Schuh **[Chen 2006]** which showed the necessity of combining percolation theory and effective medium theory in order to best describe the effective diffusivity of a randomly-distributed hexagonal network. Furthermore, our results show that the inclusion of the GB networks in a phase of grains does not alter this conclusion.

The last regime, with f_R above 0.8, in Fig. 57, corresponds to the percolating regime. Here, the correlation length ξ no longer changes because of the percolating cluster, but D_{eff} increases sharply. The colored bands between the regimes represent the transition intervals.

In summary, from the GB network characterization, we have seen that there are different types of GB networks with different topologies and connectivity depending on the fraction of random boundaries. The results on evolution of the effective evidence clear correlations between the different types of network and the different regimes of the diffusion:

- In the “path length” regime of diffusion, the RGB connectivity is very low and does not affect the effective diffusivity

- In the "large clusters" regime of diffusion, the increase the effective diffusivity is strongly on the RGB connectivity
- In the "percolated regime", the changes in the RGB network have not significant effect on the effective diffusivity.

This classification allows to determine in which interval of RGB fractions, the effective diffusivity is the more affected by the GB network topology. These three different behaviors of D_{eff} as a function of the connectivity parameters were obtained for specific parameters, particularly for given ratios D_L/D_Σ and D_R/D_L, of different diffusivities. Our interpretations apply only when there is a high contrast between the diffusivities of different boundaries types and $D_L/D_\Sigma = D_R/D_L$. In the next section, we propose to study the effects of the GB connectivity on the effective diffusivity in more generalized framework, by using homogenization technics.

IV. Effective medium approximation: implications of the GB connectivity

1. Generalized effective medium theory

In the second chapter, we highlighted the weakness of the classical homogenization technics such as the EMT to predict effective properties in heterogeneous system with percolation transition. More precisely, the EMT overestimates the percolation threshold and is unable to predict the correct power-law behavior of effective properties near the percolation threshold **[Sahimi 2003]**. To compensate this lack, McLachlan and co-workers proposed a modified EMT, in the framework of electrical conductivity in inhomogeneous media **[McLachlan 1986]**. The idea of McLachlan was to combine the EMT and the percolation theory by introducing the percolation threshold P_c and critical exponents *s* and *t* into the EMT formula. In analogy, consider a composite with two components of low and high diffusivity, with volume fractions *(1-p)* and *p*, respectively. McLachlan's modified EMT, referred to as the generalized effective-medium (GEM) approximation, is given by **[McLachlan 1986, Chen 2006]**:

$$(1-p)\frac{D_1^{1/s}-D_{eff}^{1/s}}{D_1^{1/s}+(P_c^{-1}-1)D_{eff}^{1/s}}+p\frac{D_2^{1/t}-D_{eff}^{1/t}}{D_2^{1/t}+(P_c^{-1}-1)D_{eff}^{1/t}}=0 \qquad \text{(III.14)}$$

where *s* and *t* are scaling exponents and P_c is the percolation threshold of the high diffusivity component. A general form of the GEM equation for multicomponent networks has been developed by Chen and Schuh **[Chen 2006]**:

$$\sum_{k=1}^{n} \frac{p_k}{1-p_k} \left[\sum_{i=1}^{k-1} \left(p_i \frac{D_k^{1/s} - D_{eff}^{1/s}}{D_k^{1/s} + A_{ki} D_{eff}^{1/s}} \right) + \sum_{j=k+1}^{n} \left(p_j \frac{D_k^{1/t} - D_{eff}^{1/t}}{D_k^{1/t} + A_{kj} D_{eff}^{1/t}} \right) \right] = 0 \quad \text{(III.15)}$$

$A_{ki} = \left(P_c^{k-i}\right)^{-1} - 1 = A_{ik}$ is the percolation threshold for k-i binary system and *s* and *t* are the scaling exponents for simple binary systems. According to the authors, they are independent of the number of phases.

The GEM equation provides accurate predictions for discrete networks with percolating behavior **[McLachlan 1986, Chen 2006]**. However, its application is more complex for the real materials which correspond more to a continuum composite where the different phases together fill completely the media. Due to the multi-connectivity and the geometric shape variety, continuum composites exhibit more than one percolation threshold and variable critical exponents **[Balberg 1998, Chen 2009]**. This is problematic since the GEM equation requires single values for each scaling exponent. Recently, the validity of the conventional approach which consists of mapping the phase connectivity to a discrete network to study continuum percolation was questioned by Chen and Schuh **[Chen 2009]**. The authors pointed out that this technic leads to an artificial secondary percolations thresholds and causes shift in the critical exponents of the effective properties.

In our case, the use of the GEM on the continuous ternary system would require to vary the interganular fraction on the entire range (0 to 100%) in order to find the different percolation thresholds. This is not useful in the case of polycrystalline materials since the interganular fraction rarely exceed 30% (nanocrystalline case) of the volume fraction. As an alternative, we propose a double transition-scale approach to approximate the effective diffusivity obtained with the FEM simulations.

2. Effective diffusivity of the continuum composite model

As mentioned previously, the studied membrane can be regarded as a multi-phase composite, composed by two types of GBs and grains with different diffusion properties and volume fraction. Fig. 60 illustrates the equivalent composite.

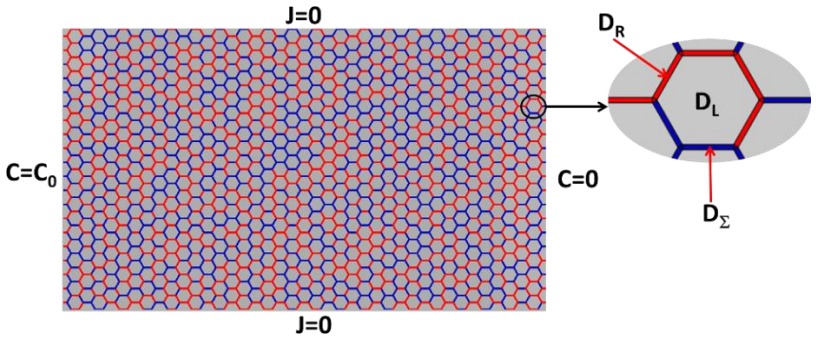

Fig. 60 – The ternary composite model, with the different diffusion coefficients

In order to find a model predicting the effective diffusivity, a deductive approach which combines the GEM approach and the Hashin-Shtrikman formula is proposed. We first calculate the effective diffusivity of GB network using GEM equation (III.14). The latter is solved using an iterative algorithm implemented on Matlab. Then, the obtained GB effective diffusivity D_{eff_GB} is incorporated in the upper Hashin-Shtrikman equation (III.16) in order to determine the macroscopic diffusivity D_{eff}.

$$D_{eff} = D_{eff\_gb} + \frac{1 - f_{GB}}{\frac{1}{D_L - D_{eff\_gb}} + \frac{f_{GB}}{2D_{eff\_gb}}} \qquad \text{(III.16)}$$

where f_{GB} is the interganular volume fraction. The main idea is to vary the parameters *s*, *t* and P_c in the GEM equation (III.14) until the calculated macroscopic diffusivity D_{eff} corresponds to the results from the FEM simulations. It should be noted that the percolation threshold is also an adjustable parameter.

The best fit of the homogenization model predictions and the simulation data is presented in Fig. 61. The quality of the fitting varies with the intergranular volume fraction. To better capture the effectiveness of the fitting, we plotted the coefficient of determination R^2, as function of intergranular fraction f_{GB}. Predictions from GEM+HS are in good agreement with the simulation data for the membrane with high intergranular volume fraction, i. e. $f_{gb} \geq 10\%$. This corresponds to nanocrystalline membranes with a grain size equal or less than of 100 nm.

The best fit yields to scaling exponents $t = 1.8 \pm 0.15$ and $s = 3 \pm 0.2$ and a percolation threshold $f_R^c = 0.52 \pm 0.02$. By definition, the scaling exponents characterize the divergence of the effective diffusivity around the percolation threshold. These parameters are different from the morphological exponents and no direct relation was found to exist between them **[Sahimi 2003]**. It is important to note that, in percolation theory, the scaling exponents of effective properties are normally symmetric ($s \approx t$), which is not the case here. This is explained by the fact that we considered a continuum percolation of the hydrogen transport. In other words, the fact that the hydrogen diffusion is not limited to the GB networks and can occur also in the

intra-granular phase changes the percolation behavior of the effective diffusivity. As shown in Table V, we compared the scaling exponents in our study with those obtained for diffusion in GB networks alone **[Chen 2006]**. It can be seen that the continuum values of *s* and *t* are higher than in the discrete model. The increase in *s* and *t* may be caused by the more diffusion paths offered by the intra-granular diffusion. Another explanation of this would be the effects of corners contact, as shown by Chen and Schuh **[Chen 2009]** for the percolation in a continuum 2-D square composite.

Table V : Scaling exponents of the effective diffusivity

	s	t
Discrete system **[Chen 2006]**	1.05 ± 0.07	1.15 ± 0.1
Continuum system	3 ± 0.2	1.8 ± 0.15

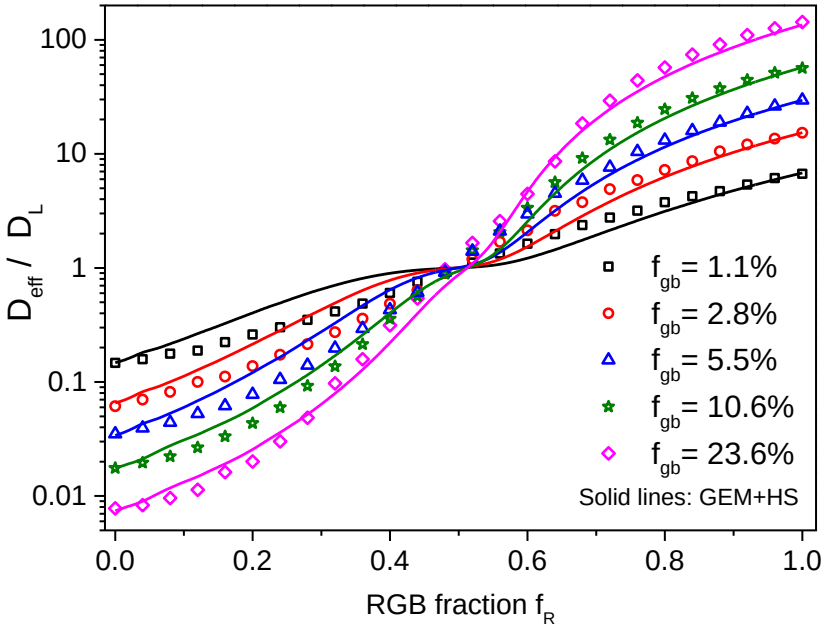

Fig. 61 – The macroscopic effective diffusivity D_{eff} normalized by the lattice diffusivity D_L as a function of the RGB fraction for different intergranular fractions. Solid lines represent the predictions of the GEM+HS with f_R^c = 0.52, *t* = 1.8, and *s*=3.

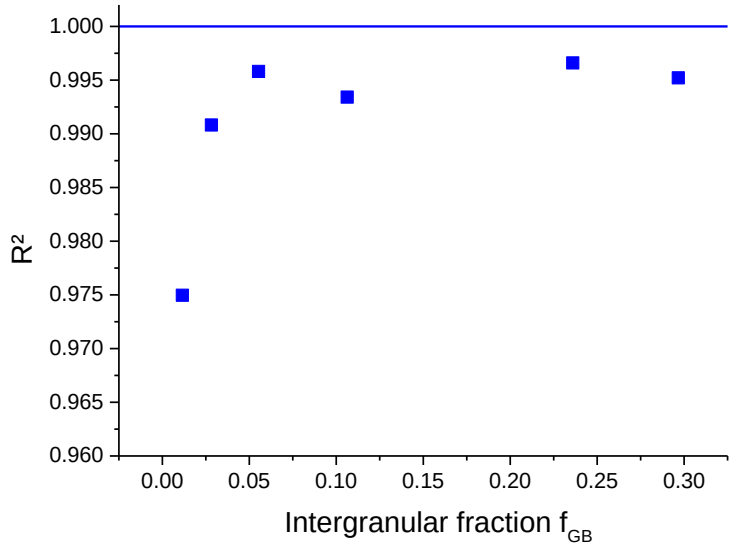

Fig. 62 : The coefficient of determination R^2 as function of intergranular fraction f_{GB}

The percolation threshold of GB effective diffusivity obtained from the fitting is the same that the intersection point of the curves with different intergranular fractions. It has been revealed that transport in ternary continuum composite exhibit two percolation thresholds **[Chen 2009]**. We believe that this percolation threshold corresponds to one of the two percolation thresholds of the effective diffusivity in the ternary continuum system. In terms of continuum phase fraction, the obtained percolation threshold from the fitting is $P_c = f_{GB} \times f_R^c$. Thus, it can be deduced that the percolation threshold of the effective diffusivity in the different membranes is almost the half ($f_R^c \approx 0.52$) of the intergranular fraction. This value can be explained by the symmetry of the system in term of GB diffusivities relative to the lattice diffusivity value. In other terms $D_R/D_L = D_L/D_\Sigma$ in our case. Therefore, we observe that the percolation threshold for diffusion in continuum system depends on the ratio between the different diffusivities. To illustrate this point, the evolution of the diffusivity D_{eff}, normalized by the lattice diffusion D_L as a function of the RGBs fraction is depicted in Fig. 63, for two different ratio between GB diffusivities and lattice diffusivity. The percolation threshold obtained from the fitting is $f_R^c \approx 0.39$ in the case where $D_R/D_L = 100 \times (D_L/D_\Sigma)$, as shown in Fig. 63. While in the case where $D_R/D_L = 10^{-6} \times (D_L/D_\Sigma)$, we observe a percolation threshold of round $f_R^c \approx 0.6$ (Fig. 63) .

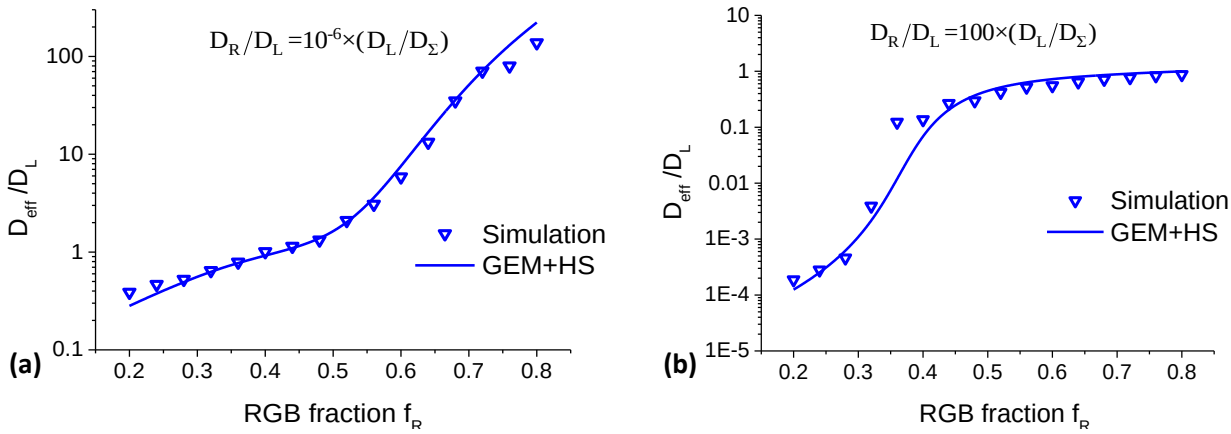

Fig. 63 - Macroscopic effective diffusivity D_{eff} normalized by the lattice diffusivity D_L as a function of the RGB fraction for different contrast of diffusivities $D_R/D_L = \alpha(D_L/D_\Sigma)$ with $\alpha = 10^{-6}$ (a) and $\alpha = 100$. Solid lines represent the predictions of the homogenization model.

In summary, we notice that the application of the existent homogenization tools on continuum heterogeneous materials with percolating behavior is complex. The proposed model can be used as a transition scale method and can give a more accurate estimation of the GB network contribution to the macroscopic diffusivity, particularly for nanocrystalline materials. However, more analysis is necessary to see if it can be extended to a multicomponent continuum composite.

V. Hydrogen diffusion in 3-D simulated polycrystalline aggregates

We have shown in the previous part of this chapter that the connectivity of grain boundaries is a key parameter for the good prediction of the effective diffusivity when one is considering grain boundaries with different diffusivities. This result was obtained with a two dimensional model. To go farther, we need to question the effect of the space dimension on the effective diffusivity behavior.

But, before investigating the grain-boundary connectivity effects in three dimensional systems, we have focused on the effects of the membrane geometric size. According to Legrand *et al.****[Legrand 2013b]***, one need to consider a membrane with a thickness higher than a critical value in order to avoid scale effects one the effective diffusivity, as illustrated in Fig. 64. In addition, this critical thickness is found to be dependent on the intergranular volume fraction. However, these findings were obtained from calculations on two-dimensional FEM model. The idea is to confirm this result in three dimensions.

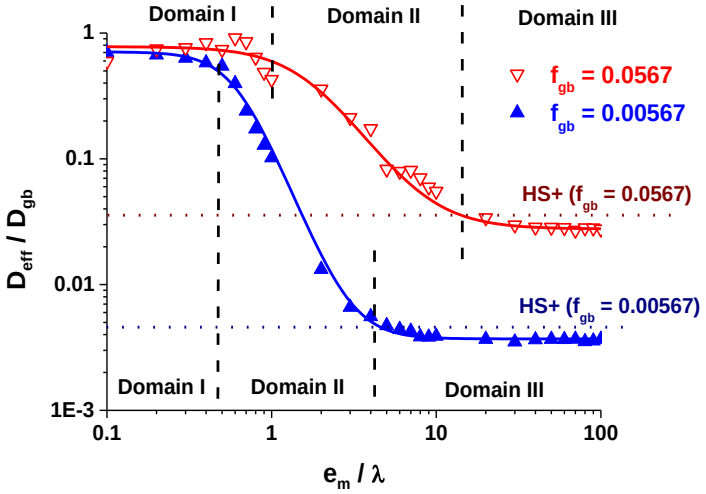

Fig. 64 - Evolution of the effective diffusion coefficient D_{eff} as a function of the ratio between the membrane thickness e_m and the grain size λ for two grain boundary volume fractions **[Legrand 2013b]**.

1. Geometric considerations

2.1. Scale effects due to the membrane thickness

As described in the second chapter, the principles of experimental permeation tests consists in measuring the hydrogen flux through a membrane subjected on one of its faces to a hydrogen pressure (or concentration). Since the duration of the experience is several days for cfc polycrystalline materials, such as nickel, one of the way to reduce the experience time is to use very thin membrane **[Frappart 2011a, Oudriss 2012a]**. However, dimensional characteristics of the metallic membrane can alter the data extracted from this technic such as the diffusivity. The impact of the membrane thickness on permeation transient has been reported in a number of experimental works **[Crolet , Crolet , Bonis , Kittel 2008, Frappart 2011a]**. According to Crolet *et al*.**[Crolet 2001a]**, there are two different permeation behaviors for thin and thick membranes. However, there is not a unique transition thickness between thin and thick membranes because the critical thickness depends on environmental parameters such as the pH but also on the materials characteristic **[Kittel 2008]**. Recently, Legrand et al. **[Legrand 2013b]** have studied the effects of grain boundaries, considered as fast diffusivity paths, on the permeation data, by using FEM calculations in two dimensions. They have shown the scale effects of the membrane size on the permeation data and more particularly the dependence of the critical thickness on grain boundaries volume fraction.

In this section, we consider the same approach than in **[Legrand 2013b]** but in three dimensions. As described above, the simulated microstructure is composed of grains surrounded by intergranular phase. In order to focus only on the effects of the membrane thickness, the intergranular phase is assumed to be mainly constituted of percolated RGBs, with higher diffusivity than lattice diffusivity. The values of diffusivities used

in these calculations are taken from the experimental results in **[Oudriss 2012b]**, performed on polycrystalline Ni. All the parameters of the model are summarized in Table VI.

Table VI - List of parameters used in the model

Parameter	Description	Value(s)
e_m	Thickness of the membrane	9.5×10^{-2} µm< e_m <6.8 µm
d_m	Depth of the membrane	0.2 µm
h_m	Height of the membrane	0.2 µm
e_{gb}	Grain boundary thickness	5 nm
λ	Grain size	50 nm
C_0	Initial entry side concentration	1 mol/m^3
Cs	Exit side concentration	0 mol/m^3
D_L	Grains diffusion coefficient	10^{-13} m^2/s
D_{gb}	Grain boundaries diffusion coefficient	10^{-10} m^2/s

The effective diffusivity D_{eff}, normalized by the GB diffusivity D_{gb}, is plotted in Fig. 65 as function of the ratio between the membrane thickness e_m and the grain size λ. We can separate clearly in three domains the evolution of D_{eff}. The first domain corresponds to the case where the membrane is thinner than the average grain size, so D_{eff} is close to D_{gb}. Then, in the second domain, D_{eff} is decreasing with increasing the membrane thickness, until reaching the third domain, where it is constant. In this latter domain, the membrane thickness effects on the permeation data become negligible, confirming the results in **[Legrand 2013b]** obtained for two-dimensional simulated membranes. In addition, in third domain, the effective diffusivity can be approximated by the Hashin-Shtrikman superior bound (equation (III.17)). This is also consistent with previous works **[Chen 2007, Legrand 2013b]**.

$$D_{eff}^{HS+} = D_{gb} + \frac{1 - f_{GB}}{\frac{1}{D_L - D_{gb}} + \frac{f_{GB}}{3D_{gb}}} \qquad \text{(III.17)}$$

According to the result in Fig. 65, a critical ratio $e_m/\lambda \approx 40$ was estimated for the simulated polycrystalline membrane. Specifically, this means that for a nanocrystalline material containing 10% of intergranular fraction, the effective diffusivity is a material property if only the membrane is at least 40 times the grain size. It is important to notice that this critical thickness is dependent on the intergranular volume fraction, as shown by Legrand *et al*. **[Legrand 2013b]** for 2-D simulated microstructures. Their result is depicted in Fig. 66. It can be seen that the critical thickness increases with the intergranular fraction. The required critical membrane thickness is larger for nanocrystalline materials. If we compare the estimated critical thickness from our study in 3D and the prediction of the critical thickness estimated for the 2-D microstructures (Fig. 66) for an equivalent intergranular fraction, we observe that the 3D critical thickness is higher than in the 2D case. This could be explained by the greater impact of the intergranular diffusivity in 3D. However, it would be

interesting to also determine the evolution of the critical thickness as a function of the intergranular fraction. That was not possible in the framework of this work due to the computation limitations.

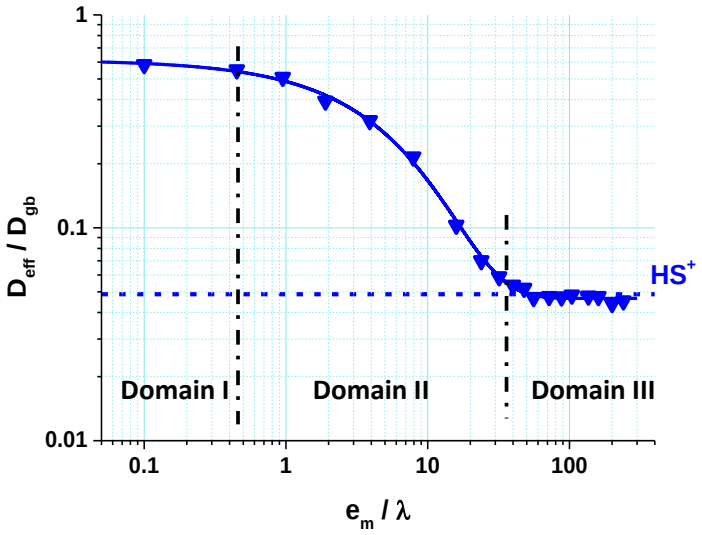

Fig. 65 – The normalized effective diffusivity as a function of the ratio between the membrane thickness e_m and the grain size λ.

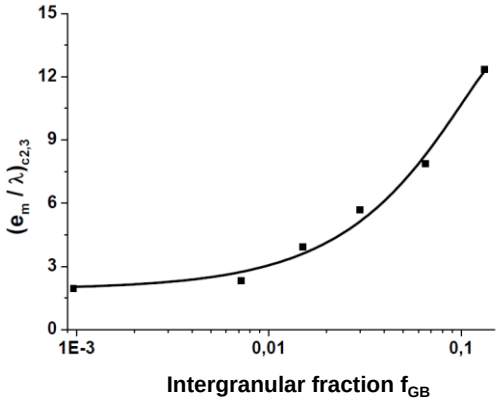

Fig. 66 – Evolution of the crtical ratio e_m / λ as a function of the intergranular fraction in two dimensions **[Legrand 2013b]**.

2.2. Effect of the membrane height and width on the effective diffusivity

According to the previous results, a membrane thickness e_m (Fig. 67) that is 40 times the grain size could be sufficient to get rid of the effects of the membrane thickness. The width d_m and the height h_m of the membrane have no effects on the effective diffusivity because the symmetric boundary conditions and the fact that diffusion flow is normal to their direction (Fig. 67a). However, in the case of heterogeneous intergranular

phase, the sizes in the y and z directions can induce finite size effects on the GB network. This can result in fluctuations of the effective diffusivity. To check the magnitude of these fluctuations, we varied the width d_m of the membrane for fixed thickness and height and we computed H-permeation tests. The evolution of the effective diffusivity D_{eff} as a function of the RGB fraction f_R, for different membrane width, is reported in Fig. 67b. It can be seen that the fluctuations of D_{eff} are limited to the transition zone of the GB connectivity. In addition, the magnitude of the fluctuations is not very important. As we were not able to compute very large 3-D models, the adopted solution was to repeat calculation in the transition zone a number of times in order to reach a sufficient relative precision on the average effective diffusivity.

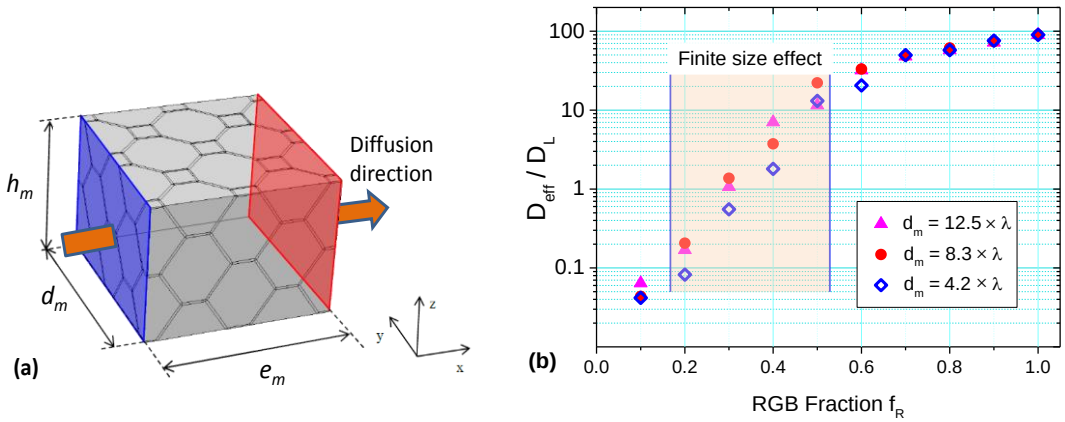

Fig. 67 – (a) Geometric parameters of the 3-D simulated membrane; (b) The normalized effective diffusivity as a function of the fraction of RGBs for membrane width. λ is the grain size and the considered membrane thickness and height are e_m =40×λ and h_m = 3×λ, respectively.

3. Implications of the space dimensionality

Most of the analytical and experimental studies dealing with the grain boundary connectivity and their implications for material properties have focused on two dimensional cases **[Wells 1989, Frary 2005b, Tsurekawa 2006, Rohrer 2010]**. However, few realistic polycrystalline materials are in two dimensions, except thin films. In addition, the dimensionality of the system has been shown to affect the connectivity and the percolation behavior of GB networks **[Frary 2005a, Deng 2014]**. One of the main effects is a shift in the percolation threshold between the 2-D and the 3-D cases. As shown in **[Deng 2014]**, this shift is reflected also in the behavior of the GB network effective diffusivity. However, the results are valid only in the C-type diffusion regime (§Chapter 2-Section II.2.2) because the authors neglected the diffusion in the bulk and considered any leakage from grain boundaries to grains. In this section, we consider a more realistic model by taking into account the diffusion in the bulk and two types of boundaries with different diffusion properties.

3.1. Model parameters

In this section, we follow the same approach as in the study on the 2D simulated polycrystalline aggregates. The grain boundaries are randomly classified into "random" GBs (RGBs) and special GBs (SGBs). RGBs are assigned a high diffusivity coefficient $D_R = 10^{-10}$ m^2/s; while SGBs are attributed a low diffusivity coefficient $D_\Sigma = 10^{-16}$ m^2/s. The diffusivity coefficient in grains is $D_L = 10^{-13}$ m^2/s. As in the 2D study, the diffusivities values are based on the experimental results in **[Oudriss 2012b]**, obtained for polycrystalline Nickel. We do not take into account the effects of triple junctions in this study. We assume that the diffusivity of each triple junction is determined by the types of GBs surrounding it. For instance, a triple junction surrounded by at least two RGBs, is assigned a high diffusivity D_R. In order to investigate the effect of grain boundary networks on the effective diffusivity of membranes, two heterogeneous polycrystalline composites with grain sizes λ of 50 and 20 nm were modeled. The corresponding intergranular fractions are 10.9% and 23.9%, respectively. The parameters of the model are summarized inTable VII.

Table VII - Parameters used in the model

Parameter	Description	Value(s)
e_m	Thickness of the membrane	0.887 μm, 2.09 μm
d_m	Depth of the membrane	0.266 μm, 0.626 μm
h_m	Height of the membrane	0.062 μm , 0.146 μm
e_{gb}	Grain boundary thickness	5 nm
λ	Grain size	20 nm, 50 nm
C_0	Initial entry side concentration	1 mol/m^3
Cs	Exit side concentration	0 mol/m^3
D_L	Grains diffusion coefficient	10^{-13} m^2/s
D_R	RGBs diffusion coefficient	10^{-10} m^2/s
D_Σ	SGBs diffusion coefficient	10^{-16} m^2/s

The size of the simulated membranes was chosen according to the previous analysis of the membrane thickness effects on the effective diffusivity. In this section, the intergranular phase is characterized by a two GB diffusivities randomly distributed, which induce statistical fluctuations effect on the effective diffusivity, as shown above. Thus to obtain an average of the effective diffusivity, the procedure is repeated a number of times N. By using the same method presented in section (§II.1.2), we estimated the necessary minimum number of realizations to obtain relative errors of 1% and 5% (Table VIII) accordingly to equation (III.6). Due to computational limitations, a standard error of 5% on the effective diffusivity was deemed acceptable.

Table VIII - The necessary minimum number of realizations to obtain a given relative error

ε_{rel}	1%	5%
N	1440	56

As in the 2-D case, the random distribution of GB diffusivities produces two types GB network: RGB and SGB networks. Both networks can be more and less connected depending on the respective fraction of

each type of GBs (Fig. 68). However in contrast with the 2-D case, the GB clusters are represented by a chain of 3-D surfaces. Depending on the contact points, different types of connectivity can be defined in 3D polycrystalline microstructure **[Priester 2012]**, as illustrated in Table IX. In this work, we considered the case where the GB network connected through both triple junctions (J) and quadruple node (Q). Due to the complexity the GB network in 3D, we did not characterize the 3-D GB connectivity in this study.

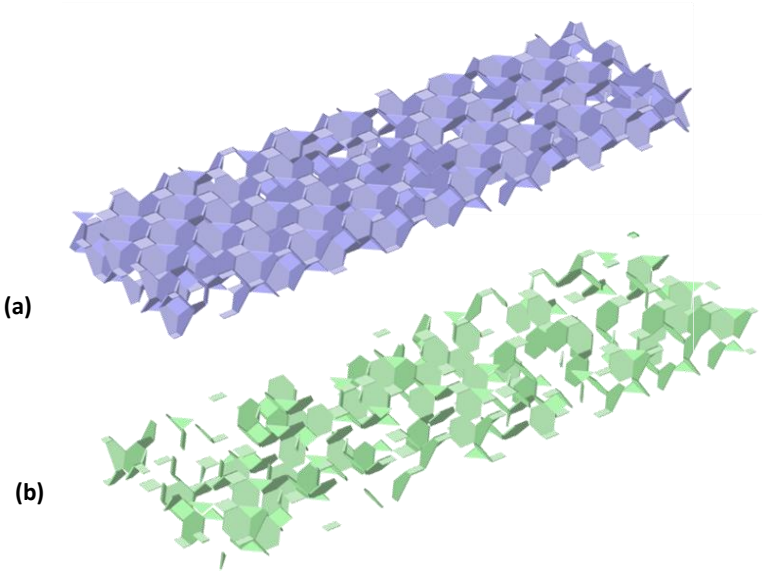

Fig. 68 - Example of GB networks in 3D for a fraction of RGBs f_R =0.6. (a) RGBs network, (b) SGBs network.

Table IX - Different types of connectivity that can be defined in 3D polycrystalline microstructure **[Priester 2012]**

Elements forming The network	Triple junctions (J)	Grain boundaries	Grain boundaries
Schematic drawing	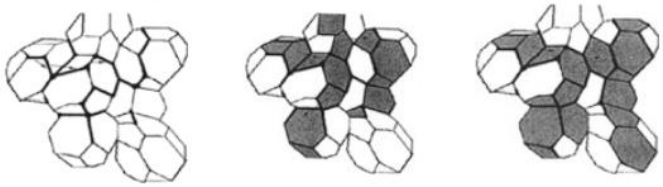		
Contact by	Q	Q+J	J
Threshold p_c	0.39	0.16	0.21

3.2. Effective diffusivity

The evolution of the normalized effective diffusivity as a function of the fraction of RGBs f_R, is depicted in Fig. 69. We observe the increase of the effective diffusivity with the fraction of RGBs. This increase is more important around the fraction f_R = 0.3. This threshold fraction corresponds also to the intersections of the two curves and according to the results in chapter II, it can be concluded that this fraction is the percolation

threshold of the effective diffusivity. The evolution of the effective diffusivity is a result of the evolution of GB network connectivity with the fraction of RGBs, similarly to the 2D study. Indeed, the geometrical percolation threshold in randomly-assembled three-dimensional grain boundary networks, formed by 2-D surfaces in a 3D lattice, was estimated at $P_c = 0.225$ **[Frary 2005a]**.

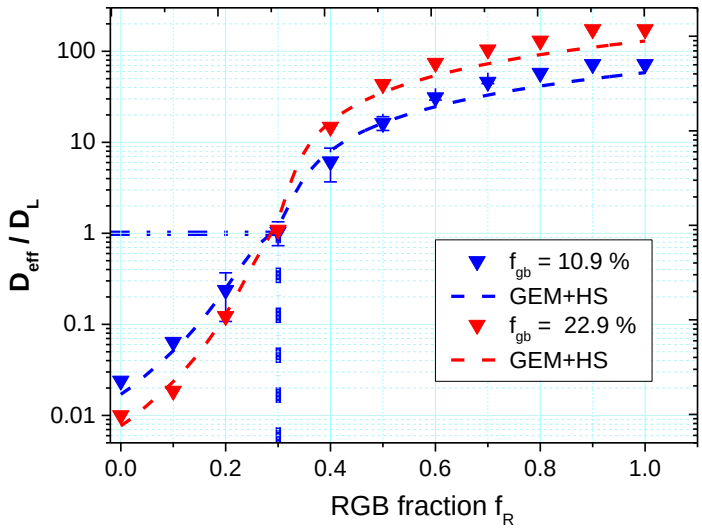

Fig. 69 – The normalized effective diffusivity as a function of the fractions of the RGBs for two membranes with different intergranular fractions.

In order to capture quantitatively the GB networks effects on the effective diffusivity, we apply the GEM+HS$^+$ approach to approximate the evolution of the effective diffusivity D_{eff}, as shown in Fig. 69. As described in the section (§IV), this approach consists in combining the general effective medium approximation (equation (III.18)), proposed by McLachlan **[McLachlan 1986, McLachlan 1987]** in the conductivity field and the Hashin–Shtrikman upper bound **[Hashin 1963]** in three dimensions (Equation (III.19)).

$$(1-f_R)\frac{D_\Sigma^{1/s}-D_{eff\_gb}^{1/s}}{D_\Sigma^{1/s}+(P_c^{-1}-1)D_{eff\_gb}^{1/s}}+f_R\frac{D_R^{1/t}-D_{eff\_gb}^{1/t}}{D_R^{1/t}+(P_c^{-1}-1)D_{eff\_gb}^{1/t}}=0 \qquad \text{(III.18)}$$

$$D_{eff}^{GM+HS}=D_{eff\_gb}+\frac{1-f_{GB}}{\frac{1}{D_L-D_{eff\_gb}}+\frac{f_{GB}}{3D_{eff\_gb}}} \qquad \text{(III.19)}$$

This phenomenological approach contains three parameters that describe the interconnection between the GB network percolation behavior and the overall diffusion of the continuum system. The best fitting between the simulations results and the GEM+HS$^+$ predictions is obtained for the values of the critical exponents s = 3±0.2

and t = 1.01±0.05 and for a percolation threshold of f_R^c = 0.3±0.02. This result shows that the approach proposed in the second chapter works also very well for diffusion in 3D nanocrystalline diffusion models. Secondly, it allows determining quantitative parameters about the GB networks effect on the effective diffusivity.

3.3. Comparison between 2D and 3D results

In order to evaluate the effect of system dimensionality on the effective diffusivity, we re-used the results of the effective diffusivity presented in the 2-D study for the membrane with grain size 20 nm and compare it to the results in 3D. The normalized effective diffusivity as a function of the fraction of RGBs for 2D and 3D membranes with the same intergranular fraction is shown in Fig. 70. It can be seen that there is a shift of the effective diffusivity between the 2-D and 3-D results, and particularly in the transition zone. This could be explained by the difference in the geometrical percolation thresholds in 2-D and 3-D GB networks. The geometrical percolation threshold is known to be dependent on the dimensionality of the system. As a result, the percolation behavior of the effective diffusivity is affected by the dimensionality of the system. This result shows that there may be large differences between the diffusivities obtained from 2-D models and the experimental values which are mostly obtained from 3-D microstructures, and particularly in the interval fractions of transitions (around percolation threshold). For instance, for the same RGB fraction f_R = 0.4, it can be seen a difference of more than one order of magnitude of the effective diffusivities. This highlights the more large effect of GB networks on the effective diffusivity in 3-D system and thus reinforces the idea that GB connectivity should be considered in the experimentally obtained diffusivity values.

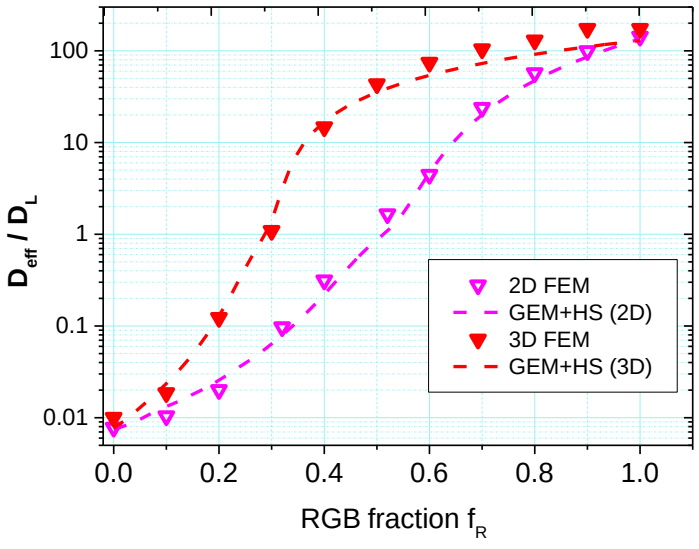

Fig. 70 – The normalized effective diffusivity as a function of the fractions of the RGBs for 2D and 3D membranes with grain size λ = 20 nm.

The fitting parameters from the 2-D and 3-D calculations are summarized in Table X. In addition to the percolation threshold of the effective diffusivity which has decreased, it can be noted that only a critical exponent, namely *t*, changed between 2D and 3D. This result is interesting because the scaling exponents usually depend on the space dimensionality **[Sahimi 2003]** and the fact that *s* does not evolve is a surprise. The decrease in *t*, compared to the 2-D, is probably related to a more important effect of the percolated cluster in 3-D system. Indeed, the critical exponent *t* characterize the divergence of the effective diffusivity above the percolation threshold ($f_R > f_R^c$) and thus capture the effect of the percolated cluster.

Table X- Scaling exponents of the effective diffusivity

	2D	3D
f_R^c	0.52 ± 0.02	0.3±0.02
s	3 ± 0.2	3±0.2
t	1.8 ∓ 0.15	1.01±0.05

VI. Discussion

1. Overview and analysis of the results

In this work, the effects of the GB connectivity on the macroscopic diffusivity in polycrystalline materials were investigated. Both idealized and reconstructed microstructures were used to simulate H-permeations in two and three dimensions. Unlike previous studies **[Legrand 2013b, Jothi 2014]**, the grain-boundary region was modeled by a heterogeneous phase (random and special GBs), with two distinct diffusion coefficients.

The first approach of this work consisted in working on idealized 2-D simulated microstructures, with a random distribution of grain-boundary diffusion properties. This allowed us to perform a statistical characterization of the connectivity of random boundaries. The results showed clearly three different topological behaviors (system of path, large clusters and percolating clusters) depending on the fraction of RGBs. Then we analyzed in detail the correlation between the effective diffusivity and the connectivity parameters (average path length, correlation length). It was found a non-linear dependence of the effective diffusivity on the correlation length on the whole interval of the fractions of RGBs. However, we observed that, by taking the three interval of the fraction of RGBs corresponding to the different topological domains, we had linear relationships between the effective diffusivity and the connectivity parameters. It was found a significant increase of the effective diffusivity as a function of the correlation length ξ, in the domain of large

clusters. In this domain, the slope of the linear relationship was more important for nanocrystalline membranes, compared to micro-crystalline membranes.

These findings proved the important role of GB connectivity on the effective diffusivity, and more particularly in nanocrystalline materials. However, it is important to view these results in perspective, as we focused only on the GB connectivity and neglected the connectivity between grains and each category of grain boundaries. To analyze the problem as a continuum percolation transport we proposed a homogenization deductive approach, based on the combination of the generalized effective medium and the Hashin-Shtrikman formulas. The results of this analysis showed that the percolation threshold of the effective diffusivity is different from the geometrical one of the GB network. This suggests that the percolation behavior of the effective diffusivity depends on the contacts between all the different phases in the system. The studies on the percolation behavior of effective properties in continuum system are very rare. To our best knowledge, Chen and Schuh **[Chen 2009]** are the first who analyzed the question by considering transport through a two phase continuum square system. In their study, the authors investigated the effects of corners contacts and showed that they can influence the percolation of the effective diffusivity. In the same study, it is reported that the continuum scaling exponents are asymmetrical and different from their lattice counterparts, which is consistent with our results. This study also raised the question of universality of continuum percolation and the fact that more studies are necessary to elucidate the question. It should be noted also that the scaling exponents reported in the literature are in the range of 1-2 **[Sahimi 1994]**, which is not the case for the scaling exponent *s* obtained from our fitting. This point reinforces the idea of non-universality of the percolation in continuum systems. However the percolation in continuum transport remains complex and further studies are necessary.

In a second part (section §V), we analyzed the effects of the space dimensionality on the percolation behavior of the effective diffusivity, showing a decrease of its percolation threshold. This is a result of the geometrical percolation threshold of 3-D GB networks, which is smaller than in 2-D GB networks, as reported in the literature **[Frary 2005a]**. This result suggests that the different correlations established between the connectivity parameters and the effective diffusivity in 2-D systems should be different in three dimensional cases. Indeed, the GB connectivity seems to increase faster than in 2-D, thereby the effect of large clusters may occur for lower fractions of random boundaries.

In summary, the results of this numerical approach pointed out different correlations between grain-boundary connectivity and the macroscopic diffusivity, depending on the fraction of random boundaries or the space dimensionality. The study highlighted also that the continuum percolation behavior of the effective diffusivity is different from that in discrete networks. In the current approach several assumptions were made, through the physics applied and also the microstructure modeling. The main simplifications of the approach and their implications are discussed in the next section.

2. Discussion on the simplifications of the numerical approach

1. The binary classification of GB diffusivities

In our numerical study, we used a binary classification of grain boundaries, based on geometric property, namely the coincidence index Σ. This approach is widely used because it has a significant advantage. It helps reduce the number of significant parameters that characterize grain boundaries and it is applicable to many areas such as corrosion resistance, fracture propagation and electromigration **[Gertsman 1996, Watanabe 1999, Kononenko 2001, Lehockey 2004]**. In regard to the GB diffusivity, this classification is still controversial because direct relationship between this crystallographic property and the GB property has not been elucidated **[Priester 2006]**.

In the current approach, we assigned a low diffusivity to the special GBs ($\Sigma<29$) and a high diffusivity to random (often also called general) GBs. This choice is based on experimental findings in **[Oudriss 2012b]**. According to Oudriss *et al*., the increase of hydrogen diffusion along random GBs can be explained mainly by the presence of strong distortions and large regions of poor structural match inside this type of GBs. On the contrary, most of special GBs are presented as preferential area for hydrogen trapping because of a favorable atomic structure characterized by a good fit between the interfacial atoms and the adjoining crystals and weak distortions. However, it is difficult to find diffusivity data associated to each category of GBs. Only some atomistic simulations have determined diffusion constants for specific GBs **[Suzuki 2004, Pedersen 2009, Di Stefano 2015]**.

In this work, diffusivity in random boundaries is assumed three orders of magnitude higher than in crystal, based on our previous works **[Oudriss 2012b]**. Ratio between GBs and lattice diffusivities reported in the literature varies from one to four orders magnitudes **[Tsuru 1982, Yao 1988, Harris 1991, Palumbo 1991a, Brass 1996]**, without specifying the category of GBs. For the special boundaries, quantitative results of the delaying effect of trapping on the GB diffusivity are even more limited. In our study, we assumed a diffusivity three order of magnitude smaller than in crystal. This value seems to correspond to extreme case where the GBs present high density of deep trapping sites **[Kumnick 1974, Thomas 2002]**. Without a high contrast ($D_R/D_\Sigma > 10^4$) between the diffusivities of the two types of boundaries, it has been found that the effects of GB connectivity on the effective diffusivity seem to be negligible **[Chen 2006]**. This is consistent with our numerical results. The normalized effective diffusivity calculated from the 2-D simulated FEM model, as a function of random boundaries for different ratios, is illustrated in Fig. 71. It can be seen the effect of RGBs becomes significant for ratios higher than 10^4. Below this ratio, the effect of GB connectivity can be neglected and common homogenization models can provide accurate description of the effective diffusivity **[Chen 2006]**.

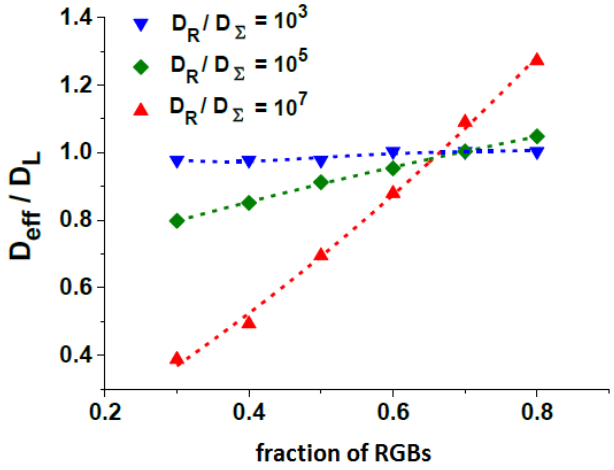

Fig. 71- Evolution of the effective diffusion coefficient as a function of the random grain boundary volume fraction for different contrasts of the random and special grain boundary diffusivities. Other parameters kept constant. Grain boundary thickness e_{gb} = 5 nm, grain size λ = 10 µm, membrane thicknesses e_m = 500 µm.

2. Influence of triple junctions on the effective diffusivity

In our numerical approach, each triple junction was assigned the same diffusivity as the surrounding GBs. However, the triple junction diffusivity is generally found to be higher than in GBs or in lattice **[Palumbo 1990b, Doyle 1995, Bokstein 2001, Wang 2005]**. In addition, triple junctions occupy a significant portion of the intergranular region in nanocrystalline materials **[Palumbo 1990b]**. These entities can form a high diffusivity percolating network throughout the volume of the material. Legrand investigated the triple junction effects on the effective diffusivity using 3-D simulated networks in his PhD thesis **[Legrand 2013a]**. According to his simulation results, a significant increase (on order of magnitude) of the effective diffusivity compared the case where the triple junction diffusivity is not considered. However, in his study, the segregation behavior of triple junctions was not taken into account and the considered TJ diffusivity was chosen arbitrarily. In reality, the study of triple junctions' effects is complicated by the lack of experimental data on their diffusion property and segregation behavior.

In summary, a complete description of diffusion in polycrystalline would require to consider the triple junction effect, in addition to the grain boundaries effect. This could bring an alternative explanation of the non mono-atomic dependence of the effective diffusivity on the grain size observed for experimental data **[Oudriss 2012b]**. However, the numerical analysis of triple junctions' effects would make sense only with in three dimensional realistic microstructures.

VII. Concluding remarks

In this chapter, hydrogen diffusion through heterogeneous materials, modeled by a ternary continuum composite media, was simulated. Then, the effect of grain-boundary networks on macroscopic diffusivity was investigated. Four main results can be underlined:

- *Depending on the RGB fraction, the RGB networks can be classified into three groups characterized by differences in morphology and statistical distributions of their connectivity parameters.*

- *It appears a strong correlation between the grain boundary transition threshold and the maximum of increase in the effective diffusivity. This influence is more pronounced for nanoscaled membranes, compared to fine grained membranes.*

- *As a consequence of the three groups of networks, we highlighted three different regimes of diffusion. In each regime of diffusion, linear correlation between the effective diffusivity and the grain-boundary morphology parameters was detected.*

- *By combining the generalized effective medium (GEM) equation and the upper Hashin-Shtrikman formula, we proposed an approach to approximate the effective diffusivity obtained from the FEM simulations. This approach allowed to extract the continuum percolation threshold and the scaling exponents of the effective diffusivity in the polycrystalline aggregate. This evidences that the percolation behavior of the effective diffusivity is affected also by the intra-granular diffusion.*

- *By treating the heterogeneous materials as 3-D ternary composite with two types of grain boundaries, we investigated the implication of the dimensionality of the system on the correlation between the GB connectivity and the effective diffusivity. As well as in 2-D, The evolution of the effective diffusivity is controlled by the changes in the GB network connectivity and topology. However, we observe a shift in percolation threshold of the effective diffusivity compared to the 2-D results. This shift is a result of the grain-boundary network connectivity which is different in 2-D and 3-D. In addition, we extend the homogenization approach proposed in 3-D.*

This numerical work has been conducted on simulated aggregates with idealized geometries. However, it is not sufficient to describe the actual behavior of polycrystalline material, particularly because realistic microstructures involve irregularly shaped single crystals and local microstructural constraints. This point will be questioned in the next chapter.

Chapter 4

Diffusion in realistic heterogeneous microstructures

In the third chapter, we have shown that the effective diffusivity of hydrogen in polycrystalline materials depends strongly on the connectivity and the percolation behavior of the GB networks. However, these analyses were conducted using idealized microstructures with a random distribution of the GB diffusivities. This chapter combines numerical and experimental analyses. It is aimed at first investigating the GB connectivity effects on the effective diffusivity in realistic microstructures and secondly at providing insights on the GB effects on hydrogen local concentration.

I. FEM analysis of the hydrogen diffusion in reconstructed polycrystalline aggregates

1. Introduction

It is known that the behavior of realistic microstructures differs from the idealized ones, due to more complicated physics and more microstructural constraints. Polycrystalline materials consist of irregularly shaped single crystals joined by grain boundaries which present a wide range of properties. Moreover, the GB characters distribution (GBCD) is subjected to crystallographic constraints **[Gertsman 1995, Gertsman 2001]**. Particularly, it has been proven that, when three CSL boundaries meet at triple junction, their Σ values must verify a "sigma combination rule", **[Miyazawa 1996]**, as reviewed the chapter 2 (§II.1.3).

The influence of the crystallographic constraint on the GB topology and connectivity was investigated by Frary *et al*. **[Frary 2004, Frary 2005b]**. It has been shown that preferential GB cluster configurations were induced by these constraints **[Frary 2005b]**. The authors also found that the non-random distribution of the GB characters lead to a shift of the geometrical percolation threshold, compared to the analytical value obtained from the percolation theory. These findings pointed out the importance of considering a realistic distribution of the GB properties to better analysis the correlations between the GB connectivity and the effective properties of materials. In order to connect the numerical simulations and the experimental data on hydrogen diffusivity, it is necessary to include information on the grain boundary character distribution in the FEM diffusion model, by performing microstructural characterizations.

It is difficult to compare simulation results and experimental data due to low availability of appropriate experimental data on GB diffusivities. To our knowledge, diffusion measurements in polycrystals from the perspective of microstructure are rare. Oudriss *et al.* **[Oudriss 2012b]** provided large experimental data set on hydrogen diffusivity in polycrystalline Ni with a wide range of grain size (Fig. 72), using electrochemical permeation tests. These diffusion measurements were combined with GB characterization and GB connectivity analysis. This study allowed them to retrieve an effective GB diffusivity of $D_{gb}= 4.10^{-10}$ m²/s by using a fitting procedure of the Hashin-Strickman approximation and the experimental data of the effective diffusivities calculated from the desorption step. According to the authors, the effective diffusion coefficient ($D_{eff,d}$) determined from the desorption step corresponds to the hydrogen diffusion without strong trapping effect, while the effective diffusion coefficient ($D_{eff,c}$) determined from the charging step is affected by the trapping processes. This theory could explain the large discrepancy of the values of diffusivities from the two methods.

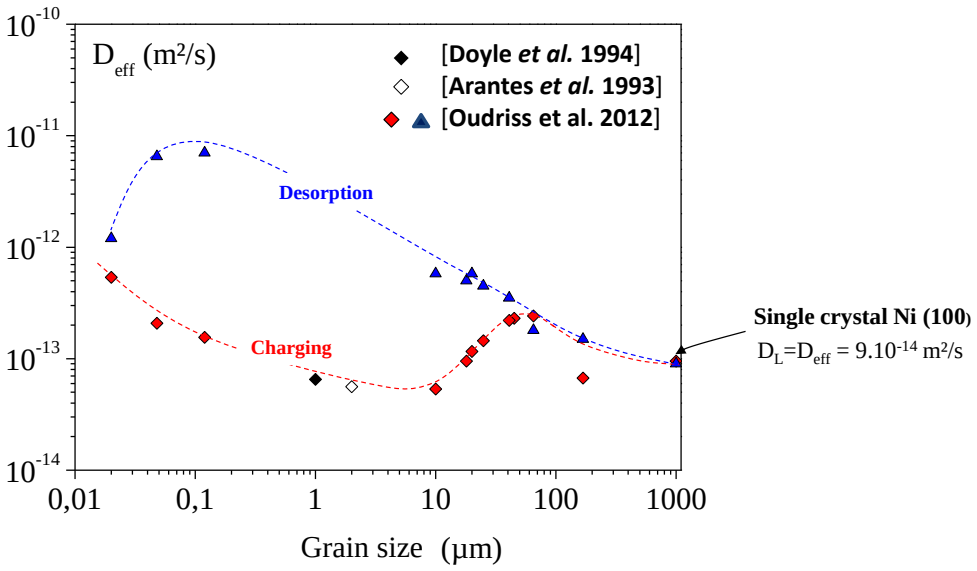

Fig. 72 – Experimental data on the evolution of the effective diffusivity as a function of the grain size, by considering hydrogen charging and desorption **[Oudriss 2012b]**.

The aim of this section is to study the effect of GB connectivity on the effective diffusivity in realistic microstructures, based on Electron backscatter diffraction (EBSD) maps of polycrystalline Ni. For that, as in the last chapter, we combine GB connectivity characterization and FEM simulations of H-permeations. Firstly, we present the experimental procedure to obtain EBSD maps and the computational procedure to build the EBSD-based FEM. Then, the connectivity of the reconstructed GB networks is quantified and compared to the results of the randomly assembled networks in chapter III. Finally, the FEM results of the effective diffusivity are confronted with experimental data from the literature.

2. Experimental procedure

2.1. Materials and characterization

Three different microstructures were used in this study: two polycrystalline Ni with micrometric average grain size and one nancrystalline Ni. The latter, obtained by electrodeposition process, comes from the PhD works of Dr. Godon **[Godon 2010]**. The two others are from polycrystalline nickel (purity 99.99%) provided by Goodfellow company. Grain sizes were obtained by thermo-mechanical processing at constant temperature for a predefined time in a controlled atmosphere on nickel cold-drawn round rods **[Haddou 2003, Feaugas 2007, Oudriss 2012b]**.

To obtain the microstructural geometry and the crystallographic data, EBSD analyses were performed on the samples. Initially, the samples were prepared by SiC surface grinding up to 4000 grade and then electropolished in H_2SO_4/CH_3OH acid solution **[Sahal 2004, Lekbir 2013]**. The polishing procedure is described in appendices XX. The orientation data were obtained using an EDAX/TSL OIM system coupled to a FEI Quanta 200 ESEMFEG scanning electron microscope. Operating conditions of 20 kV and 0.2 μm step size were used. Automatic beam scanning and the TSL OIM Data Collection 5 software were used to map the crystal orientations on planar sections. Two of the three microstructures used in this work were characterized during the PhD works of Godon **[Godon 2010]** and Oudriss **[Oudriss 2012a]**. One microstructure was characterized during this work, following the same procedure. For more details on the characterization procedure, readers are referred to the works of Godon and Oudriss **[Godon 2010, Oudriss 2012a]**.

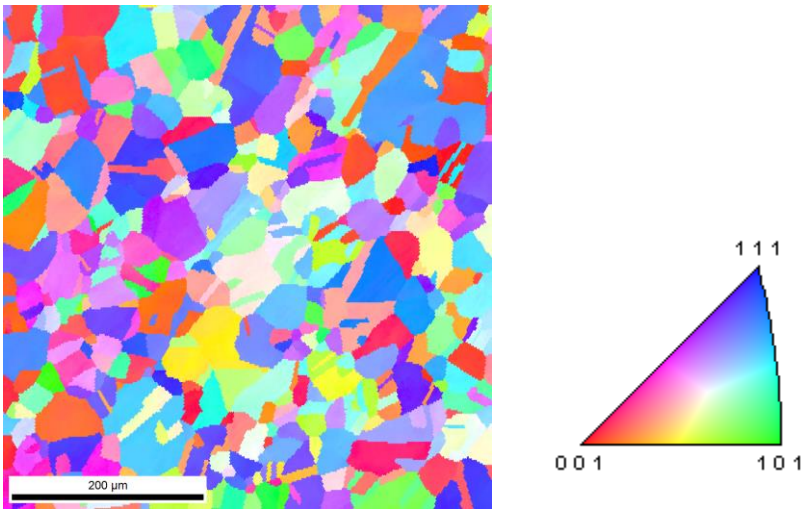

Fig. 73 – EBSD orientation map of the Ni sample with grain size 45 μm from present work.

The obtained EBSD maps were post-treated using the TSL OIM analysis 5 software. Precisely, a cleaning-up procedure was performed on all EBSD maps to adjust single points with misorientations higher than 5° with its neighbors.

3. Computational procedure

3.1. Reconstruction of the microstructure

In order to build an image-based FE Model, a procedure to extract the geometrical data from the EBSD analysis and convert it into Comsol mesh was developed. Initially, by using the OIM analysis

software, the grain boundaries were approximated by a set of lines. Then, the following information was extracted for each map:

- The coordinates of the endpoints of each line
- The average orientation of the adjacent grains.

This information was used in a set of scripts implemented in Comsol with Matlab. Firstly, the microstructures were reconstructed as in the EBSD maps. Then, a dilatation algorithm was applied on it, in order to make the boundaries thicker. A reconstructed microstructure is shown in Fig. 74. This operation treats boundaries as a separate domain with a finite thickness and different diffusion properties against the bulk. Afterward, a mesh was generated from the reconstructed microstructures. Domains comprising grains and triple junctions were meshed with triangular elements, while mapped mesh is applied to the grain boundaries. By imposing three boundary elements on the triple junctions, three elements are ensured in the thickness of the grain boundary, as illustrated in the Fig. 75.

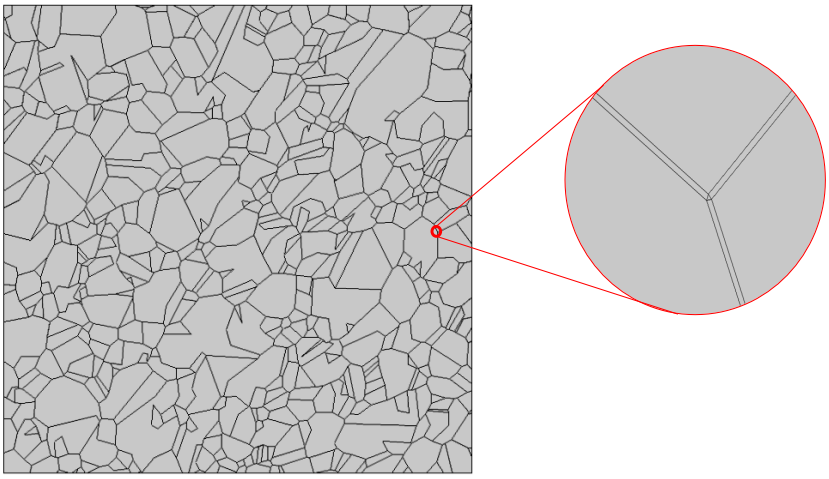

Fig. 74 – Reconstructed microstructure with thick boundaries shown in the inset.

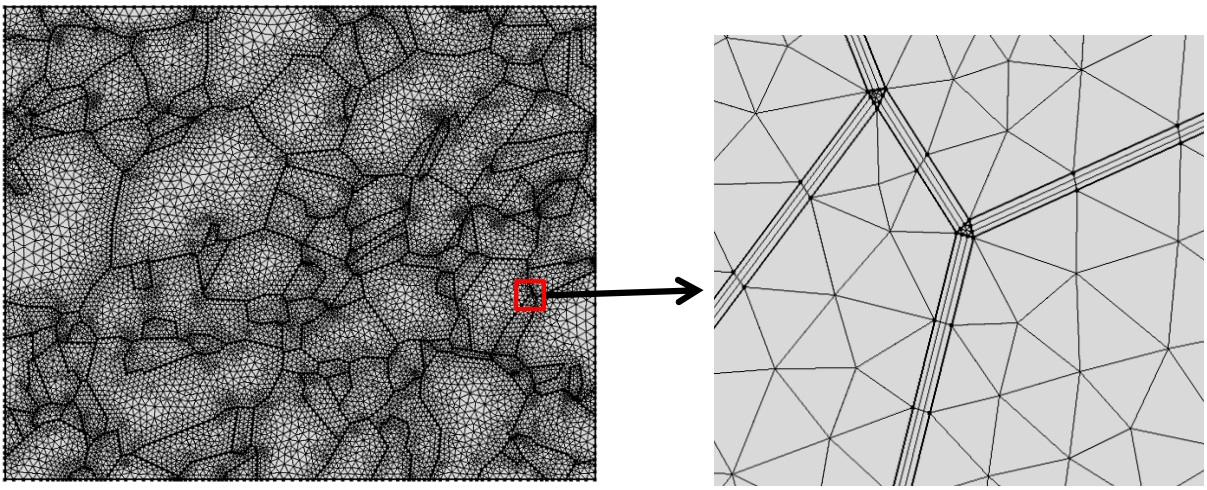

Fig. 75 – FE mesh of the reconstructed boundaries.

3.2. Permeation modeling

The permeation modeling follows the same approach as in the 2-D model of the third chapter. As illustrated in the Fig. 76, a constant hydrogen concentration C_0 is imposed at the left side and a zero concentration at the exit side. This results in a concentration gradient from the entry to the exit side of the membrane. The hydrogen diffusion is governed by Fick's laws, implemented on each node following the equation (IV.1). The isotropic hydrogen diffusion coefficient D_i is dependent of the position in the different phases. The same diffusion coefficient D_L is used for the grains, while each GB is assigned either a high diffusion coefficient D_R or low diffusion coefficient D_Σ otherwise depending on their character. Unlike the third chapter, the GB diffusivity is not randomly assigned but is based on the EBSD map. Using the EBSD data, grain boundaries were classified into two categories: special boundaries with diffusivity D_Σ and general or "random" boundaries with diffusivity D_R. Special boundaries comprise low angle boundaries and CSL boundaries with high coincidence ($\Sigma<29$). Random boundaries include high angles boundaries without coincidence or long range coincidence (($\Sigma>29$). An example is illustrated in Fig. 77. This binary classification was transferred into the FEM model.

$$\frac{\partial C}{\partial t} = \nabla \cdot (D_i \nabla C) \qquad \text{(IV.1)}$$

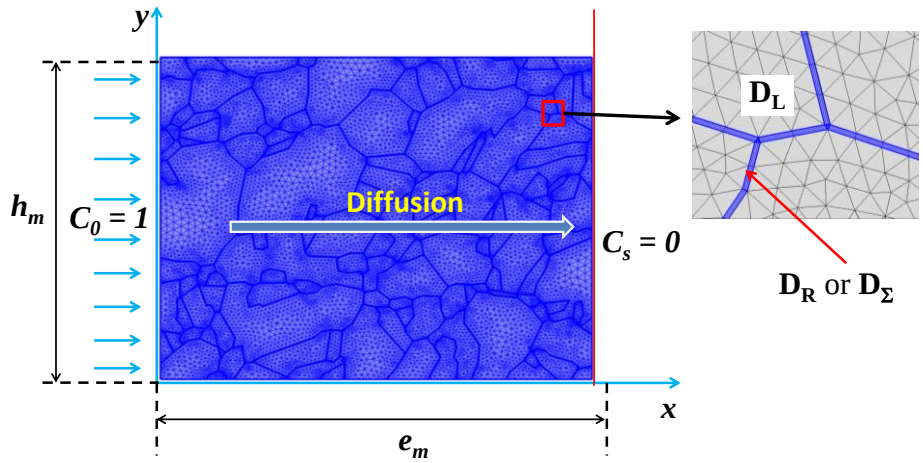

Fig. 76 – FE modeling of the permeation on the reconstructed microstructures. As in the third chapter, the membrane thickness and height are called e_m and h_m, respectively.

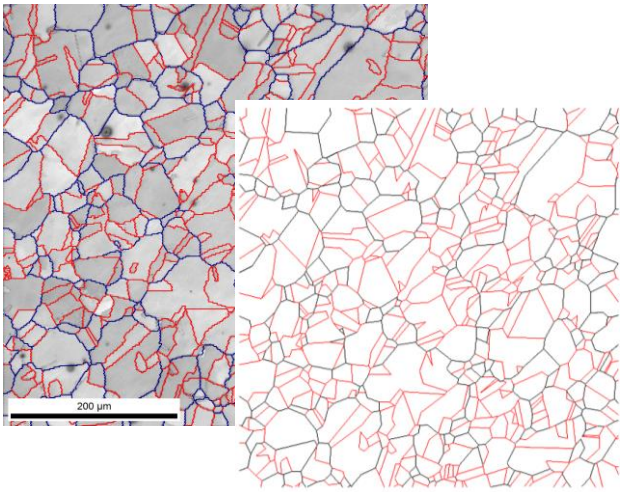

Fig. 77 – EBSD map and the resulted binary classification of boundaries.

3.3. Parameters of the models

The FE calculations were conducted on three EBSD-based models of Ni with average grain sizes λ of 45, 18 and 0.12 µm. The 2D-EBSD experimental microstructural image of polycrystalline Ni and the FEM geometries are shown in Fig. 78. For each grain size two or three different EBSD maps were used in order to gain insight of the variability of measured data. An arbitrary constant GB thickness of 10 nm was defined for the grain boundaries. This value is very large compared to the usually reported values of GB thickness. However, it can be seen as an effective GB thickness that represents the enhanced diffusion or the segregation zone inside and around the GB. The boundary conditions and the geometrical parameters are reported in Table XI.

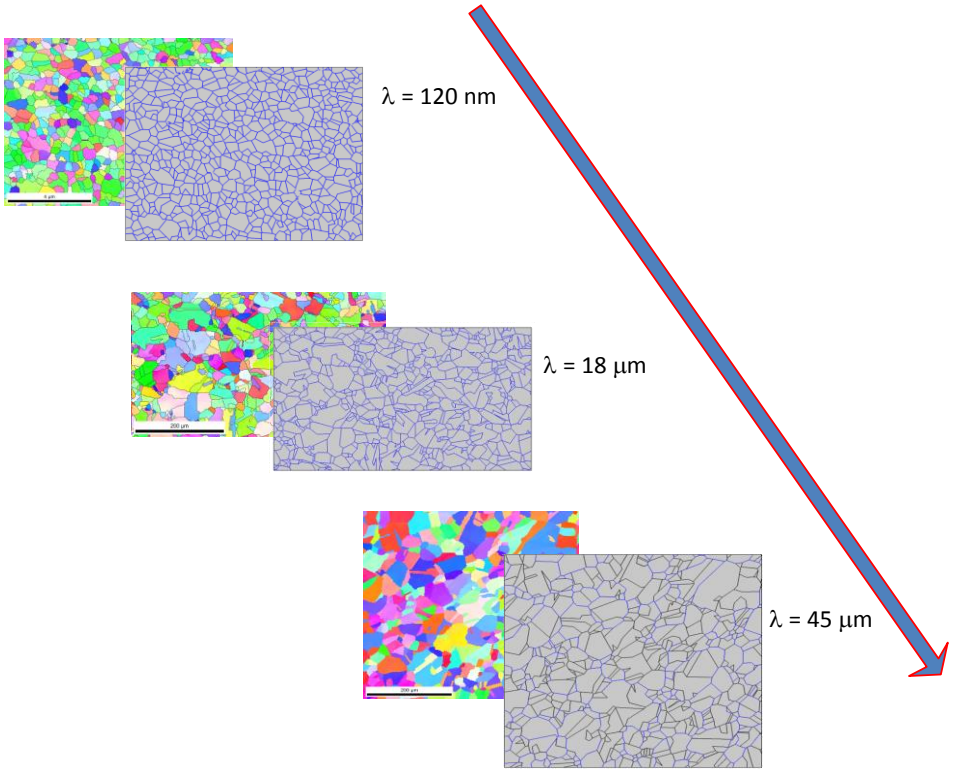

Fig. 78 – EBSD orientation maps and the corresponding reconstructed boundaries.

Table XI – Parameters of the model

Parameter	Description	Values
e_m	Thickness of the membrane	10.8 – 570 µm
h_m	Height of the membrane	8.6 – 500 µm
e_{gb}	Thickness of the grain boundaries	10 nm
λ	Grain size	180– 45000 nm
C_0	Entry side hydrogen concentration	1 mol/m^3
C_S	Exit side hydrogen concentration	0 mol/m^3

4. Results

4.1. Grain boundary Connectivity

In order to investigate the GB connectivity, reconstructed grain boundary maps were obtained from the COMSOL models. Using the information from the EBSD, the GBs were classified into Special (SGBs) and random (RGBs). The reconstructed GB networks of the two types are shown in Fig. 79. Visually, it can be seen that RGBs are more connected that SGBs. However, the respective fractions of the two categories of boundaries do not show the same the trend, as illustrated in Fig. 80.

Furthermore, we quantified the connectivity of the different networks by determining two parameters: the correlation length of the clusters and the fractions of triple junctions of different nature.

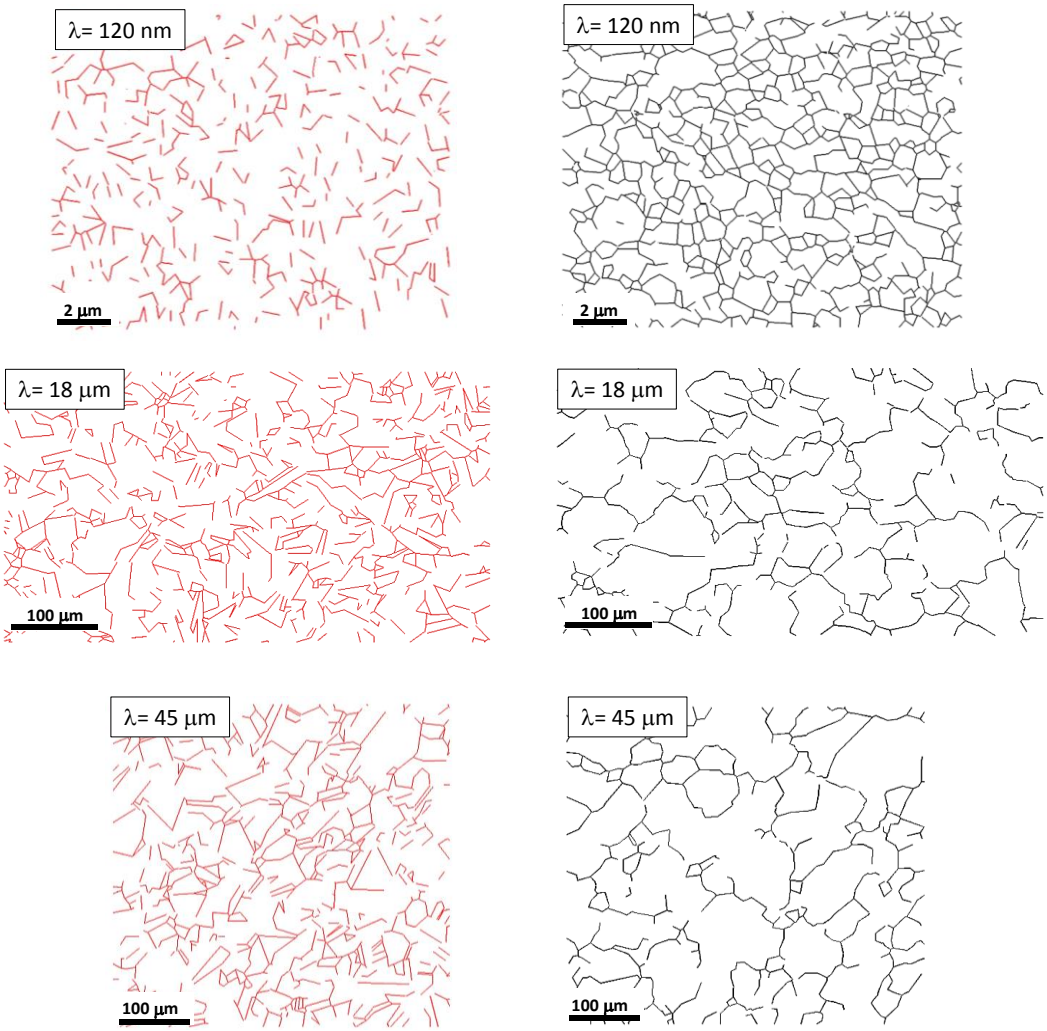

Fig. 79 – Special (red) and random (black) boundaries networks for the three microstructures with grain sizes λ= 120 nm, λ =18 μm and λ = 45 μm.

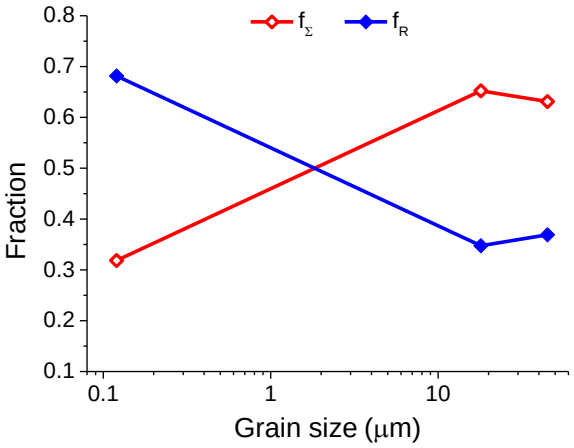

Fig. 80 – Fraction of each type of boundaries for the three microstrucures

The first step of the GB networks characterization was to convert the images into binary images. Then we applied exactly the same procedure previously described in the third chapter (section §II.2) to calculate the correlation length ξ. The results are depicted in Fig. 81a. As foreseen after the observation of the GB networks images, the correlation length show that the connectivity of RGBs is higher than that of SGBs. We compared the values of the correlation length of the RGB clusters to those obtained for the randomly assembled GB networks from the third chapter, as reported in Fig. 81b. It can be seen a large discrepancy between the correlation length of the randomly assembled GB networks and the real networks, more particularly for the low fraction of RGBs. This result is not surprising because the spatial distribution of GB of different nature is affected by crystallographic constraints, as mentioned above. Following the results of the correlation length, it can be concluded that the fractions of boundaries of each type are not good indicators of the GB connectivity.

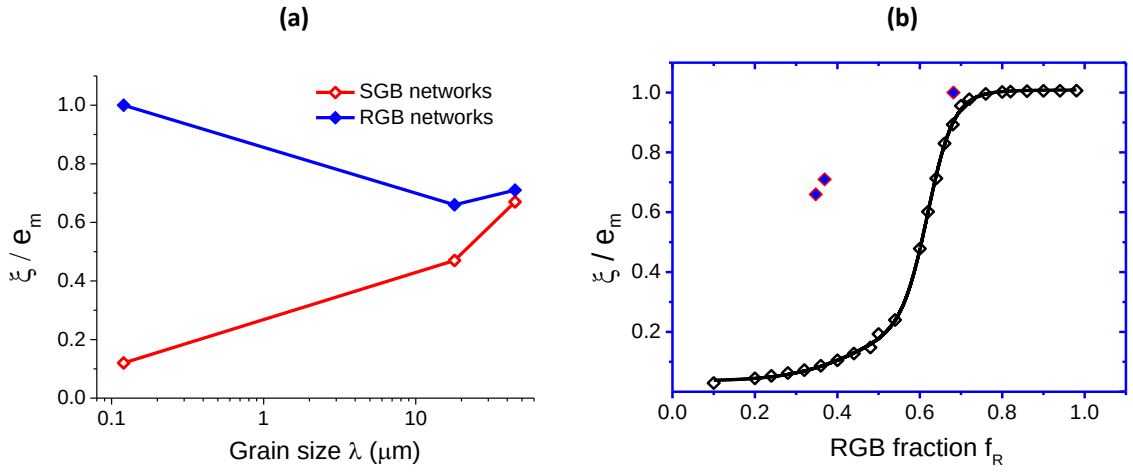

Fig. 81 – (a) Normalized correlation length ξ of the reconstructed GB networks as a function of the grain size. (b) Normalized correlation length ξ of the reconstructed RGB networks and RGB simulated networks.

To go further, we used another parameter to quantify the GB connectivity. As discussed in the second chapter (chapter 2, §IV.2), the fraction of different types of triple junctions was suggested to be a good measure of the GB connectivity. According to the nature of the grain boundaries that form it, a triple junction can be classified into four types: 0-SGBs, 1-SGBs, 2-SGBs and 3-SGBs, with fractions J_0, J_1, J_2 and J_3 respectively. The four cases are illustrated in Fig. 82. The 0-SGBs and 1-SGBs types triple junctions are qualified random triple junctions and the 2-SGBs and 3-SGBs types are special triple junctions.

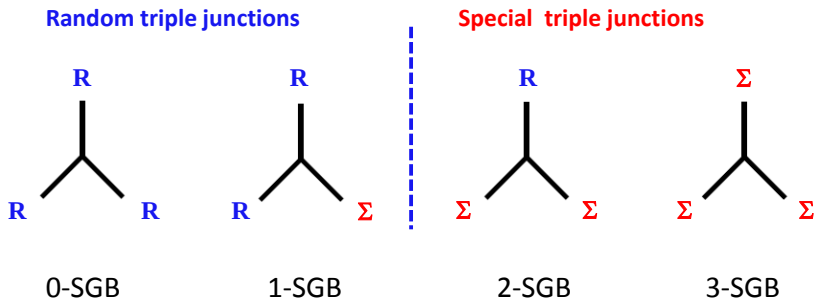

Fig. 82 - Classification of triple junctions depending on the number of SGBs that compose them.

We determined the fractions of random triple junctions (J_0+J_1) and that of special triple junctions (J_2+J_3) for the three microstructures. The result is reported in Fig. 83. It can be seen that the fraction of random triple junctions is more important than that of special triple junctions. This reflects the higher inter-connectivity of RGBs and could explain the evolution of the correlation lengths of the RGBs and SGBs clusters as shown in Fig. 81a. A linear correlation was found between the correlation lengths of the RGB clusters and the fractions of random triple junctions (J_0+J_1), as illustrated in Fig. 84. This is an important result that corroborates previous studies **[Kumar 2000, Minich 2002, Schuh 2003b]**. This result confirms that the fractions of triples junctions of different nature are a better indicator of the connectivity than the fraction of different type of GBs.

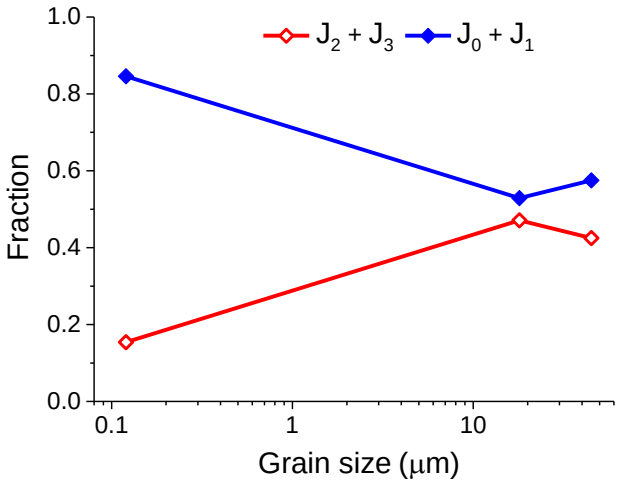

Fig. 83 – Fractions of random and special triple junctions as a function of grain size

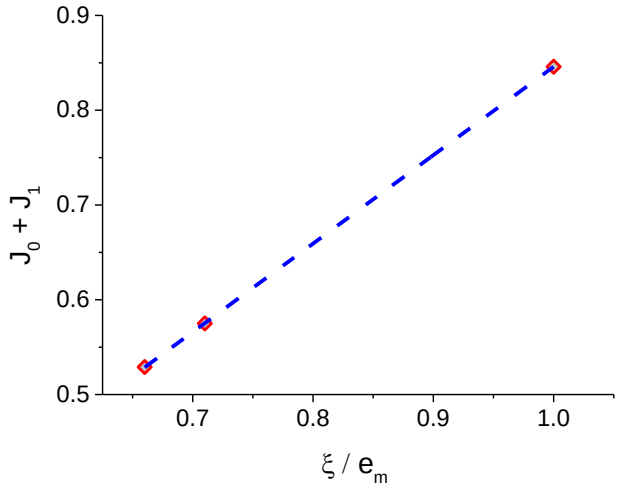

Fig. 84 - Fractions of random triple junctions as a function of the correlation length of the RGB clusters

In summary, following the correlation lengths and the fraction of random triple junctions, it can be concluded that the RGBs are more interconnected than the SGBs for the three microstructures. For the nanocrystalline one, the percolation of the RGBs is even ensured as indicated by the correlation length. This means that the diffusion process along grain boundaries for these three microstructures will be affected the RGBs diffusivity.

4.2. Effect of high angles random boundaries on the effective diffusivity

As just explained, the RGBs are more interconnected than the SGBs in the three studied microstructures. To investigate the effect of this higher connectivity of random boundaries, we

simulated the hydrogen diffusion through the three reconstructed microstructures. Then, the effective diffusivities were calculated for the three different heterogeneous models by using the same procedure than in the 2-D hexagonal models. To be able to compare the FEM results to the experimental data of the desorption step, we considered the same diffusivity parameters than the experimental measurements: $D_R = 4.10^{-10}$ m²/s in the random boundaries and $D_L=D_\Sigma = 9.10^{-14}$ m²/s in lattice and special boundaries.

The results of the effective diffusivities as a function of the grain size are reported in Fig. 85. In the same figure, we plotted the experimental data from **[Oudriss 2012b]**. We also repeated the 3-D Hashin-Shtrikman **[Hashin 1963]** approximation in the Fig. 85, as proposed in **[Oudriss 2012b]**. It can be seen that our FEM simulation results are slightly different from the experimental data but still follow the same trend. The increase in the effective diffusivity, due to the high-angle random boundaries can be observed and more particularly of the nanoscale membrane.

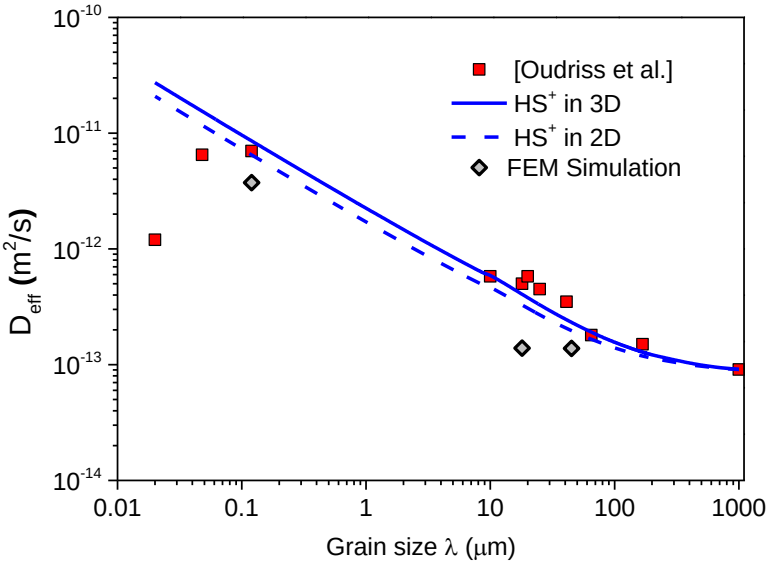

Fig. 85 - The effective diffusivity as a function of the grain size. Comparison between the results of the EBSD-based FEM simulations, the experimental data from **[Oudriss 2012b]** and the predictions of the upper Hashin-Shtrikman (in 2-D and 3-D).

The difference between the FEM simulation results and the experimental may be due to the dimensionality of the system. As shown in the third chapter, there can be discrepancies between the 2-D and the 3-D results because of the grain-boundary connectivity effect. However, this is not the only factor. As shown on Fig. 85, our FEM results are slightly different from the 2-D HS approximation. Some other possible explanations would be the non-consideration of the triple junctions' diffusivity or the loss of geometrical information in the reconstruction process. Indeed, a number of studies reported that triple junctions contribute to the diffusion acceleration, especially for nanocrystalline microstructures **[Palumbo 1991a, Doyle 1995, Wang 2005]**.

In the previous result, the same diffusion coefficient was considered in the bulk and in the special boundaries in order to be coherent with the experimental work. However, in the approach of the third chapter, we always considered a very slow diffusivity in the SGBs compared to the bulk ($D_L \gg D_\Sigma$). To check if there is any difference in the effective diffusivities calculated with the EBSD-based FEM model, we compared both cases, as reported in Fig. 86. It can be seen that the SGB diffusivity has no significant effect on the effective diffusivity. For the nanoscaled membranes, this is explained by the very low connectivity of SGBs compared to the RGBs (Fig. 81a). For the two others microstructures (λ= 18μm and λ = 45 μm), there are two reasons: first, the SGB connectivity is little lower than the RGB connectivity (Fig. 81a, Fig. 83), secondly, the effect of the GB connectivity on the effective diffusivity is not important at this scale. This result is consistent with our analyses in the third chapter on the correlation between GB connectivity and the effective diffusivity. However, the slower diffusivity may affect the local concentration distribution at the steady state, which will be discussed in the next paragraph.

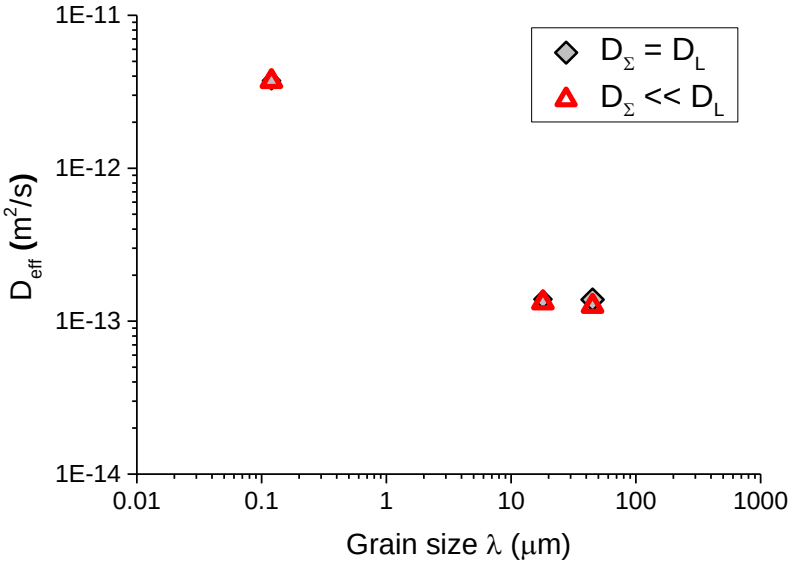

Fig. 86 - The effective diffusivity as a function of the grain size for two values of D_Σ ($D_\Sigma = D_L$ and $D_\Sigma = 9\times10^{-16}$).

4.3. Effects of the GBCD on the hydrogen concentration distribution

In the method of solving the Fick's equation, it is assumed that the system is homogeneous at the steady state and the concentration profile is linear within the thickness of the membrane **[Kuhn 1991]**. However, this is not always the case when grain boundaries present different diffusion properties from the bulk. It has been shown that the concentration profile is affected by the geometric distribution of the microstructure **[Legrand 2013a]**. To analyze this point, we plotted in Fig. 87, the

surface profile concentration and the evolution of the hydrogen concentration in the thickness of the membrane at steady state for two microstructures.

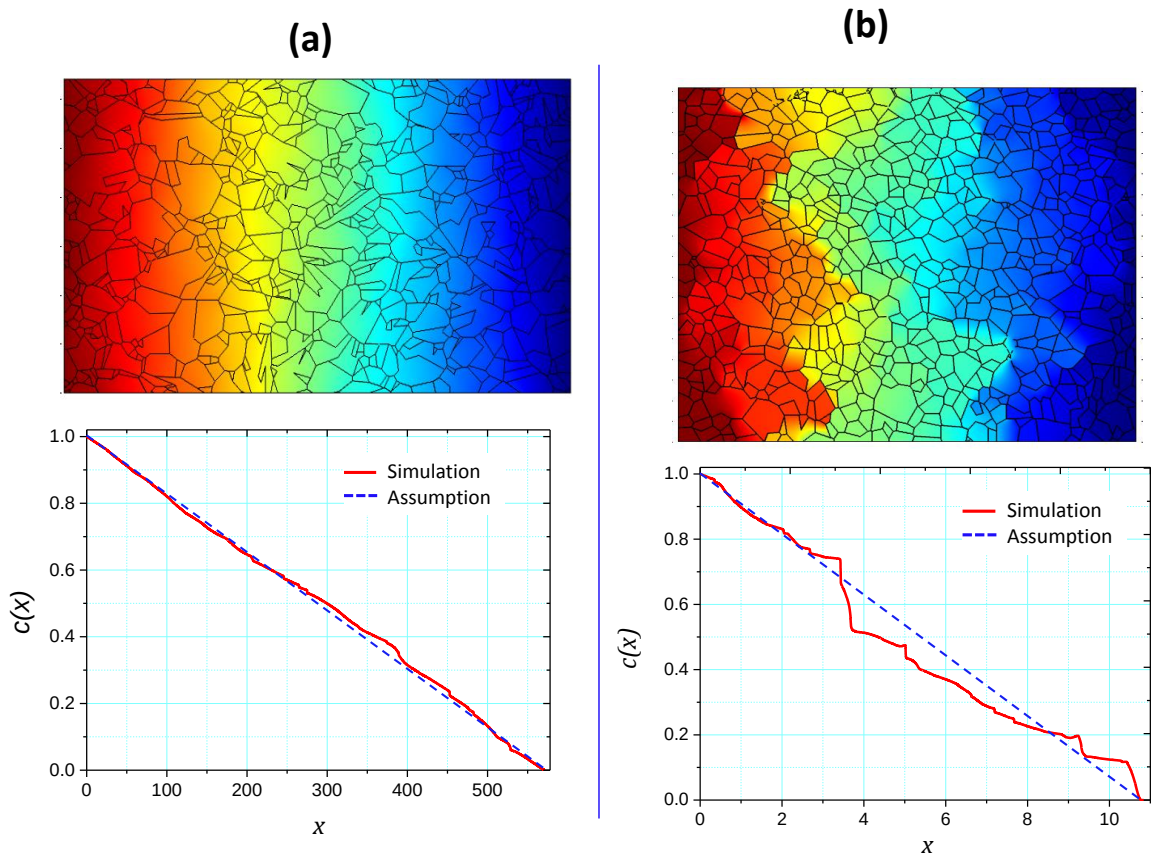

Fig. 87 – Surface profile concentration and the evolution of the average hydrogen concentration in the thickness of the membrane in the steady state. (a) Grain size λ = 18 μm; (b) Grain size λ= 120 nm.

It can be seen that the average concentration deviates from the linear assumption. This deviation is more important for nanoscale membrane (Fig. 87b). This means that the magnitude of this discrepancy depends on the grain size and thus on the intergranular volume fraction. It seems that the membrane behaves as a heterogeneous composite.

To explore this point, we analyzed the local concentration by plotting line profiles concentration at the grain scale in different regions of the membrane with grain size λ=120 nm (50 different zones were explored). Two typical line profiles concentration were detected, as depicted in Fig. 88, depending on the grain-boundary type: a gap of concentration between the two grains can be observed at special boundaries, while for random boundaries the evolution is less abrupt. This means that the RGBs favor the homogenization of the local concentration unlike the SGBs.

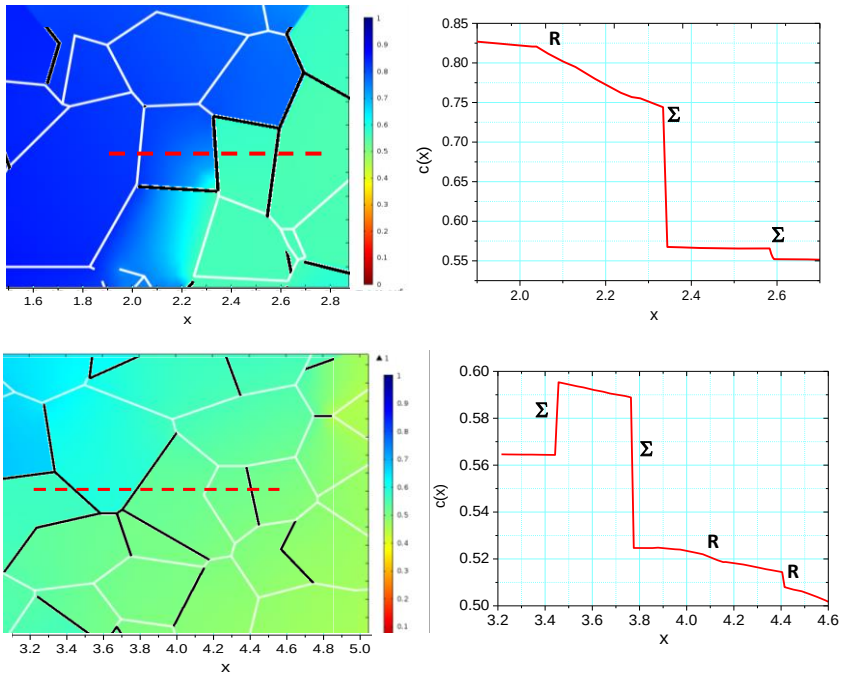

Fig. 88 - Line profiles concentration at the grain scale

One can note also that the magnitude of the gap in the concentration at SGBs is depending on the neighboring environment (its boundary conditions). When a SGB is separating two regions of high and low RGB clustering, the difference in concentrations of both sides of the SGB is very important. This situation is as a result of the clustering of random boundaries and their role in the transient diffusion. As shown in Fig. 89a, the hydrogen diffusion occurs primarily along RGBs, for very short times. Then, the diffusion leaks to the grains surrounding these random boundaries (Fig. 89b) and at the end the hydrogen diffuses across the special boundaries from the neighboring grains. Thus in the regions of low clustering of RGBs, the diffusion is delayed either by the SGB clusters or the large size grains. As a result, at steady state, the diffusion front is more or less advanced depending of the RGB clustering.

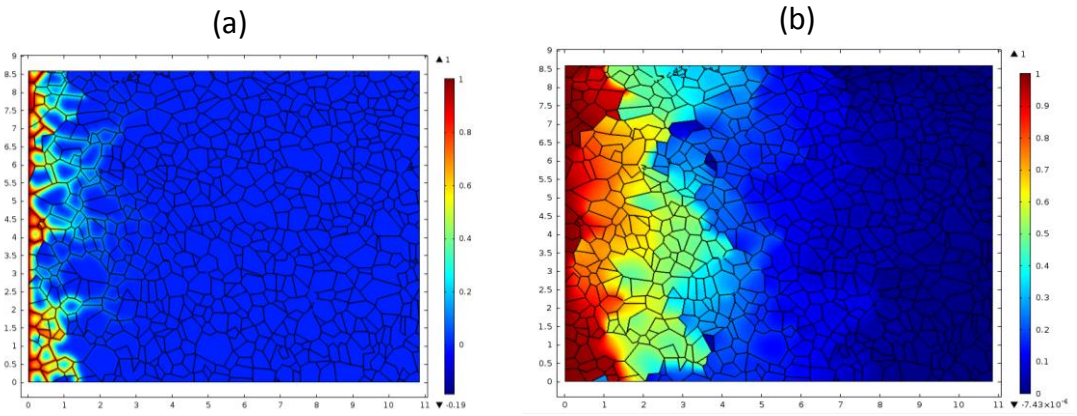

Fig. 89 – Surface profile concentration for different diffusion time t: (a) t = 0.08 s and (b) t = 2 s.

5. Discussion on the implications of trapping at GBs on the hydrogen diffusion

We have seen in the previous section that the GB network topology can lead to local heterogeneities of the H concentration. However, considering a slower H diffusivity in the GB is not sufficient to model all the implications of grain boundaries on the hydrogen transport in polycrystals. Indeed, there are different H-interactions with GBs, depending on the atomistic GB structure and the diffusion configuration. The boundary can enhance or reduce the hydrogen diffusion, but it can also attract hydrogen into its cavity or vicinity (segregation). Studies report also that GBs can act as an energy barrier to the hydrogen diffusion **[Pedersen 2009, Di Stefano 2015]**. In a thermodynamically point of view, these different situations can be described in terms of potential energies, as shown in Fig. 90.

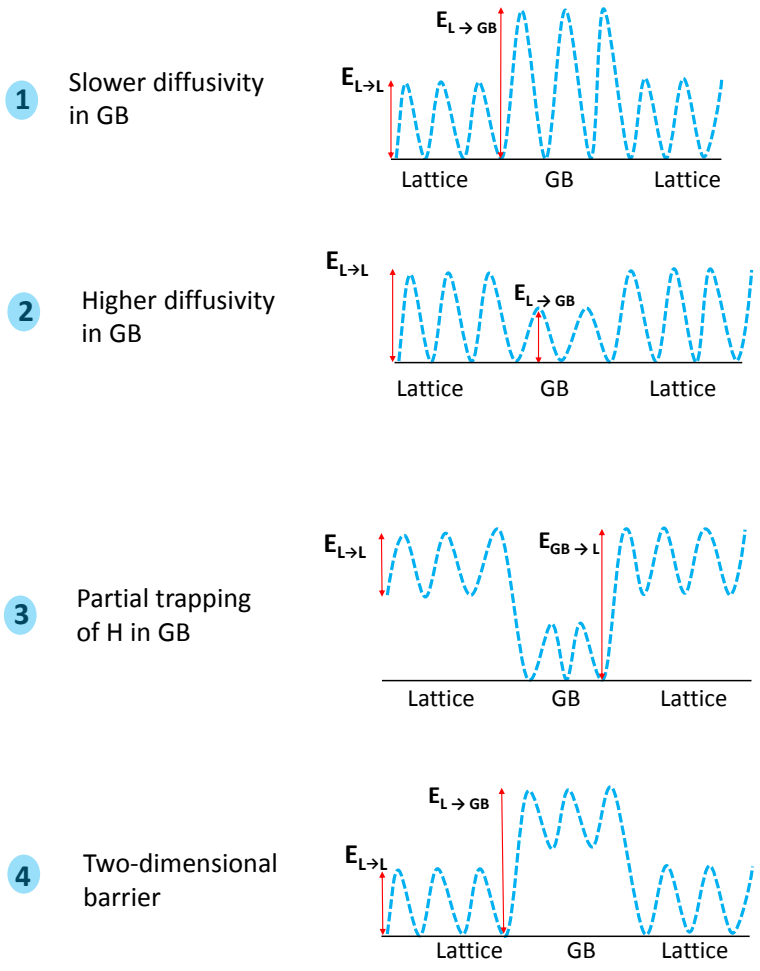

Fig. 90- Different cases energy barrier between the lattice and the grain-boundary, $E_{L\rightarrow L}$ is the activation energy of lattice diffusion. $E_{L\rightarrow GB}$ is the activation energy for moving from a lattice site to a GB site, while $E_{GB\rightarrow L}$ is the activation energy for the inverse case.

In our numerical approach, we only considered the two first situations (Fig. 90) by taking into account both higher and smaller GB diffusivities than lattice. It can be noted that the slower diffusivity

case is equivalent to an energy barrier when the atoms diffuses across the boundary. Thus, we think that the two-dimensional barrier situation is considered in our study. Therefore, the omitted situation in our approach is the segregation of hydrogen to GBs (Situation 3 in Fig.). In addition to delay the H transport, the H segregation to GBs affects particularly H-distribution in the material, at steady state.

In the classical models of diffusion in polycrystals **[Mehrer 2007]**, the GB segregation effect is taken into account by imposing the following boundary condition between the lattice and the GB:

$$c_{gb}(x,y,t) = sc(x,y,t) \tag{IV.2}$$

where *s* is an equilibrium segregation factor. As mentioned in the first chapter, in this approach, a local equilibrium is assumed between the atoms in the GBs and those in the adjacent grains. In other words, the H-concentration in the grains is not affected by the trapping. Recently Knyazeva *et al*. **[Knyazeva 2015]**investigated the effect of the segregation factor on the effective diffusion, using phenomenological equation inspired from the Maxwell-Garnet approximations. In their approach, they compared the predictions of their equation with experimental data of Oudriss *et al*. **[Oudriss 2012b]**, as shown in Fig. 91.

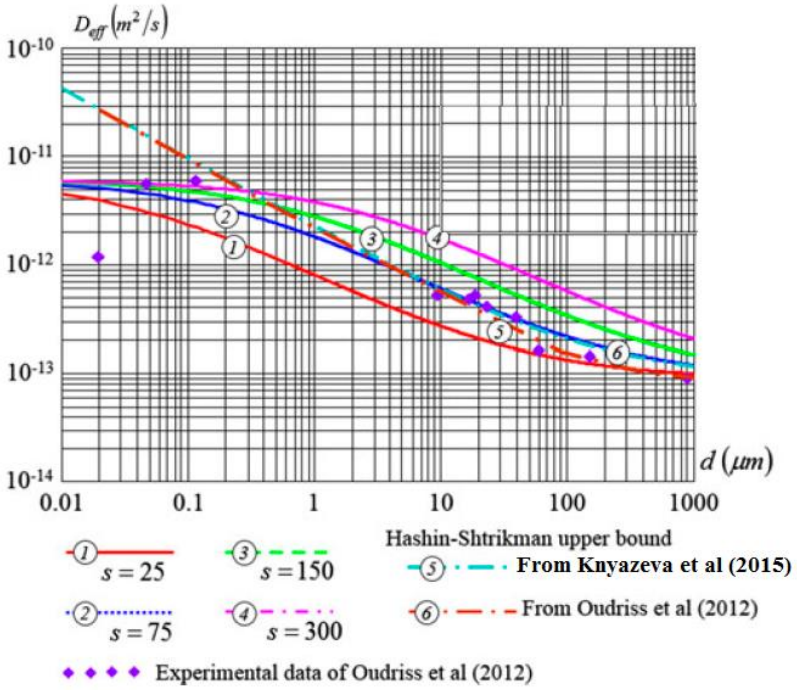

Fig. 91- Comparison of the predictions of the phenomenological equation accounting of a segregation factor with experimental data of **[Oudriss 2012b] [Knyazeva 2015]**

According to their results, a segregation factor s = 75 gives a relative good approximation of the experimental data. However, in this kind of approach, the using of a constant segregation factor for all the grain boundaries is questionable because of the variety of grain boundaries. In addition, this does

not allow to describe the segregation kinetics because of the assumed equilibrium state. Therefore, this kind of approach can result in controversial interpretations of the experimental data.

A realistic description of the hydrogen segregation effects on the hydrogen diffusion process in the materials requires the consideration of the GB segregation kinetics as a function of the grain-boundary character. However, due to the anisotropy and structure dependence of segregation at GB, a detailed description of the hydrogen segregation at GBs should be based on atomistic calculations **[Lejcek 2010]**. Recently, Ilin **[Ilin 2014]**, as a part of his doctoral thesis, investigated the segregation barrier effect on the hydrogen diffusion, using one dimensional atomic layer model based on jump probabilities. However, the approach adopted in its work remains very local and complex to implement in large system with higher dimensions.

Simulating the segregation behavior of each individual boundary is complex because of the huge number of grain boundaries that differ in their segregation behavior. Therefore, a binary classification of the GBs depending on their segregation behavior, the same approach as the diffusion property in the present work, could be an alternative to study the diffusion in a polycrystal, as suggested by Hofmann **[Hofmann 1996]**.

It is for this purpose that we conducted an experimental study combining microstructure characterization and local concentration profiling performed on the same materials in order to gain insights the effects of the GBs on the local hydrogen segregation.

II. Experimental analysis of hydrogen segregation effects on the hydrogen distribution near grain boundaries

1. Introduction

If the court-circuit diffusion of GBs can be taken into account in the numerical diffusion models by using a diffusion parameter, it is more difficult for the trapping phenomena. As underlined in the first chapter, grain boundaries can contain a wide variety of trap sites, leading to a broad spectrum of segregation energies **[Moody 1991, Kirchheim 1993]**. In addition to reducing the apparent GB diffusivity, the hydrogen trapping at GBs leads to an increase of the local hydrogen solubility and promotes local oversaturation phenomenon **[Coudreuse 2000]**. The hydrogen trapping at GBs can also affect the hydrogen diffusion and concentration near GBs, as suggested by some numerical works **[Pedersen 2009]**. The few experimental studies on the subject indicated also the presence of a gradient of hydrogen concentration near GBs **[Fukushima 1982, Ladna 1987a]**. Moreover, using microprint technics **[Katano 2001, Ohmisawa 2003]** and/or high-resolution tritium

autoradiography **[Aucouturier 1982]**, it was clearly established a segregation of hydrogen near some GBs but not for all the GBs considered **[Aucouturier 1982]**. These results suggest a specific behavior that depends on grain boundaries character. Birnbaum and co-worker **[Birnbaum 1988]** suspected this specificity long time ago and tried to prove it using SIMS analyses on some GBs of polycrystals and bi-crystals. These analyses clearly demonstrate for some selected GBs a gradient of hydrogen content with a length path higher than the GBs thickness. But the lack of statistical analyze has made it difficult to determine the hydrogen distribution and trapping contribution around GBs.

The present experimental study is aimed at providing qualitative and statistical view on the dependence of the hydrogen trapping around GBs with the GB character. To do that, combined EBSD and SIMS analyses were performed on polycrystalline Ni. First, the experimental procedure is presented. Then, the results of the hydrogen local distribution around GBs are discussed as a function of the grain-boundary type.

2. Experimental procedure

This study was conducted in three phases. As first step, the crystallographic orientation of the samples was characterized, using EBSD. Afterwards, the samples were charged with hydrogen, except the control sample. After the charging step, SIMS measurements were performed to characterize the hydrogen local distribution on the samples surface.

2.1. Microstructural characterization and hydrogen charging

The material used was polycrystalline nickel (purity 99.99%) with different grain sizes 45 μm and 18 μm. In order to characterize the grain-boundary character distribution by EBSD mapping, the same procedure as in the first section (I.2.1) were used here. The grain boundary character distribution (GBCD) was investigated using crystallographic orientation mapping data as previously described in the first section.

After the characterization step, hydrogen were introduced into the samples, at room temperature (298 K) for 48 hours by electrochemical charging at a cathodic current density of -20 mA/cm^2 in a 0.1 M NaOH (pH =13) aqueous solution, deaerated with an argon pressure of 1.4 bar. After the charging, the initial hydrogen concentration was respectively equal to 540 ppm at. and 360 ppm at. for grains sizes of 18 μm and 45 μm. These concentrations are higher than the hydrogen solubility (6.8 ppm at for 0.1MPa and 300K) reported for nickel single crystal at room temperature **[Fukai 2006]**. This difference can be explained by the fact that equivalent pressure corresponding to the cathodic charging was higher than 0.1 MPa, but also the fact that some GBs can promote the hydrogen trapping processes.

The different samples were analyzed by using secondary ion mass spectroscopy, after a specific backing time in room temperature, in order to investigate the hydrogen surface distribution.

2.2. Secondary ion mass spectroscopy (SIMS) analysis

This part of the study was done in the framework of a research internship of a master student, i.e., Ms. Solenne LEGERNNIC, in cooperation with the Pacific Northwest National Laboratory (PNNL) in Richland (US).

SIMS technique provides the best sensitivity and depth resolution to track hydrogen in materials. This technic consists in sputtering the specimen surface with a focused primary ion beam and detecting the secondary ions subsequently ejected. A more detailed description of this technic is provided in Appendix D. Note that the performance and the reliability of this technique depend mainly on the experimental settings. The optimal experimental settings used in this study have been previously established by Zhu et al. **[Zhu 2012b]**.

Entire hydrogen mappings were performed using time-of-flight SIMS measurements (TOF.SIMS5, ION-TOF GmbH, Germany). Samples were pumped down in the introduction chamber 12 hours before they were introduced into the analysis chamber. The pressure in the analysis chamber was about 3.4×10^{-9} mbar. For each zones studied, the sputtering primary ion was a 1.0 keV Cs^+ beam, which was rastered over a 300×300 μm^2 area during sputtering. A pulsed 25 keV Bi^+ beam was used for analysis, which was rastered over a 100×100 μm^2 area at the center of the Cs^+ sputter craters during data acquisition. The pulse frequency of the Bi^+ beam was 33 kHz and the corresponding current was about 3.8 pA. The H^- ions were detected because the H^- signal is more sensitive than the H^+ signal **[Zhu 2012a, Zhu 2012b]**. After the SIMS measurements, the samples were removed from the vacuum, and the depths of sputter craters were measured using a stylus profilometer (Dektak 150, Veeco Instruments, Inc.). A constant sputtering rate was assumed for each depth profiling measurements. The depth of sputter craters was intentionally controlled to be around 270±20 nm. The first 80 nm is not taken into account to the summation of hydrogen content used to present a mapping of solute distribution.

3. Hydrogen local distribution

The correlation of the corresponding mappings of SEM-EBSD analysis and ToF-SIMS analysis are illustrated on Fig. 92a. A typical mapping of solute content (SIMS data) and corresponding grain orientations and grain boundaries orientations (EBSD data) is shown in Fig. 92b.

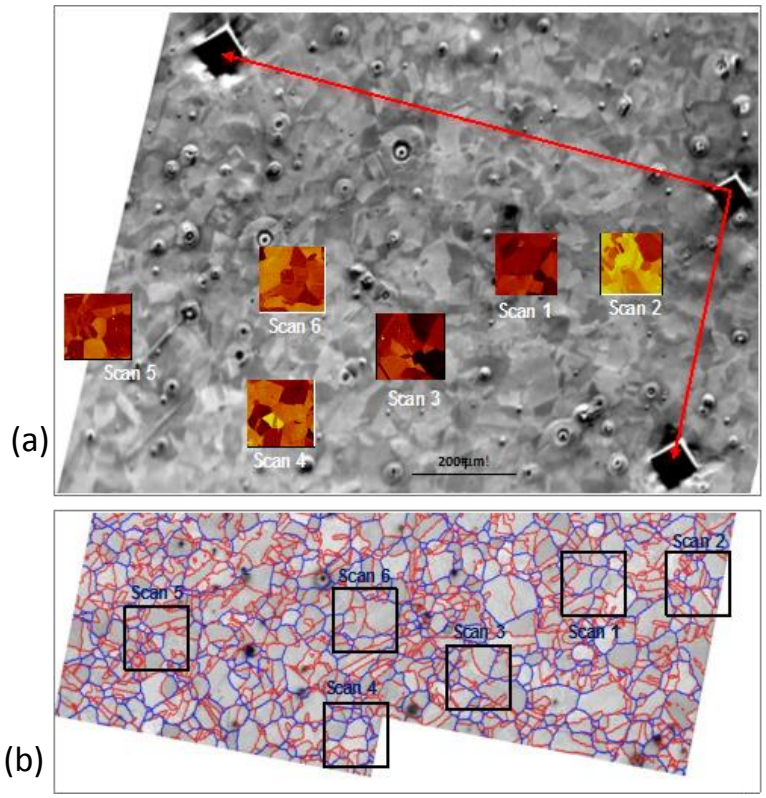

Fig. 92 – SEM (a) and EBSD (b) maps with the six SIMS maps locations on both maps.

For the six scans illustrated in Fig. 92, each grain is well distinguished by $^{58}Ni^-$ counts (Fig. 93a), $^{1}H^-$ (Fig. 93b) counts and H/Ni ratio (Fig. 93c). Consequently these maps can be easily correlated with EBSD data (grain orientation: Fig. 93d and grain boundaries orientation: Fig. 93e). As it was previously suggested, the number of counts per second is affected by the grain orientation of the studied crystal face. To minimize these effects, the data was normalized using $^{58}Ni^-$.

The hydrogen distribution appears to be influenced by the grain orientations, which illustrates that boundary conditions of one grain (grain-boundaries) affect the redistribution of hydrogen. To illustrate this point, we represent in Fig. 94 the normalized H^- signal intensity along a line that intersects different grain orientations and grain boundaries. Using EBSD data, grain boundaries have been identified as special grains boundaries ($\Sigma 3^n$) or random grains boundaries (R). It can be seen in Fig. 94b that hydrogen concentration is affected when crossing grain-boundaries. Different situations near GBs are observed, which imposes a statistical approach to characterize the profile of hydrogen around grain-boundaries. The profile of hydrogen around GBs has been investigated qualitatively in relation with the type of GBs for 50 grains boundaries for both grain sizes.

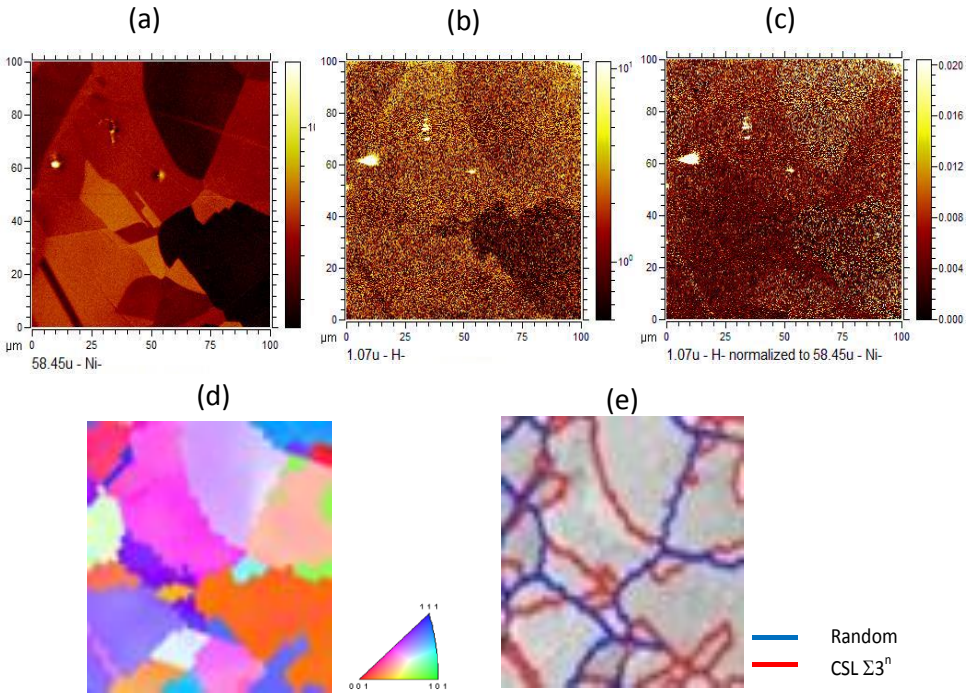

Fig. 93 - : Signal intensity for $^{58}Ni^-$ (a), $^{1}H^-$ (b) and the ratio $^{1}H^-/^{58}Ni^-$ (c). Mapping of grains orientations (d) and grain boundaries families (e). Sample with grain size of 45 µm, scan number 3

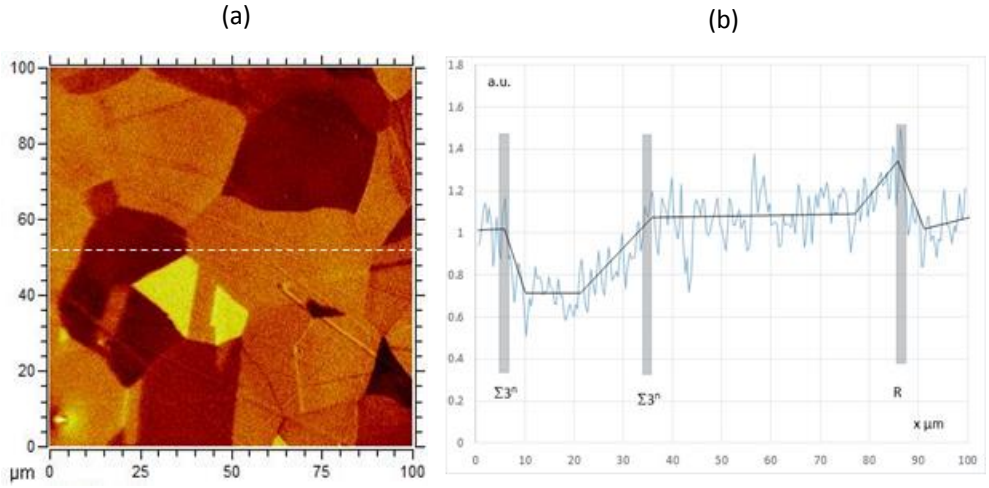

Fig. 94 - Line profile position (a) and normalized $^{1}H^-$ signal intensity versus the position along the line. Sample with grain size of 45 µm, scan number 4, line 4.

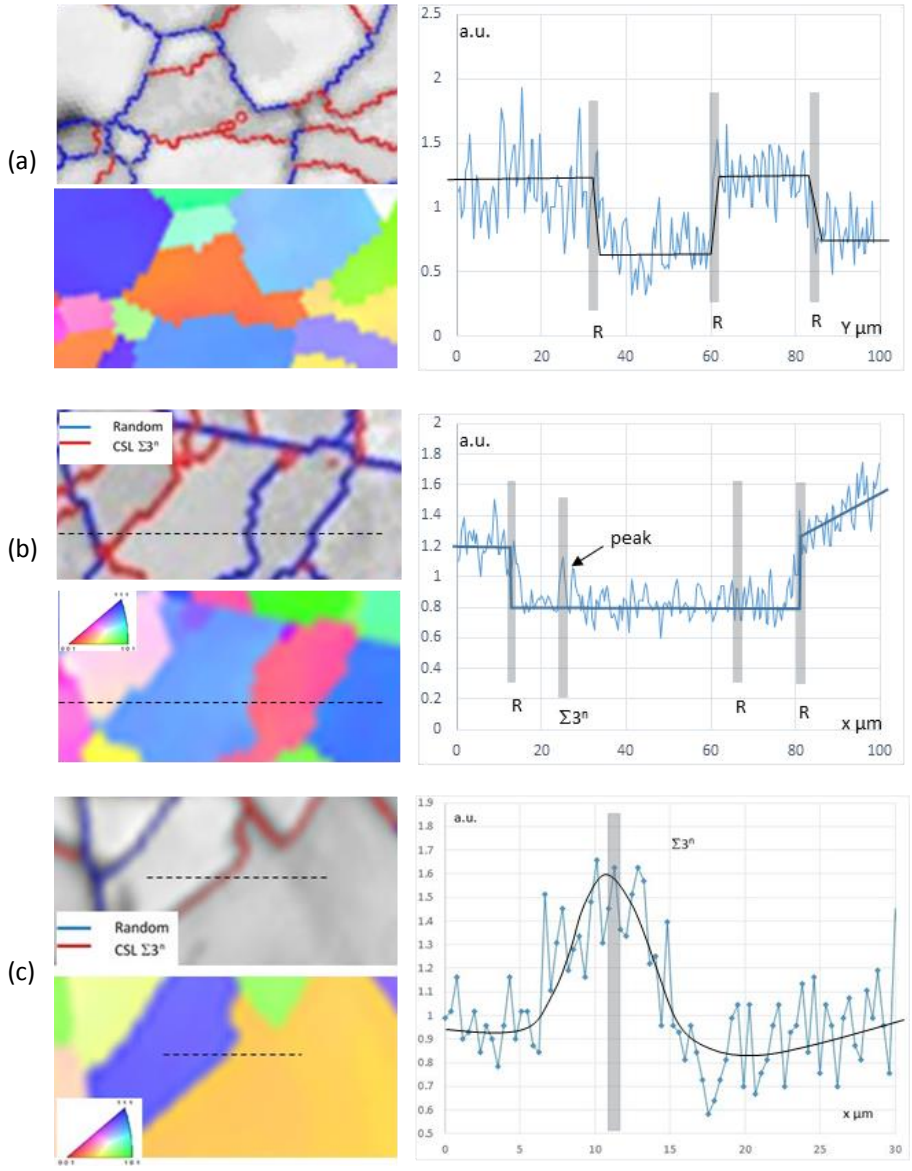

Fig. 95 - Some examples of possible correlation between EBSD and SIMS analyses.

As illustrated on Fig. 95, four kinds of profiles can be reported:

- a gap where instantaneous variation of hydrogen content is observed when we cross the GB,
- a constant profile where no significant modification of hydrogen content is related to both grains around GB,
- a break where the profile evolved crossing a GB,
- a gradient of hydrogen content for both sides of GB.

Around a large fraction of random grain-boundaries, we observed a gap of hydrogen concentration between both adjacent grains, as shown in Fig. 96a. In contrast for the special grain-boundaries, a gradient of hydrogen content on both sides of GB is the main feature observed (Fig. 96b).

It has been reported that random GBs mainly constitute fast diffusivity paths for hydrogen diffusion in relation with a large excess of free volume **[Oudriss 2012b]**. Consequently, it seems that when this process occurs along GBs, hydrogen does not cross the GB easily. In contrast to the numerical results in the first part, the random GBs do not seem to favor hydrogen homogenization grain to grain. In addition, hydrogen distribution supports the idea that random GBs accommodate hydrogen more easily than others ones and provide diffusion pathways that can determine the preferred direction of hydrogen diffusion along GBs. Oudriss *et al*. have suggested a direct correlation between the excess of volume in GBs and an accelerated H diffusion along GBs (short-circuit of diffusion) **[Oudriss 2012b]**. More recently, DFT calculations conducted by Di Stephano *et al*. in nickel, highlighted higher hydrogen diffusivity along a Σ5 GB in relation with an important excess volume **[Di Stefano 2015]**. Consequently both results seem to support the interpretation of the specific hydrogen distribution (gap) observed in the present work.

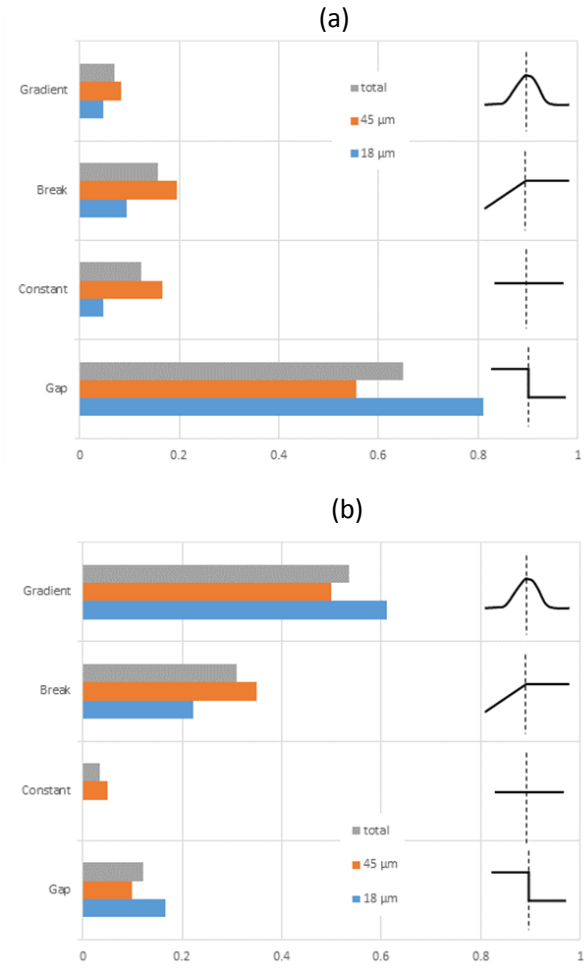

Fig. 96 - Fraction of grain-boundaries, which present one kind of hydrogen distribution. (a) random GBs and (b) $\Sigma 3^n$ GBs

Despite the large variety of special $\Sigma3^n$, hydrogen gradient around these GBs, suggests that in polycrystalline structures, a strain gradient exists near the $\Sigma3^n$ GBs with a path length (4 µm) significantly higher than GB thickness (≈2 to 5 nm). This should be noted as a surprise, because a large density of defects is necessary to accommodate the misorientation between two adjacent grain-boundaries. An elastic field was identified for some cases around GBs with HRTEM **[Zhao 2008]**. Additionally, it has been reported previously that hydrogen is deeply trapped in $\Sigma3^n$ GBs **[Oudriss 2012b]**, but also that this type of GBs is a specific location where reverse trapping occurs in relation with the long-range elastic field of dislocation networks **[Oudriss 2012b]**.

Twin boundaries are a specific configuration of Σ3, where no defects are necessary to accommodate the misorientation. In this case, we do not observe a gradient profile (Fig. 97) and the concentration of hydrogen is lower than the one obtained in the grain. Consequently, this close-packed grain boundary configuration acts as a two-dimensional barrier to hydrogen diffusion, consistent with the DFT studies **[Du 2011, Di Stefano 2015]**. According to recent DFT calculations **[Di Stefano 2015]** performed on Σ3 symmetric twin GB in nickel, the segregation energy is negligible for this GB. The diffusion parallel to the GB plane is equal to its diffusion in the grain interior but the diffusion across the GB plane seems to be associated with a significantly higher barrier. Therefore, it is surprising to observe a low concentration of hydrogen in a twin and no segregation. In opposite, to our knowledge, there are no DFT results about more defective $\Sigma3^n$ GBs.

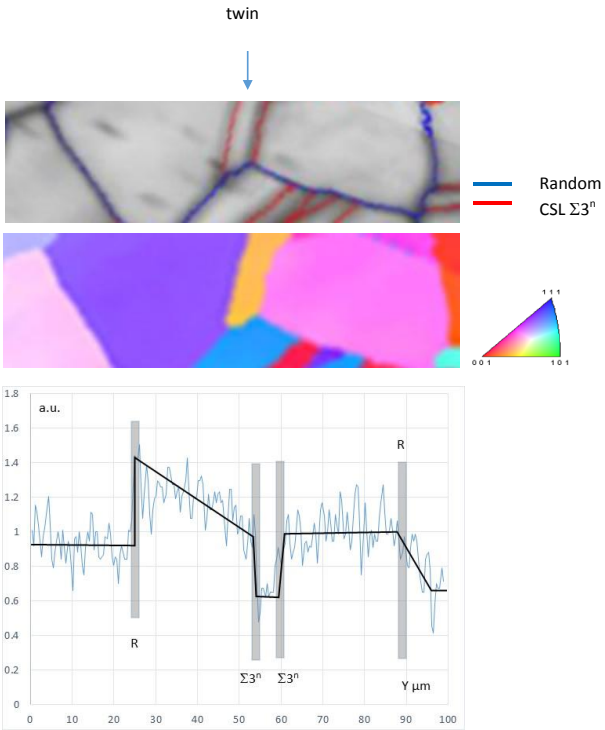

Fig. 97 – Hydrogen distribution around a twin.

Compared to our numerical results, the experimental findings show a wide variety of the GB effects on the hydrogen local distribution in polycrystalline materials. The profiles of concentration around GBs, observed in the experimental analysis, are completely different from the observation of the numerical results. For instance, the gap of concentration detected around random GBs, was observed around special GBs in the numerical study. However, this is not surprising because, even though detailed information on the microstructure was considered in our numerical model, several other considerations were missing such as the segregation effect or the barrier effect of some boundaries. As underlined in this experimental work, strain fields around GBs can also alter the hydrogen distribution. In addition, at high H concentrations, probable chemical interactions (H-H interactions or hydride formation) can impact the H local distribution in polycrystalline materials.

This point emphasizes the necessity to incorporate more ingredients in order to capture the effects of GBs on the hydrogen concentration in a multi-scale modeling. However, it is a challenging task to fully understand the coupled effects of both GB connectivity and segregation behavior associated with each type of grain boundary on the macroscopic diffusivity and concentration distribution.

III. Concluding remarks

This chapter was composed of two main parts. In the first part, we investigated the GB connectivity effects on the effective diffusivity in realistic microstructures, using EBSD-based Fem models. Secondly, SIMS analysis combined with microstructure characterization was performed to analysis hydrogen segregation near grain boundaries.

- *In the first part, we showed the necessity of considering microstructural constraints in order to model appropriately the correlation between the GB connectivity and the effective diffusivity. By comparing the simulation results with the experimental data; we reported evidences of the highly connected random boundaries on the effective diffusivity. Finally, we analyzed the local hydrogen distribution at the steady state and concluded the limitation of the model to capture a realistic local hydrogen distribution.*

- *In the second part, the SIMS investigations allowed us to gain insights about the dependence of the hydrogen segregation near grain boundaries with the type of grain boundary. After qualitative and statistical analysis of the hydrogen local profiles around grain boundaries, two main situations were observed for hydrogen in relation with the GB category (random or CSL $\Sigma 3^n$). A gap for hydrogen concentration was mainly detected near random boundaries. In opposite, a gradient of hydrogen was observed near most of special $\Sigma 3^n$ boundaries. This result evidences the significant impact of grain- boundary character on the hydrogen distribution.*

Chapter 5

Conclusions & Prospects

I. Conclusions

The determination of reliable quantitative data on the hydrogen diffusion and concentration is an essential step in every HE mechanism. Many studies have been focused on the hydrogen diffusion in polycrystalline materials. In most of these studies, the intergranular region is considered as a homogeneous phase. However, it is known that grain boundaries are characterized by a variety of diffusion properties depending on their nature. Thus considering the effects of grain boundaries heterogeneity is crucial in the analysis of hydrogen diffusion in polycrystals. The aim of this thesis was twofold. The first and the main goal was to investigate the implications of heterogeneous GB networks on the hydrogen effective diffusivity in polycrystalline materials, using a numerical approach. The second goal was to understand the GB effects on the hydrogen local concentration, using experimental analysis.

In the numerical part, two approaches were considered. The first one consisted in working on idealized microstructures models, where the grain boundaries were randomly classified into two categories: random (RGBs) and special (SGBs) boundaries, with two different diffusivities. The second approach consisted in using EBSD-based microstructures, where the binary classification of grain boundaries was based on EBSD data. The main results with the two approaches are summarized as follows.

- *Using the first numerical approach*

To investigate the effects of the GB networks on the effectivity diffusivity, we have developed FEM models to simulate permeation tests in 2-D and 3D simplified polycrystalline aggregates. Several aspects of the correlations between the GB networks topology and the effective diffusivity were analyzed.

First, we showed, by characterizing the RGB connectivity in the 2-D hexagonal model, that there are different types of RGB networks with different morphology and connectivity depending on the fraction of random boundaries. Then the results on the evolution of the effective diffusivity evidenced clear correlations between the different types of networks and the different regimes of the diffusion. The analysis of the correlations between the connectivity parameters and the effective diffusivity allowed to determine in which interval of RGB fractions the effective diffusivity is strongly affected by the RGB connectivity. This interval corresponds to the RGB percolation transition zone and is characterized by the presence of large clusters. Moreover, it was found that the maximum rate of increase of D_{eff} was corresponding to the geometrical percolation threshold of the RGB networks. In addition, our results indicated that the correlations between the effective diffusivity and the GB connectivity were more significant for nanocrystalline aggregates than for sub-micron aggregates.

We also analyzed the problem as a continuum percolation by proposing a deductive approach combining the generalized effective medium theory (GEM) and the upper Hashin-Strikman (HS^{+}) to

approximate the effective diffusivity. This approach allowed determining the percolation threshold and the critical exponents of the effective diffusivity in 2-D and 3-D. Using this approach, we showed that the effects of the GB networks connectivity on the effective diffusivity is higher in 3-D than in 2-D.

This first study was based on a specific case where a random distribution of the grain-boundary character was considered. In real polycrystals, the boundary type is correlated to the neighboring environment.

- *Using the second numerical approach*

To investigate the connections between the constrained GB networks and the effective diffusivity, H-permeation tests were simulated using 2-D EBSD-based aggregates based on polycrystalline Ni. This allowed to consider both realistic grain microstructure morphology and grain-boundary characters distribution. By comparing the results of RGB connectivity to those of the first approach, we showed the important effects of the microstructural constraints on the GB connectivity. We also evidenced that the fractions of triples junctions of different type are a more accurate indicator of the GB connectivity than the fractions of random (or special boundaries), confirming the findings in the literature. In addition, the results on the effective diffusivity as a function of the grain sizes revealed slight differences with the experimental data, but nevertheless followed the same trend. We believe that this approach, with more ingredients, could be used to model realistic macroscopic diffusion in polycrystals, by heterogeneous GB networks.

In the experimental part of the thesis, SIMS measurements combined with EBSD characterization were performed to study the effects of GBs on hydrogen concentration distribution. These investigations allowed us to gain insights about the dependence of the hydrogen segregation near grain boundaries with the type of grain boundary. After qualitative and statistical analysis of the hydrogen local profiles around grain boundaries, two main situations were observed for hydrogen in relation with the GB category (random or CSL $\Sigma 3^n$). A gap for hydrogen concentration was mainly detected near random boundaries. In opposite, a gradient of hydrogen was observed near most of special $\Sigma 3^n$ boundaries. This result evidences the significant impact of grain-boundary character on the hydrogen distribution. However, no correlation had been made with the numerical results, which suggests a strong effect of the segregation on hydrogen concentration.

The approaches and the results presented in this thesis contribute significantly to the understanding of hydrogen diffusion in polycrystalline materials. The grain-boundary connectivity is neglected in most studies dealing with the diffusion in polycrystalline materials. Our results provide key insights on the connection between the grain-boundary connectivity and the overall diffusivity of the polycrystals. The numerical approach may be enriched by integrating more physics such as hydrogen segregation at GBs and may help to the good interpretation of the experimental data on the hydrogen diffusion and segregation.

This thesis also discussed the complexity of considering all the GB effects on the hydrogen transport process in materials. Possible improvements of the numerical approach in order to have a better description of the diffusion and the segregation in polycrystals are proposed in the following section.

II. Prospects

1. Improving the microstructure modeling

As highlighted in the third chapter, it is necessary to consider both grain-boundary and triple junction character distribution in order to develop appropriate model of diffusion in polycrystals. In the last chapter, studies were conducted on two-dimensional reconstructed boundaries. This approach should be extended in three dimensions in order to get more 3-D realistic microstructures. Serial-sectioning technique coupled with EBSD mapping is a developing technique that allow the 3-D reconstruction of microstructures **[Groeber 2008]**. This technique consists in putting together the information obtained from the 2-D sections to reconstruct 3-D topological structures. To perform the serial sectioning of the specimen, one can use focused ion beam (FIB) or other edging methods. As a part of this present PhD thesis, we have already started the 3-D reconstruction of microstructures by using EBSD and electro-polishing as etching method. The study is aimed at developing 3-D EBSD-based numerical diffusion models with a realistic grain-boundary and triple junctions network. An intermediate result is shown in Fig. 98. The development of FEM model was not fully completed due to limited resolution of the length scales intrinsic to the chosen methodology. Indeed, the 3-D microstructures obtained digitized 2-D images are characterized by a limited resolution at submicron scale **[Li 2011]**. Therefore, it is nearly impossible with this method to obtain a detailed description of 3-D topological entities for nanocrystalline materials.

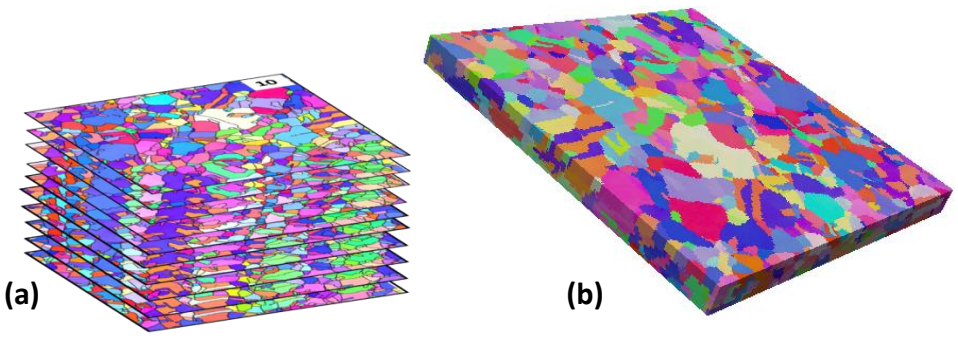

Fig. 98 – (a) Serial EBSD mapping of a nickel polycrystalline sample, (b) 3-D digitized microstructures obtained from the EBSD mapping. The 3-D reconstruction was performed with the software DREAM-3D

Nevertheless, the information from the serial-scanning techniques should be used to develop close-to-reality microstructures using Voronoi tessellation and inverse Monte Carlo simulation **[Xu 2009]**. Once realistic 3-D microstructures are developed, the next step would be to consider more physics.

2. Improving the applied physics

In our FEM models, we only considered the diffusion properties of grain boundaries. However, as discussed previously, hydrogen segregation at GBs can also alter the diffusion process by decreasing the effective diffusivity and leading to heterogeneous H-distribution. Therefore, hydrogen segregation at GB should be added to the diffusion model by defining two subsets of grain boundaries depending on their segregation behavior. In order to obtain realistic distribution of the segregation behavior of grain boundaries, high resolution visualization methods, such as 3-D atom probe tomography **[Cheng 2013]**, should be combined 3-D EBSD characterization. Information from atomistic calculations (DFT, kinetic Monte Carlo) should be also used to get accurate classification of grain boundaries.

The anisotropy of hydrogen diffusion is another important topic. Different atomistic studies have pointed out differences of diffusion rate between the diffusion across and parallel to the grain-boundary plane **[Suzuki 2004, Pedersen 2009, Di Stefano 2015]**. It would be interesting to investigate also the effects of the hydrogen diffusion anisotropy on the effective diffusivity in the polycrystalline materials, by considering different GB diffusivities in the parallel and perpendicular directions to the boundaries.

3. Towards a multi-physics modeling of hydrogen induced intergranular fracture

The present work is a part of large project which is aimed at helping to understand the role of the hydrogen diffusion and segregation in the HE mechanisms. In the present work, we focused mainly on the correlations between grain-boundary connectivity and the macroscopic diffusivity. The good estimation of the macroscopic diffusivity is important in the HE mechanisms, because it allows to estimate the necessary time for the hydrogen to reach regions of weak cohesion like grain boundaries.

In addition to the hydrogen diffusion rate, the local H concentration is a critical factor in decohesion mechanisms **[Lassila 1986]**. This local critical concentration has been found to be correlated with grain-boundary character **[Bechtle 2009]**. Moreover, Oudriss *et al.***[Oudriss 2014]** associated the increase of the fraction random boundaries with a loss of ductility in quasi-pure Nickel, as illustrated in Fig. 99.

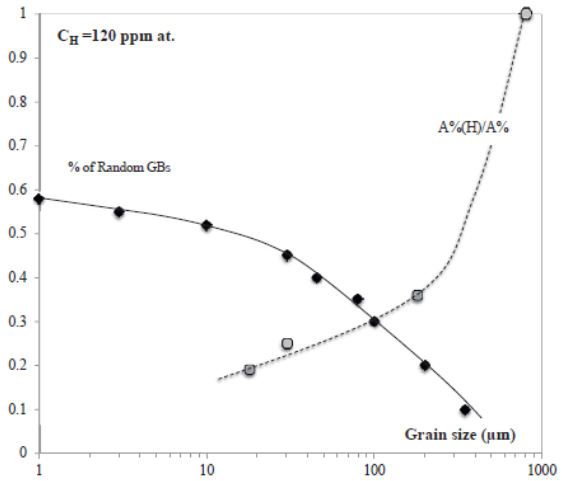

Fig. 99- The fraction of the random GBs and the ductility ratio A%(H) / A% *versus* the grain size [Oudriss 2014]

According to the authors, two different HE mechanisms (HEDE: Hydrogen-Enhanced-Decohesion, SAV: Super-Abundant Vacancies) are supposed to explain the decrease of the ductility depending on the H concentrations. However, in the same study, it is suggested that hydrogen flux promotes intergranular fracture more than the hydrogen concentration. Further studies are necessary to make clearer on this complex problem of induced intergranular fracture.

It is important to mention that the effects of the hydrogen depend on many parameters such as the hydrogen distribution, the grain-boundary character, the grain size and the mechanical history, etc., and the embrittlement of the interfaces can results from a combination of different mechanisms. There is therefore a need of a more generalized understanding of the hydrogen induced fracture. In this spirit, Kirchhem **[Kirchheim 2007, Kirchheim 2010, Kirchheim 2015]** has recently introduced a novel concept describing solute–defect interactions in a thermodynamic framework, in order to discuss models explaining hydrogen embrittlement as caused by enhanced local plasticity or the enhancement of vacancy formation.

This kind of concept requires reliable quantitative data on the local concentration and microstructure defects. For that, it is necessary to understand the effects of the microstructure, but also of the deformation heterogeneities on the hydrogen diffusion and trapping process in the materials. In this perspective, an experimental apparatus to perform hydrogen permeation under tensile Stress has been developed in the LaSIE laboratory to investigate the effects of stress-strain states on the hydrogen diffusion and solubility **[Guedes 2014]**. In parallel, it would be interesting to develop a numerical model coupling mechanical behavior and hydrogen diffusion. This model should be based on realistic microstructures and taken into account the grain-boundary character distribution, the GB connectivity, the hydrogen segregation at GBs and the anisotropy of diffusion. The inputs of this

model should be coming from different methods (experimental and atomistic calculations), at different scale, as illustrated in Fig. 100. The ultimate goal is to define critical parameters of hydrogen induced fracture.

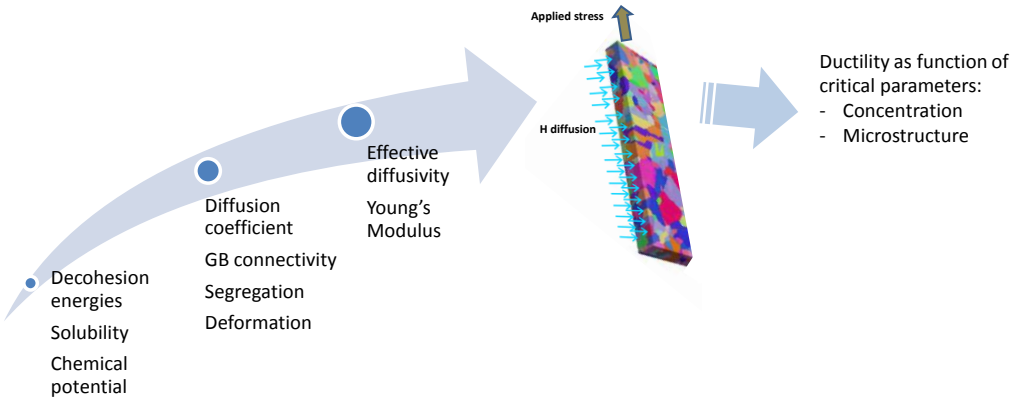

Fig. 100- Schematic description of a multi-physic model of hydrogen induced fracture

References

[Addach 2009] H. Addach, P. Berçot, M. Rezrazi and J. Takadoum, Corros. Sci. **51** (2), 263-267 (2009).

[Alexandreanu 2003] B. Alexandreanu, B.H. Sencer, V. Thaveeprungsriporn and G.S. Was, Acta Mater. **51** (13), 3831-3848 (2003).

[Altunoglu 1996] A.K. Altunoglu and N.S. Braithwaite, Metall. Mater.Trans. A **27** (9), 2495-2503 (1996).

[Arantes 1993] D.R. Arantes, X.Y. Huang, C. Marte and R. Kirchheim, Acta Metall. Mater. **41** (11), 3215-3222 (1993).

[Aucouturier 1982] M. Aucouturier, Le Journal de Physique Colloques **43** (C6), C6-175-C6-186 (1982).

[Auriault 2009] J.-L. Auriault, C. Boutin and C. Geindreau, *Homogénéisation de phénomènes couplés en milieux hétérogènes : Tome 1, Diffusion et dispersion* 2009).

[Balberg 1998] I. Balberg, Phys. Rev. B. **57** (21), 13351 (1998).

[Barnoush 2011] A. Barnoush, *Hydrogen embrittlement*. (2011).

[Basinger 2005] J.A. Basinger, E.R. Homer, D.T. Fullwood and B.L. Adams, Scripta Mater. **53** (8), 959-963 (2005).

[Beachem 1972] C.D. Beachem, Metall. Trans. **3** (2), 441-455 (1972).

[Bechtle 2009] S. Bechtle, M. Kumar, B.P. Somerday, M.E. Launey and R.O. Ritchie, Acta Mater. **57** (14), 4148-4157 (2009).

[Belova 2003] I.V. Belova and G.E. Murch, J Phys. Chem. Solids **64** (5), 873-878 (2003).

[Besenbacher 1990] F. Besenbacher, B.B. Nielsen, J.K. Nørskov, S.M. Myers and P. Nordlander, J. Fusion Energ. **9** (3), 257-261 (1990).

[Birnbaum 1997] H.K. Birnbaum, C. Buckley, F. Zeides, E. Sirois, P. Rozenak, S. Spooner and J.S. Lin, J. Alloy. Compd. **253–254** (0), 260-264 (1997).

[Birnbaum 1988] H.K. Birnbaum, B. Ladna and A. Kimura, J. Phys. Colloq. **49** (C5), C5-397-C5-401 (1988).

[Bokshtein 1958] B.S. Bokshtein, I.A. Magidson and I.A. Svetlov, Phys. Met. Metallogr. **6**, 81 (1958).

[Bokstein 2001] B. Bokstein, V. Ivanov, O. Oreshina, A. Peteline and S. Peteline, Mater. Sci. Eng. **302** (1), 151-153 (2001).

[Bonis 2002] M.R. Bonis and J.L. Crolet, (NACE International, 2002).

[Bouhattate 2011] J. Bouhattate, E. Legrand and X. Feaugas, Int. J. Hydrogen Energ. **36** (19), 12644-12652 (2011).

[Brandon 1966] D.G. Brandon, Acta Metall. **14**, 1479 (1966).

[Brass 2000] A.-M. Brass, J. Chêne and L. Coudreuse, Techniques de l'ingénieur. Corrosion vieillissement (M175), M175. 1-M175. 24 (2000).

[Brass 1996] A.M. Brass and A. Chanfreau, Acta Mater. **44** (9), 3823-3831 (1996).

[Brass 2006] A.M. Brass and J. Chêne, Corros. Sci. **48** (10), 3222-3242 (2006).

[Broadbent 1957] S.R. Broadbent, Hammersley, J. M., Proc. Cambridge Philos. Soc. **53**, 629-641 (1957).

[Budke 1996] E. Budke, Christian Herzig, S.I. Prokofjev, Lasar S. Shvindlerman, Mater. Sci. Forum **207-209**, 465-468 (1996).

[Burgers 1940] J. Burgers, P. Phys. Soc. **52** (1), 23 (1940).

[Carr 2004] N.Z. Carr and R.B. McLellan, Acta Mater. **52** (11), 3273-3293 (2004).

[Carr 2006] N.Z. Carr and R.B. McLellan, J Phys. Chem. Solids **67** (8), 1797-1802 (2006).

[Chanfreau 1992] A. Chanfreau, « Etude de la diffusion de l'hydrogène dans des matériaux chargés et non chargés en hélium, par la méthode de perméation électrochimique », PhD thesis, Université de Paris-Sud Centre d'Orsay, (1992).

[Chen 2008] Y. Chen, Percolation and Homogenization theories for Hetergeneous Materials, PhD thesis, Massachusestts Institute of Technology, (2008).

[Chen 2006] Y. Chen and C. Schuh, Acta Mater. **54** (18), 4709-4720 (2006).

[Chen 2007] Y. Chen and C.A. Schuh, J. Appl. Phys. **101** (6), - (2007).

[Chen 2009] Y. Chen and C.A. Schuh, Phys. Rev. E **80** (4), 040103 (2009).

[Chene 1982] J. Chene, presented at the Current Solutions to Hydrogen Problems in Steels, Washington DC, 1982 (unpublished).

[Cheng 2013] X. Cheng, Z. Zhang, W. Liu and X. Wang, Prog. Nat. Sci. **23** (4), 446-452 (2013).

[Cheng 2009] Y. Cheng, D. Weygand and P. Gumbsch, Comp. Mater. Sci. **45** (3), 783-787 (2009).

[Choo 1982] W.Y. Choo and J. Lee, Metall. Trans. A **13** (1), 135-140 (1982).

[Clerc 1983] J.P. Clerc, *La Percolation: modèles, simulations analogiques et numériques*. (Masson, 1983).

[Coudreuse 2000] L. Coudreuse, A.-M. Brass and J. Chêne, Techniques de l'ingénieur Corrosion et vieillissement: phénomènes et mécanismes **base documentaire : TIB371DUO** (ref. article : m176) (2000).

[Crank 1975] J. Crank, *The mathematics of diffusion / by J. Crank*. (Clarendon Press, Oxford [England], 1975).

[Crolet 2001a] J.L. Crolet and M. Bonis, (NACE International, 2001a).

[Crolet 2001b] J.L. Crolet and M.R. Bonis, (NACE International, 2001b).

[Darken 1949] L.S. Darken and R.P. Smith, Corrosion **5**, 1-16 (1949).

[Daw 1993] M.S. Daw, S.M. Foiles and M.I. Baskes, Mater. Sci. Rep. **9** (7–8), 251-310 (1993).

[Daynes 1920] H.A. Daynes, Proc. R. Soc. London Ser. A **97** (685), 286-307 (1920).

[Déchamps 1987] M. Déchamps, F. Baribier and A. Marrouche, Acta Metall. **35** (1), 101-107 (1987).

[Deng 2014] J. Deng, D. Morgan and I. Szlufarska, Comp. Mater. Sci. **93**, 36-45 (2014).

[Devanathan 1962] M.A.V. Devanathan and Z. Stachurski, Proc. R. Soc. London Ser. A **270** (1340), 90-102 (1962).

[Di Stefano 2015] D. Di Stefano, M. Mrovec and C. Elsässer, Acta Mater. **98**, 306-312 (2015).

[Doyle 1995] D.M. Doyle, G. Palumbo, K.T. Aust, A.M. El-Sherik and U. Erb, Acta Metall. Mater. **43** (8), 3027-3033 (1995).

[Du 2011] Y.A. Du, L. Ismer, J. Rogal, T. Hickel, J. Neugebauer and R. Drautz, Phys. Rev. B. **84** (14), 144121 (2011).

[Feaugas 2007] X. Feaugas and H. Haddou, Philos. Mag. **87** (7), 989-1018 (2007).

[Feng 2007] Z. Feng, L.M. Anovitz, P. Kironko, A. Duncan, T. Adams and P. Sofronis, presented at the DOE Hydrogen Pipeline Working Group Meeting 2007 (unpublished).

[Fisher 1951] J.C. Fisher, J. Appl. Phys. **22** (1), 74-77 (1951).

[Fortier 1995] P. Fortier, K.T. Aust and W.A. Miller, Acta Metall. Mater. **43** (1), 339-349 (1995).

[Fortier 1997] P. Fortier, W.A. Miller and K.T. Aust, Acta Mater. **45** (8), 3459-3467 (1997).

[Frappart 2011a] S. Frappart, « Des éléments de compréhension sur le mécanisme de transport et de ségrégation de l'hydrogène dans les aciers martensitiques trempés et revenus », PhD thesis, Université de la Rochelle, (2011a).

[Frappart 2010] S. Frappart, X. Feaugas, J. Creus, F. Thebault, L. Delattre and H. Marchebois, J Phys. Chem. Solids **71** (10), 1467-1479 (2010).

[Frappart 2011b] S. Frappart, A. Oudriss, X. Feaugas, J. Creus, J. Bouhattate, F. Thébault, . . . H. Marchebois, Scripta Mater. **65** (10), 859-862 (2011b).

[Frary 2005a] M. Frary and C.A. Schuh *, Philos. Mag. **85** (11), 1123-1143 (2005a).

[Frary 2005b] M. Frary and C. Schuh, Acta Mater. **53** (16), 4323-4335 (2005b).

[Frary 2004] M. Frary and C.A. Schuh, Phys. Rev. B. **69** (13), 134115 (2004).

[Fukai 1995] Y. Fukai, J. Alloy. Compd. **231** (1–2), 35-40 (1995).

[Fukai 2006] Y. Fukai, *The metal-hydrogen system: basic bulk properties*. (Springer Science & Business Media, 2006).

[Fukai 2001] Y. Fukai, Y. Shizuku and Y. Kurokawa, J. Alloy. Compd. **329** (1), 195-201 (2001).

[Fukushima 1982] H. Fukushima and H.K. Birnbaum, Scripta Metall. **16** (6), 753-757 (1982).

[Gahr 1977] S. Gahr, M.L. Grossbeck and H.K. Birnbaum, Acta Metall. **25** (2), 125-134 (1977).

[Gertsman 2001] V. Gertsman, Acta Crystallogr. A **57** (4), 369-377 (2001).

[Gertsman 1996] V.Y. Gertsman, M. Janecek and K. Tangri, Acta Mater. **44** (7), 2869-2882 (1996).

[Gertsman 1995] V.Y. Gertsman and K. Tangri, Scripta. Metall. Mater. **32** (10), 1649-1652 (1995).

[Gibbs 1966] G. Gibbs, physica status solidi (b) **16** (1), K27-K29 (1966).

[Godon 2010] A. Godon, Relations Structure/Composition/Propriétés de

revêtements électrodéposés de nickel de taille de grain

nanométrique, Université de La Rochelle, (2010).

[Grimmer 1974] H. Grimmer, W. Bollmann and D.H. Warrington, Acta Crystallogr. A **30** (2), 197-207 (1974).

[Groeber 2008] M. Groeber, S. Ghosh, M.D. Uchic and D.M. Dimiduk, Acta Mater. **56** (6), 1257-1273 (2008).

[Guedes 2014] D. Guedes, A. Oudriss, S. Frappart, G. Courlit, S. Cohendoz, P. Girault, . . . X. Feaugas, Scripta Mater. **84–85**, 23-26 (2014).

[Haddou 2003] H. Haddou, Influence de la taille de grain et de l'énergie de défaut d'empilement sur l'état de contraintes internes développé au cours de la déformation plastique en traction simple et en fatigue oligocyclique (alliages c.f.c), Université de Technologie de Compiègne, (2003).

[Harris 1991] T.M. Harris and M. Latanision, Metall. Trans. A **22** (2), 351-355 (1991).

[Harrison 1961] L.G. Harrison, Trans. Faraday Soc. **57** (0), 1191-1199 (1961).

[Hart 1957] E.W. Hart, Acta Metall. **5** (10), 597 (1957).

[Hashin 1963] Z. Hashin and S. Shtrikman, J. Mech. Phys. Solids **11** (2), 127-140 (1963).

[Hickel 2014] T. Hickel, R. Nazarov, E. McEniry, G. Leyson, B. Grabowski and J. Neugebauer, JOM **66** (8), 1399-1405 (2014).

[Hill 1965] R. Hill, J. Mech. Phys. Solids **13** (4), 213-222 (1965).

[Hirth 1980] J. Hirth, Metall. Trans. A **11** (6), 861-890 (1980).

[Hirth 1978] J. Hirth and B. Carnahan, Acta Metall. **26** (12), 1795-1803 (1978).

[Hoffman 1956] R.E. Hoffman, Acta Metall. **4** (1), 97-98 (1956).

[Hofmann 1996] S. Hofmann and P. Leiĉek, Interface Science **3** (4), 241-267 (1996).

[Horinouchi 2013] H. Horinouchi, M. Shinohara, T. Otsuka, K. Hashizume and T. Tanabe, J. Alloy. Compd. **580, Supplement 1** (0), S73-S75 (2013).

[Hoshen 1997] J. Hoshen, J. Phys. A **30** (24), 8459-8469 (1997).

[Hoshen 1998] J. Hoshen, Pattern. Recogn. Lett. **19** (7), 575-584 (1998).

[Hughes 1997] D.A. Hughes, Liu, Q., Chrzan, D.C., Hansen, N., Acta Mater. **45** (1) (1997).

[Ilin 2014] D. Ilin, Simulation of hydrogen diffusion in fcc polycrystals: effect of deformation and grain boundaries, PhD thesis, Université de Bordeaux, (2014).

[Instruments] O. Instruments, Electron backscattered diffraction explained.

[Jérôme 2003] M. Jérôme, Interactions hydrogène-métal et perméation électrochimique, « Mémoire d'HdR », Université de Technologie de Compiègne, (2003).

[Jothi 2014] S. Jothi, T.N. Croft, S.G.R. Brown and E.A. de Souza Neto, Composite Structures **108**, 555-564 (2014).

[Kanit 2003] T. Kanit, S. Forest, I. Galliet, V. Mounoury and D. Jeulin, Int. J. Solids Struct. **40** (13), 3647-3679 (2003).

[Katano 2001] G. Katano, K. Ueyama and M. Mori, J. Mater. Sci. **36** (9), 2277-2286 (2001).

[Kaur 1995] I. Kaur, Y. Mishin and W. Gust, *Fundamentals of Grain and Interphase Boundary Diffusion*. (John Wiley & Sons, Chichester, England, 1995).

[Kawamoto 2007] K. Kawamoto, Y. Oda, H. Noguchi, H. Fujii, T. Izumi and G. Itoh, T. Jpn. Soc. Mech. Eng. **73** (731), 788-795 (2007).

[Kirchheim 2007] R. Kirchheim, Acta Mater. **55** (15), 5129-5138 (2007).

[Kirchheim 2010] R. Kirchheim, Scripta Mater. **62** (2), 67-70 (2010).

[Kirchheim 1993] R. Kirchheim, I. Kownacka and S. Filipek, Scripta. Metall. Mater. **28** (10), 1229-1234 (1993).

[Kirchheim 2015] R. Kirchheim, B. Somerday and P. Sofronis, Acta Mater. **99**, 87-98 (2015).

[Kittel 2008] J. Kittel, F. Ropital and J. Pellier, Corrosion **64** (10), 788-799 (2008).

[Kiuchi 1983] K. Kiuchi and R.B. McLellan, Acta Metall. **31** (7), 961-984 (1983).

[Klugkist 2001] P. Klugkist, A.N. Aleshin, W. Lojkowski, L.S. Shvindlerman, W. Gust and E.J. Mittemeijer, Acta Mater. **49** (15), 2941-2949 (2001).

[Knyazeva 2015] A.G. Knyazeva, G.P. Grabovetskaya, I.P. Mishin and I. Sevostianov, Philos. Mag. **95** (19), 2046-2066 (2015).

[Kobayashi 2005] S. Kobayashi, S. Tsurekawa and T. Watanabe, Acta Mater. **53** (4), 1051-1057 (2005).

[Kononenko 2001] O. Kononenko, V. Matveev and D. Field, J. Mater. Res. **16** (07), 2124-2129 (2001).

[Krom 2000] A.M. Krom and A. Bakker, Metall. Mater.Trans. B **31** (6), 1475-1482 (2000).

[Kronberg 1949] F.H.W.a.M.L. Kronberg, Trans. AIME **185**, 501 (1949).

[Kuhn 1991] D.K. Kuhn and H.H. Johnson, Acta Metall. Mater. **39** (11), 2901-2908 (1991).

[Kumar 2000] M. Kumar, W.E. King and A.J. Schwartz, Acta Mater. **48** (9), 2081-2091 (2000).

[Kumnick 1974] A.J. Kumnick and H.H. Johnson, Metall. Trans. **5** (5), 1199-1206 (1974).

[Lacaille 2014] V. Lacaille, C. Morel, E. Feulvarch, G. Kermouche and J.M. Bergheau, Comp. Mater. Sci. **95**, 187-191 (2014).

[Ladna 1987a] B. Ladna and H.K. Birnbaum, Acta Metall. **35** (10), 2537-2542 (1987a).

[Ladna 1987b] B. Ladna and H.K. Birnbaum, Acta Metall. **35** (7), 1775-1778 (1987b).

[Lange 1967] F. Lange, Acta Metall. **15** (2), 311-318 (1967).

[Lassila 1986] D.H. Lassila and H.K. Birnbaum, Acta Metall. **34** (7), 1237-1243 (1986).

[Le Claire 1963] A.D. Le Claire, Brit. J. Appl. Phys. **14** (6), 351-356 (1963).

[Leblond 1983a] J.B. Leblond and D. Dubois, Acta Metall. **31** (10), 1459-1469 (1983a).

[Leblond 1983b] J.B. Leblond and D. Dubois, Acta Metall. **31** (10), 1471-1478 (1983b).

[Legrand 2013a] E. Legrand, Numerical approach of the scale transitions applied to the diffusion and the trapping of hydrogen in metals with heterogeneous structures, PhD thesis, Université de La Rochelle, (2013a).

[Legrand 2012] E. Legrand, J. Bouhattate, X. Feaugas and H. Garmestani, Int. J. Hydrogen Energ. **37** (18), 13574-13582 (2012).

[Legrand 2013b] E. Legrand, J. Bouhattate, X. Feaugas, S. Touzain, H. Garmestani, M. Khaleel and D.S. Li, Comp. Mater. Sci. **71** (0), 1-9 (2013b).

[Lehockey 2004] E. Lehockey, A. Brennenstuhl and I. Thompson, Corros. Sci. **46** (10), 2383-2404 (2004).

[Lehockey 1997] E.M. Lehockey and G. Palumbo, Mater. Sci. Eng. A **237** (2), 168-172 (1997).

[Lejcek 2010] P. Lejcek, *Grain Boundary Segregation in Metals*. (Springer Berlin Heidelberg, 2010).

[Lekbir 2013] C. Lekbir, J. Creus, R. Sabot and X. Feaugas, Mater. Sci. Eng. **578**, 24-34 (2013).

[Levine 1960] H.S. Levine and C.J. MacCallum, J. Appl. Phys. **31** (3), 595-599 (1960).

[Li 2011] M. Li and T. Xu, Prog. Mater. Sci. **56** (6), 864-899 (2011).

[Lienhard 1967] J.H. Lienhard and P.L. Meyer, Quart. Appl. Math. **XXV** (3) (1967).

[Liu 2011] X. Liu, W. Xie, W. Chen and H. Zhang, J. Mater. Res. **26** (21), 2735-2743 (2011).

[Liu 2009] Y.-L. Liu, Y. Zhang, H.-B. Zhou, G.-H. Lu, F. Liu and G.N. Luo, Phys. Rev. B. **79** (17), 172103 (2009).

[Lu 2005] G. Lu and E. Kaxiras, Phys. Rev. Lett. **94** (15), 155501 (2005).

[Ly 2009] C. Ly, Caractérisation d'aciers à très haute limite d'élasticité vis-à-vis de la fragilisation par hydrogène, PhD thesis, École Centrale, (2009).

[Lynch 1988] S.P. Lynch, Acta Metall. **36** (10), 2639-2661 (1988).

[Ma 1993] Q. Ma, C.L. Liu, J.B. Adams and R.W. Balluffi, Acta Metall. Mater. **41** (1), 143-151 (1993).

[Manolatos 1995] P. Manolatos, M. Jerome and J. Galland, Electrochim. Acta **40** (7), 867-871 (1995).

[Marte 1997] C. Marte and R. Kirchheim, Scripta Mater. **37** (8), 1171-1175 (1997).

[Martin 1975] G. Martin and B. Perraillon, Le Journal de Physique Colloques **36** (C4), C4-165-C4-190 (1975).

[McLachlan 1986] D.S. McLachlan, J. Phys. C **19** (9), 1339 (1986).

[McLachlan 1987] D.S. McLachlan, J. Phys. C **20** (7), 865 (1987).

[McLellan 1997] R.B. McLellan and Z.R. Xu, Scripta Mater. **36** (10), 1201-1205 (1997).

[McMahon Jr 2001] C.J. McMahon Jr, Mater. Sci. Eng. **68** (6), 773-788 (2001).

[McNabb 1963] A. McNabb and P.K. Foster, T. Metall. Soc. AIME **227**, 618-627 (1963).

[Mehrer 2007] H. Mehrer, *Diffusion in solids: fundamentals, methods, materials, diffusion-controlled processes*. (Springer, 2007).

[Minich 2002] R. Minich, C. Schuh and M. Kumar, Phys. Rev. B. **66** (5) (2002).

[Mishin 2005] Y. Mishin, in *Diffusion Processes in Advanced Technological Materials*, (Springer Berlin Heidelberg, 2005), pp. 113-171.

[Mishin 1999] Y. Mishin and C. Herzig, Mater. Sci. Eng. **260** (1), 55-71 (1999).

[Miyazawa 1996] K. Miyazawa, Y. Iwasaki, K. Ito and Y. Ishida, Acta Crystallogr. A **52** (6), 787-796 (1996).

[Moody 1991] N.R. Moody and S.M. Foiles, MRS Online Proceedings Library **229**, null-null (1991).

[Morlet 1958] J. Morlet, H. Johanson and A.R. Troiano, J. Iron. Steel. I. **189**, 37-44 (1958).

[Mütschele 1987] T. Mütschele and R. Kirchheim, Scripta Metall. **21** (2), 135-140 (1987).

[Nagumo 2004] M. Nagumo, Mater. Sci. Tech. Ser. **20** (8), 940-950 (2004).

[Ohmisawa 2003] T. Ohmisawa, S. Uchiyama and M. Nagumo, J. Alloy. Compd. **356–357**, 290-294 (2003).

[Oriani 1970] R.A. Oriani, Acta Metall. **18** (1), 147-157 (1970).

[Oriani 1966] R.A. Oriani, Darken, L.S., Z. Physik. Chem. Neue Folge **49**, 271--290 (1966).

[Oriani 1974] R.A. Oriani and P.H. Josephic, Acta Metall. **22** (9), 1065-1074 (1974).

[Oriani 1972] R.A.J. Oriani, P.H. , Scripta Metall. **6**, 681 (1972).

[Oudriss 2012a] A. Oudriss, « Influence des hétérogénéités métallurgiques sur les processus de diffusion et de piégeage de l'hydrogène dans le nickel », PhD thesis, Université de La Rochelle, (2012a).

[Oudriss 2014] A. Oudriss, J. Bouhattate, C. Savall, J. Creus, X. Feaugas, F.A. Martin, . . . J. Chêne, Procedia Mater. Sci. **3**, 2030-2034 (2014).

[Oudriss 2012b] A. Oudriss, J. Creus, J. Bouhattate, E. Conforto, C. Berziou, C. Savall and X. Feaugas, Acta Mater. **60** (19), 6814-6828 (2012b).

[Oudriss 2012c] A. Oudriss, J. Creus, J. Bouhattate, C. Savall, B. Peraudeau and X. Feaugas, Scripta Mater. **66** (1), 37-40 (2012c).

[Palumbo 1990a] G. Palumbo and K.T. Aust, Acta Metall. Mater. **38** (11), 2343-2352 (1990a).

[Palumbo 1991a] G. Palumbo, D.M. Doyle, A.M. El-Sherik, U. Erb and K.T. Aust, Scripta. Metall. Mater. **25** (3), 679-684 (1991a).

[Palumbo 1991b] G. Palumbo, P.J. King, K.T. Aust, U. Erb and P.C. Lichtenberger, Scripta. Metall. Mater. **25** (8), 1775-1780 (1991b).

[Palumbo 1990b] G. Palumbo, S.J. Thorpe and K.T. Aust, Scripta. Metall. Mater. **24** (7), 1347-1350 (1990b).

[Park 2010] Y. Park, J. Lu and G. Rozgonyi, Electronic Materials Letters **6** (1), 1-5 (2010).

[Pedersen 2009] A. Pedersen and H. Jónsson, Acta Mater. **57** (14), 4036-4045 (2009).

[Pressouyre 1979] G.M. Pressouyre, Metall. Trans. A **10** (10), 1571-1573 (1979).

[Pressouyre 1980] G.M. Pressouyre, Acta Metall. **28** (7), 895-911 (1980).

[Priester 2006] L. Priester, *Les joints de grains de la théorie à l'ingénierie* (Edp sciences, 2006), p. 504.

[Priester 2012] L. Priester, *Grain boundaries: from theory to engineering*. (Springer Science & Business Media, 2012).

[Prokoshkina 2013] D. Prokoshkina, V.A. Esin, G. Wilde and S.V. Divinski, Acta Mater. **61** (14), 5188-5197 (2013).

[Pundt 2006] A. Pundt and R. Kirchheim, Ann. Rev. Mater. Res. **36** (1), 555-608 (2006).

[Randle 1999] V. Randle and P. Davies, Interface Science **7** (1), 5-13 (1999).

[Read 1950] W.T. Read and W. Shockley, Phys. Rev. **78** (3), 275-289 (1950).

[Reuss 1929] A. Reuss, J. Appl. Math. Mech. **9**, 49-58 (1929).

[Rohrer 2011] G.S. Rohrer, J. Mater. Sci. **46** (18), 5881-5895 (2011).

[Rohrer 2010] G.S. Rohrer and H.M. Miller, Acta Mater. **58** (10), 3805-3814 (2010).

[Romero 1996] D. Romero, L. Martinez and L. Fionova, Acta Mater. **44** (1), 391-402 (1996).

[Sahal 2004] M. Sahal, J. Creus, R. Sabot and X. Feaugas, Scripta Mater. **51** (9), 869-873 (2004).

[Sahimi 1994] M. Sahimi, *Applications of Percolations Theory*. (Taylor and Francis, 1994).

[Sahimi 2003] M. Sahimi, *Heterogeneous Materials I: Linear transport and optical properties*. (Springer Science & Business Media, 2003).

[Saintier 2011] N. Saintier, T. Awane, J.M. Olive, S. Matsuoka and Y. Murakami, Int. J. Hydrogen Energ. **36** (14), 8630-8640 (2011).

[Schuh 2003a] C.A. Schuh, M. Kumar and W.E. King, Acta Mater. **51** (3), 687-700 (2003a).

[Schuh 2003b] C.A. Schuh, R.W. Minich and M. Kumar, Philos. Mag. **83** (6), 711-726 (2003b).

[Seber 2005] G.A.F. Seber and C.J. Wild, in *Nonlinear Regression*, (John Wiley & Sons, Inc., 2005), pp. 325-365.

[Shimada 2002] M. Shimada, H. Kokawa, Z.J. Wang, Y.S. Sato and I. Karibe, Acta Mater. **50** (9), 2331-2341 (2002).

[Slade 1994] G. Slade, Math. Intelligencer **16** (1), 29-35 (1994).

[Sommer 1989] J. Sommer, C. Herzig, S. Mayer and W. Gust, Defect Diffus. Forum **66-69**, 843 (1989).

[Sørensen 2000] M.R. Sørensen, Y. Mishin and A.F. Voter, Phys. Rev. B. **62** (6), 3658 (2000).

[Stauffer 1994] D. Stauffer and A. Aharony, *Introduction To Percolation Theory*. (Taylor & Francis, 1994).

[Sugimoto 2014] H. Sugimoto and Y. Fukai, Acta Mater. **67**, 418-429 (2014).

[Surholt 1998] T. Surholt, D.A. Molodov and C. Herzig, Acta Mater. **46** (15), 5345-5355 (1998).

[Sutton 1995] A.P. Sutton and R.W. Balluffi, *Interfaces in crystalline materials* (Oxford Science Publishers, 1995), p. 819.

[Suzuki 2003] A. Suzuki and Y. Mishin, Interface Science **11** (1), 131-148 (2003).

[Suzuki 2004] A. Suzuki and Y. Mishin, J. Metas. Nanocryst. Mater. **19**, 1-24 (2004).

[Suzuoka 1961] T. Suzuoka, T. Jpn. I. Met. **2** (1), 25-32 (1961).

[Takai 2002] K. Takai, Y. Chiba, K. Noguchi and A. Nozue, Metall. Mater.Trans. A **33** (8), 2659-2665 (2002).

[Takai 2008] K. Takai, H. Shoda, H. Suzuki and M. Nagumo, Acta Mater. **56** (18), 5158-5167 (2008).

[Taketomi 2008] S. Taketomi, R. Matsumoto and N. Miyazaki, Acta Mater. **56** (15), 3761-3769 (2008).

[Tanabe 1992] T. Tanabe, Y. Yamanishi and S. Imoto, J. Nucl. Mater. **191–194, Part A** (0), 439-443 (1992).

[Thomas 2002] R.S. Thomas, D. Li, R. Gangloff and J. Scully, Metall. Mater.Trans. A **33** (7), 1991-2004 (2002).

[Torquato 2002] S. Torquato, *Random Heterogeneous Materials: Microstructure and Macroscopic Properties* (Springer-Verlag, New-York, 2002).

[Troiano 1960] A.R. Troiano, Trans. ASM. **52**, 54-80 (1960).

[Tsang 2000] I.J. Tsang, I.R. Tsang and D.V. Dyck, Phys. Rev. E **62** (5), 6004-6014 (2000).

[Tsurekawa 2006] S. Tsurekawa, S. Nakamichi and T. Watanabe, Acta Mater. **54** (13), 3617-3626 (2006).

[Tsurekawa 2000] S. Tsurekawa and T. Watanabe, presented at the Mater. Res. Soc. Symp. P., 2000 (unpublished).

[Tsuru 1982] T. Tsuru and R. Latanision, Scripta Metall. **16** (5), 575-578 (1982).

[Voigt 1887] W. Voigt, Abh. Kgl. Ges. Wiss. - Mathematische Classe **36**, 1-100 (1887).

[Wang 2005] H. Wang, W. Yang and A.H.W. Ngan, Scripta Mater. **52** (1), 69-73 (2005).

[Wanner 2010] T. Wanner, E.R. Fuller Jr and D.M. Saylor, Acta Mater. **58** (1), 102-110 (2010).

[Watanabe 1984] T. Watanabe, Res. Mech. **11** (1), 47-84 (1984).

[Watanabe 1994] T. Watanabe, Mater. Sci. Eng. A **176** (1-2), 39-49 (1994).

[Watanabe 1999] T. Watanabe and S. Tsurekawa, Acta Mater. **47** (15–16), 4171-4185 (1999).

[Wells 1989] D.B. Wells, J. Stewart, A.W. Herbert, P.M. Scott and D.E. Williams, Corrosion **45** (8), 649-660 (1989).

[Westlake 1969] D.G. Westlake, T. Metall. Soc. AIME **62**, 1000 (1969).

[Whipple 1954] R.T.P. Whipple, Philos. Mag. Series 7 **45** (371), 1225-1236 (1954).

[Winning 2005] M. Winning and A.D. Rollett, Acta Mater. **53** (10), 2901-2907 (2005).

[Wipf 1997] H. Wipf, in *Hydrogen in Metals III*, (Springer, 1997), pp. 51-91.

[Wipf 2001] H. Wipf, Physica Scripta **2001** (T94), 43 (2001).

[Wolf 1989] D. Wolf and J. Lutsko, Z. kristallogr. **189** (1-4), 239-262 (1989).

[Xu 2009] T. Xu and M. Li, Philos. Mag. **89** (4), 349-374 (2009).

[Yamanishi 1983] Y. Yamanishi, T. Tanabe and S. Imoto, T. Jpn. I. Met. **24** (1), 49-58 (1983).

[Yamaura 2003] S.I. Yamaura, S. Tsurekawa and T. Watanabe, Mater. Trans. **44** (7), 1494-1502 (2003).

[Yao 1988] J. Yao and J.R. Cahoon, Scripta Metall. **22** (11), 1817-1820 (1988).

[Yao 1991] J. Yao and J.R. Cahoon, Acta Metall. Mater. **39** (1), 119-126 (1991).

[Zakroczymski 2006] T. Zakroczymski, Electrochim. Acta **51** (11), 2261-2266 (2006).

[Zhang 2014] P. Zhang, C. Zhang, R. Li and J. Zhao, J. Nucl. Mater. **444** (1–3), 147-152 (2014).

[Zhao 2008] C.W. Zhao, Y.M. Xing, P.C. Bai, J.F. Hou and X.J. Dai, Physica B **403** (10–11), 1838-1842 (2008).

[Zhu 2012a] Z. Zhu and V. Shutthanandan, Surf. Interface Anal. **44** (1), 89-93 (2012a).

[Zhu 2012b] Z. Zhu, V. Shutthanandan and M. Engelhard, Surf. Interface Anal. **44** (2), 232-237 (2012b).

Appendices

Content

Appendix A: Review on the demonstration of 1st order bounds

It is generally impossible to predict the exact analytical solutions of the effective properties for random media of an arbitrary microstructure. However, there are models of homogenization using a theoretical powerful tool to bound the effective properties. These methods are derived using variational principles, which are based on minimizing the power dissipation in the system. In this section, we propose to show that the range of possible effective coefficients is bounded, using the theorem of virtual work, the minimum energy principles and the Hill-Mandel principle. This demonstration is inspired from the book of Auriault which has developed it in a thermal transfer framework **[Auriault 2009]**.

Minimum energy principles

To describe this theory, we consider a mass transport problem at steady state, in a supposed isotropic media. Figure 1 illustrates the problem with the macroscopic boundary conditions. A normal flux boundary condition is applied on Γ_J, while on Γ_J, a constant concentration is applied. The mass transport in a heterogeneous media, with a symmetric definite positive diffusivity tensor **D**(x), is described by:

$$Div\mathbf{J} = 0 \tag{A.1}$$

$$\mathbf{J} = \mathbf{D}\ \mathbf{grad}C \tag{A.2}$$

With boundary conditions in term of concentration and flux, on surfaces:

$$\left[\mathbf{J}\cdot\mathbf{n}\right]_\Gamma = J_n \tag{A.3}$$

$$\left[\mathbf{C}\right]_\Gamma = C_0 \tag{A.4}$$

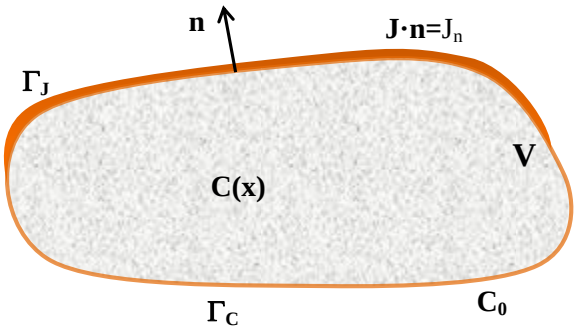

Fig. 1 Problem with the boundary conditions

Let us consider two virtual fields, **J*** and C', satisfying boundary conditions:

$$Div\mathbf{J}^* = 0 \qquad \text{in V} \tag{A.5}$$

$$\left[\mathbf{J}\cdot\mathbf{n}\right]_\Gamma = J_n \qquad \text{on } \Gamma_J \tag{A.6}$$

$$C^{'} = C_0 \qquad \text{on } \Gamma_C \tag{A.7}$$

The **theorem of "virtual work "**says that the dissipated power is equal to the external virtual contributions, which means here:

$$\int_V \mathbf{J}^* \cdot \mathbf{grad}(C^{'})dV = \int_{\Gamma_J} C^{'} J_n dS - \int_{\Gamma_c} C_0 \mathbf{J}^* \cdot \mathbf{n} dS \tag{A.8}$$

In others words, the variation of energy of the system is equal to the developed virtual power of the fields C' and $\mathbf{J}^*$.

Now, the following quadratic form is considered:

$$\Phi(\mathbf{J}^*, C^{'}) = \int_V \frac{1}{2}(\mathbf{J}^* + \mathbf{Dgrad}(C^{'}))\cdot\mathbf{D}^{-1}(\mathbf{J}^* + \mathbf{Dgrad}(C^{'}))dV \tag{A.9}$$

Thus :

$$\Phi(\mathbf{J}^*, C^{'}) \geq 0 \tag{A.10}$$

By developing Φ and using the theorem of virtual work, we can write Φ in the form:

$$\Phi(\mathbf{J}^*, C') = \Phi_1(\mathbf{J}^*) + \Phi_2(C') \tag{A.11}$$

Where:

$$\Phi_1(\mathbf{J}^*) = \int_V \frac{1}{2}\mathbf{J}^* \cdot \mathbf{D}^{-1}\mathbf{J}^* dV + \int_{\Gamma_c} C_0 \mathbf{J}^* \cdot \mathbf{n} dS \tag{A.12}$$

$$\Phi_2(C') = \int_V \mathbf{Dgrad}(C') \cdot \mathbf{grad}(C') dV + \int_{\Gamma_J} C' J_n dS \tag{A.13}$$

The complementary dissipation Φ_1 and the potential dissipation Φ_2 vary independently with J * and C' and their sum is minimal for J and C. Thus, we can easily deduce that the minimum of Φ_1 is reached for **J***=**J** and the minimum of Φ_2 is reached for C'=C:

$$\Phi_1(\mathbf{J}) \leq \Phi_1(\mathbf{J}^*) \tag{A.14}$$

$$\Phi_1(\mathbf{J}) \leq \Phi_1(\mathbf{J}^*) \tag{A.15}$$

The first inequality is called the theorem of the *minimum complementary energy* principle and the second one is called the *minimum potential energy principle*.

Since $\Phi(\mathbf{J}, C) = \Phi_1(\mathbf{J}) + \Phi_2(C) = 0$, for every C' and J*, the *minimum energy principles* yield to the following bounding:

$$-\Phi_2(C') \leq -\Phi_2(C) = \Phi_1(\mathbf{J}) \leq \Phi_1(\mathbf{J}^*) \tag{A.16}$$

Hill principle

The ***Hill principle*** enables us to establish the link between microscopic and macroscopic descriptions. First, the hypothesis (H) states that (i) global variables are the volume average of fluxes and local gradients, and (ii) the balance equations and behavior have the same structure at microscopic and macroscopic scales. Second, the *principle of Hill* requires equality of the energy contained in the medium, whether expressed in local or macroscopic variables defined by (H).

By applying the hypothesis (H), in the current problem, to the dissipated power, expressed in microscopic variables (D, gradC, J) and in macroscopic variables (D_{eff}, <gradC>, <J>), we obtain:

$$\int_V \mathbf{J}\cdot\mathbf{grad}(C)dV = \int_V \mathbf{grad}C\cdot\mathbf{D}\mathbf{grad}CdV = V\left\langle\mathbf{grad}C\right\rangle\cdot\mathbf{D}_{eff}\left\langle\mathbf{grad}C\right\rangle \quad \text{(A.17)}$$

$$\int_V \mathbf{J}\cdot\mathbf{grad}(C)dV = \int_V \mathbf{J}\cdot\mathbf{D}^{-1}\mathbf{J}dV = V\left\langle\mathbf{J}\right\rangle\cdot\mathbf{D}_{eff}^{-1}\left\langle\mathbf{J}\right\rangle \quad \text{(A.18)}$$

Where <·> describes the volume average: $\langle\cdot\rangle = \frac{1}{V}\int_V .\, dV$

1st order bounds: Wiener bounds

Upper bound: Voigt bound

Let us consider the case where a constant concentration C_0 is applied on the entire external surface S, corresponding to a uniform intensity field G, which means:

$$\Gamma_J = \varnothing \qquad \Gamma_C = S \qquad C_0 = \mathbf{G}\cdot x$$

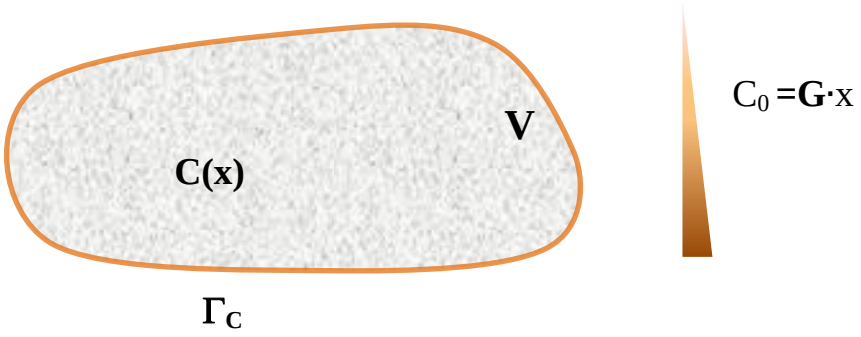

Fig. 2 - Problem with the boundary conditions

It can be shown that the intensity field G satisfies:

$$\left\langle\mathbf{grad}C\right\rangle = \mathbf{G}. \quad \text{(A.19)}$$

Applying the Hill principle and considering the diffusion tensor D_{eff} homogenous and isotropic, we can write the expression of the dissipation:

$$\int_V D\mathbf{grad}(C)\cdot\mathbf{grad}(C)dV = V\ D_{eff}\left\langle\mathbf{grad}C\right\rangle\cdot\left\langle\mathbf{grad}C\right\rangle \quad \text{(A.20)}$$

Now let us consider, a concentration field C' of uniform gradient **grad**C'= <**grad**C>. This field is admissible in concentration, which means:

$C' = \langle \mathbf{grad} C \rangle \cdot x = \mathbf{G} \cdot x$ and thus $C' = C_0$ on *S*.

The field C' satisfies the theorem of *minimum potential energy:*

$$\Phi_2(C) \le \Phi_2(C') \tag{A.21}$$

And given that $\Gamma_J = \emptyset$:

$$\begin{aligned} \int_V D\mathbf{grad}(C) \cdot \mathbf{grad}(C) dV &\le \int_V D\mathbf{grad}(C') \cdot \mathbf{grad}(C') dV \\ &= \int_V D \langle \mathbf{grad}(C) \rangle \cdot \langle \mathbf{grad}(C) \rangle dV \\ &= \langle \mathbf{grad}(C) \rangle \cdot \langle \mathbf{grad}(C) \rangle \int_V D dV \end{aligned} \tag{A.22}$$

By using the Hill principle, we can conclude:

$$V\ D_{eff} \langle \mathbf{grad} C \rangle \cdot \langle \mathbf{grad} C \rangle \le \langle \mathbf{grad}(C) \rangle \cdot \langle \mathbf{grad}(C) \rangle \int_V D dV \tag{A.23}$$

And thus:

$$D_{eff} \le \langle D \rangle \tag{A.24}$$

In other words, the arithmetic mean is the upper bound of Voigt. For a binary composite with homogenous components of respectively volume fractions P_1 and P_2:

$$D_{eff} \le P_1 D_1 + P_2 D_2 \tag{A.25}$$

The Voigt bound is reached for gradC=gradC'=<gradC>.

<u>Lower bound: Reuss bound</u>

Now we consider the case where a uniform flux $\mathbf{J}_0$ is applied on the entire external surface S, which means:

$\Gamma_C = \varnothing$ and $\Gamma_J = S$ $J_n = \mathbf{J}_0 \cdot n$

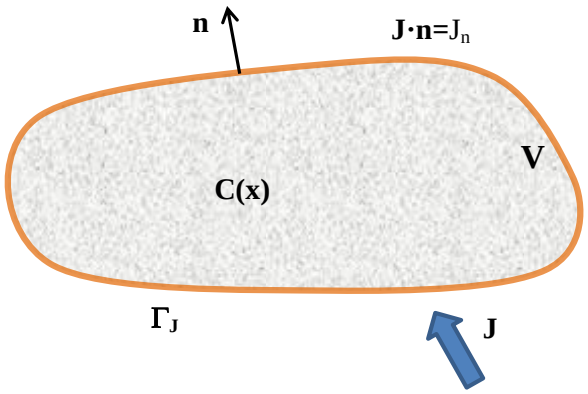

Fig. 3 Problem with the boundary conditions

It can be shown that the average flux in the medium is identical to the applied flux on the surface:

$$\mathbf{J} = <\mathbf{J}> \tag{A.26}$$

Then by applying the Hill principle, and considering the diffusion tensor D_{eff} homogenous and isotropic, we can deduce the expression of the energetic property:

$$\int_V \frac{\mathbf{J}\cdot\mathbf{J}}{D} dV = V \frac{\langle\mathbf{J}\rangle\cdot\langle\mathbf{J}\rangle}{D} \tag{A.27}$$

Now let us consider an admissible field J* defined by J*=<J>. This field satisfies the complementary energy principle:

$$\Phi_1(\mathbf{J}) \le \Phi_1(\mathbf{J}^*) \tag{A.28}$$

And given that $\Gamma_C = \varnothing$:

$$\int_V \frac{\mathbf{J}\cdot\mathbf{J}}{D} dV \le \int_V \frac{\mathbf{J}^*\cdot\mathbf{J}^*}{D} dV = \langle\mathbf{J}\rangle\cdot\langle\mathbf{J}\rangle \int_V \frac{1}{D} dV \tag{A.29}$$

Then by applying the energetic property of J:

$$V\frac{\langle \mathbf{J} \rangle \cdot \langle \mathbf{J} \rangle}{D} \le \langle \mathbf{J} \rangle \cdot \langle \mathbf{J} \rangle \int_V \frac{1}{D} dV \tag{A.30}$$

Thus finally:

$$D_{eff} \ge \left\langle \frac{1}{D} \right\rangle^{-1} \tag{A.31}$$

The geometric mean is the lower bound, called bound of Reuss. In the case of a binary composite, this lower bound is:

$$D_{eff} \ge \frac{D_1 D_2}{P_2 D_1 + P_1 D_2} \tag{A.32}$$

Appendix B: Single inclusion solution

A number of homogenization theories, such the effective medium theory, are based on the solution of the boundary value problem of the relevant field for a single inclusion one phase in a matrix of another phase **[Torquato 2002]**. In this appendix, we will derive single-inclusion solution, in the framework of diffusion. The demonstration was inspired from **[Torquato 2002]**, in analogy of conduction problem.

We consider a spherical inclusion α of radius R with diffusivity D_α placed in an infinite volume V with diffusivity D_{eff}. A uniform concentration gradient with intensity G_0 is applied to all (Fig. 4). A spherical coordinate system (r,θ,φ) is used in this problem with r the position of the vector emanating from the center of the inclusion. The Concentration gradient is carried by the axis $\theta = 0$. Here we propose to determine the induced perturbation ΔC in the concentration field outside the sphere.

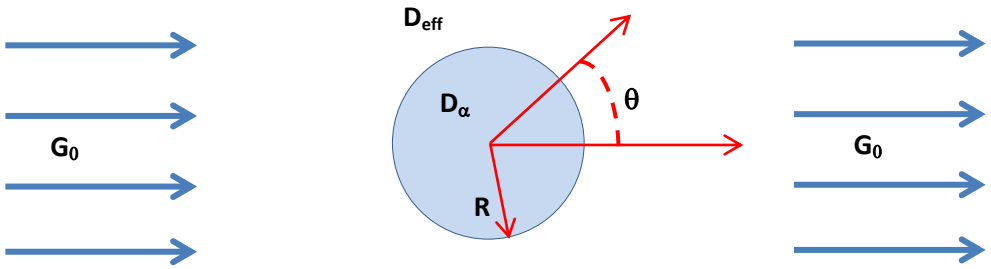

Fig. 4- Schematic of the problem of single inclusion in an infinite matrix

Within and outside the sphere, C must satisfy the Laplace's equation:

$$\Delta C = 0 \tag{B.1}$$

With the boundary conditions:

$$C = C_\alpha \qquad r = R \tag{B.2}$$

$$D^{eff}\,\mathbf{n}\cdot(\nabla \mathrm{C}) = D_\alpha \mathbf{n}\cdot(\nabla \mathrm{C}_\alpha) \qquad r = R \tag{B.3}$$

$$C(r) = -\mathbf{G_0}\cdot\mathbf{r} \qquad r \to \infty \tag{B.4}$$

where C and C_α are the concentrations outside (r>R) the sphere and inside (r<R), respectively.

The Laplace's equation can be solved in three dimensions, using the separation of variables technique (Jackson). The general form of the solution in the matrix can be written as:

$$\begin{aligned} C &= -\mathbf{G_0}\cdot r + A\mathbf{G_0}\cdot\nabla(\frac{1}{r}) \\ &= -G_0 r\cos\theta - AG_0\frac{\cos\theta}{r^2} \end{aligned} \tag{B.5}$$

where A is a constant, θ is the angle between vectors $\mathbf{G_0}$ and $\mathbf{r}$, and $G_0 \equiv |\boldsymbol{G_0}|$. As r →∞, the solution verifies the boundary condition (B.4).

Inside the inclusion, the general form of the solution can be written as:

$$\begin{aligned} C &= -\mathbf{G_0}\cdot r + B\mathbf{G_0}\cdot r \\ &= -G_0 r\cos\theta - BG_0 r\cos\theta \end{aligned} \tag{B.6}$$

where B is a constant.

Using the interfaces continuity conditions in equations (B.5) and (B.6), one can obtain linear equations systems for the unknown constants A and B:

$$C(R) = C_\alpha(R) \quad \Rightarrow \quad A = BR^3 \tag{B.7}$$

$$\begin{aligned} &D^{eff}\,grad(C(R))\cdot e_r = D_\alpha\,grad(C_\alpha(R))\cdot e_r \;\Rightarrow \\ &-D^{eff} + \frac{2AD^{eff}}{R^3} = -D_\alpha + BD_\alpha \end{aligned} \tag{B.8}$$

By solving the system of equations, it yields to:

$$A = -R\frac{D_\alpha - D^{eff}}{D_\alpha + 2D^{eff}} \tag{B.9}$$

$$B = \frac{D_\alpha - D^{eff}}{D_\alpha + 2D^{eff}} \tag{B.10}$$

The substitutions of these relations in equations (B.5) and (B.6) yields to the expressions of the concentration in the matrix and in the inclusion:

$$C = \begin{cases} -\mathbf{G_0}\cdot r + \dfrac{D_\alpha - D^{eff}}{D_\alpha + 2D^{eff}}\mathbf{G_0}\cdot r\left(\dfrac{R}{r}\right)^3, & \text{r} \geq \text{R} \\ -\mathbf{G_0}\cdot r + \dfrac{D_\alpha - D^{eff}}{D_\alpha + 2D^{eff}}\mathbf{G_0}\cdot r\,, & \text{r} \leq \text{R} \end{cases} \tag{B.11}$$

Very far from the inclusion (r→∞), the solution satisfies the boundary condition (B.4). Thus, the solution of the concentration in the matrix can be decomposed into two parts: the uniform concentration field and the induced perturbation ΔC.

$$C = C_0(r) - \frac{D_\alpha - D^{eff}}{D_\alpha + 2D^{eff}} \left(\frac{R}{r} \right)^3 C_0(r) \quad \Rightarrow \quad C = C_0(r) + \Delta C(r) \tag{B.12}$$

As a result, the induced perturbation ΔC is given by:

$$\Delta C(r) = - \frac{D_\alpha - D^{eff}}{D_\alpha + 2D^{eff}} \left(\frac{R}{r} \right)^3 C_0(r) \tag{B.13}$$

Appendix C: Calculation of the diffusivity of the special boundaries

This appendix is aimed at describing how we extracted a diffusion coefficient of the special boundaries from the data of Oudriss *et al*.**[Oudriss 2012]**.

We assumed that the grains phase (G) and the random boundaries (R) form homogenized inclusions of diffusivity $D_{eff}^{R+G} = 2 \times 10^{-12}\ m^2/s$ (figure 5) in a matrix composed of special boundaries (Σ).

We inferred from the effective diffusivity obtained the corresponding sorption curve in Fig. 5, a diffusion coefficient of the special boundaries of D_Σ =3×10^{-16} m²/s., by using the lower Hashin-Shtrikman formula.

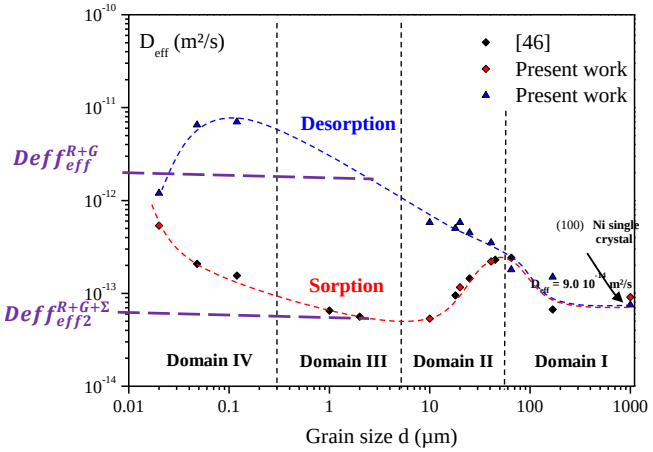

Fig. 5 - Experimental data on the evolution of the effective diffusivity as a function of the grain size, by considering hydrogen charging and desorption[Oudriss 2012]

Table I – Volume fractions of the different phases, at the considered grain size

f_{R+G}	0.9856
f_Σ	0.0164
$Deff_{eff}^{R+G}$	2×10^{-12} m^2/s
$Deff_{eff2}^{R+G+\Sigma}$	5×10^{-14} m^2/s

Lower Hashin-Shtrikman

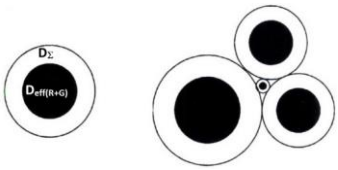

$$Deff_2^{HS-} = D_\Sigma + \frac{f_{R+G}}{\frac{1}{\left(Deff_{eff}^{R+G} - D_\Sigma\right)} + \frac{1 - f_{R+G}}{3D_\Sigma}}$$

$$Deff^{HS-} = 5.1\times10^{-14}\ m^2/s$$
$$with\ D_\Sigma = 3\times10^{-16}\ m^2/s$$

Appendix D: Experimental technics

Electron Back Scattered Diffraction (EBSD)

EBSD technique is used to determine the crystallographic orientation of a polycrystal. This scanning electron microscope (SEM) based technique, also provides information about the grain sizes or the grain-boundary type. In this work, we used this technic mainly to determine the grain-boundary type depending on the crystallographic orientation and to get also a realistic morphology of the grains.

Schematic of the typical EBSD geometry is represented in Fig. 6a. The principle is to direct a beam of electrons on a crystalline sample tilted to 70º from horizontal. Some of the incident electrons arrive at the sample surface with an angle that satisfies the Bragg conditions related to the spacing of the periodic atomic lattice planes of the crystalline structure. These electrons are diffracted and form a pattern that is detected with a fluorescent screen, as schematically described in Fig. 6b.

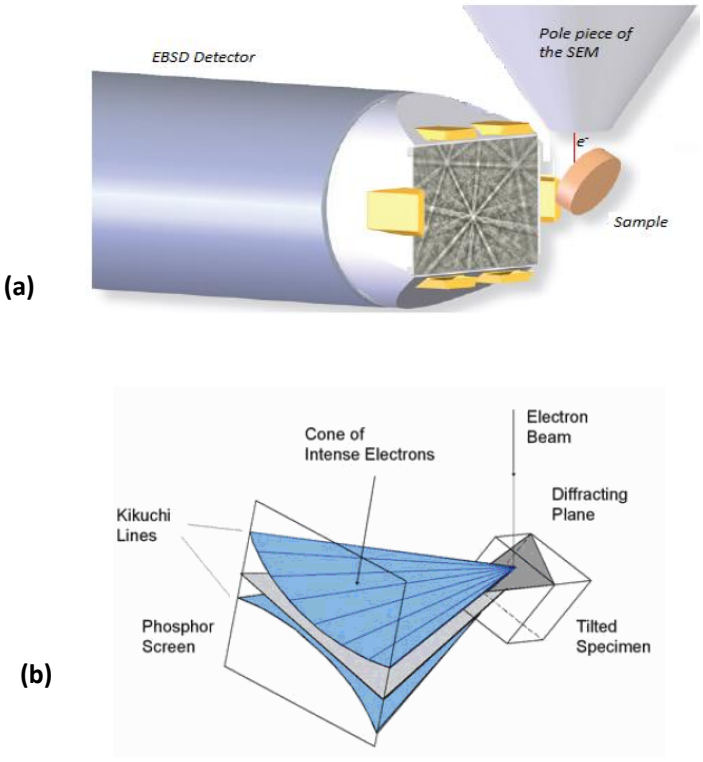

Fig. 6- (a) Schematic of the typical EBSD geometry, showing the pole piece of the SEM, the electron beam, the tilted specimen, and the phosphor screen [Instruments]. (b) Schematic of the diffracting cones with respect to the reflecting plane, the specimen, and the phosphor screen[Schwarzer 2009]

This results in the formation on the screen of several pairs of lines that form the characteristics Kikuchi bands. These bands correspond to the different diffracting crystal planes and each band can be

indexed by the Miller indices of the corresponding plane. This demarche leads to a crystallographic orientation mapping of the sample. The resolution limit of this mapping depends on the fineness of the electron beam and the step size of the scanning. Concerning our analyses, the step size varied between 30 nm and 200 nm depending of type of sample and its grain size. The step size also conditions the acquisition time of an EBSD map.

The sample preparation is a critical step in the achievement of a good EBSD results. A deformation-free surface is an essential condition to obtain good electron backscattered diffraction. In this work, the samples were prepared by SiC surface grinding up to 4000 grade and then electropolished in H_2SO_4/CH_3OH acid solution.

Secondary Ion Mass Spectroscopy (SIMS)

Basically, the principle of SIMS analysis consists in sputtering the surface of a sample and then analyzing the ejected charged particles (Secondary Ions) by mean of mass spectroscopy. A general scheme of the principle of SIMS is shown in Fig. 7. The sample must be solid and stable in a vacuum. The primary ions are usually O^{2+}, O^-, C^{s+}, Ar^+, Ga^+ or neutrals.

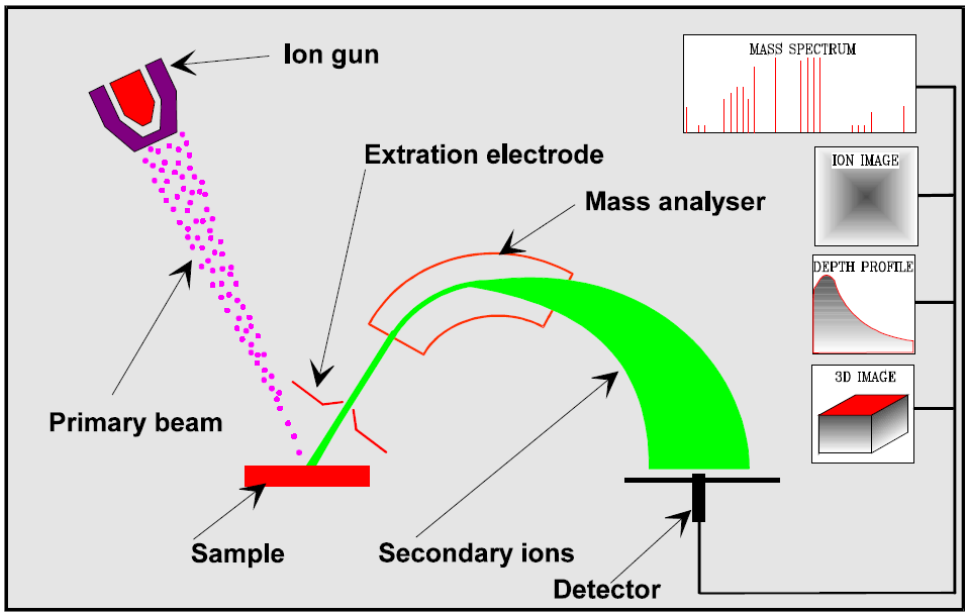

Fig. 7 – Schematic of the typical components of SIMS

Depending on their mass analyzers, SIMS instruments are generally divided into three types: magnetic SIMS, quadrupole SIMS and time-of-flight SIMS. The latter was used in our study. For this

type of SIMS, a Time-of-flight mass spectrometry saves as a function of time the entire spectrum of the ions emitted during a pulse or series of pulses of the primary beam. An ion detection system is then used to record the magnitude of the secondary ion signal. Most modern mass spectrometers combine more than one detector (a channel plate, scintillator and photomultiplier).

The data obtained can be analyzed in different ways. It can be used for depth profiling or surface analysis. In our case, SIMS analyses were performed to evaluate the hydrogen surface distribution.

[Auriault 2009] J.-L. Auriault, C. Boutin and C. Geindreau, *Homogénéisation de phénomènes couplés en milieux hétérogènes : Tome 1, Diffusion et dispersion* 2009).

[Instruments] O. Instruments, Electron backscattered diffraction explained.

[Oudriss 2012] A. Oudriss, J. Creus, J. Bouhattate, E. Conforto, C. Berziou, C. Savall and X. Feaugas, Acta Mater. **60** (19), 6814-6828 (2012).

[Schwarzer 2009] R. Schwarzer, D. Field, B. Adams, M. Kumar and A. Schwartz, in *Electron Backscatter Diffraction in Materials Science*, (Springer US, 2009), pp. 1-20.

[Torquato 2002] S. Torquato, *Random Heterogeneous Materials: Microstructure and Macroscopic Properties* (Springer-Verlag, New-York, 2002).

Modélisation de la diffusion de l'hydrogène dans les matériaux hétérogènes: implications de la connectivité des joints de grains

Résumé :
La diffusion de l'hydrogène dans les métaux est un paramètre clef pour la compréhension des mécanismes de base de la fragilisation par l'hydrogène. Néanmoins, le rôle des joints de grains dans le processus de diffusion de cet élément reste à éclaircir. Avec une approche numérique, nous avons étudié les effets d'un réseau hétérogène de joints de grains sur la diffusivité macroscopique de l'hydrogène. Pour cela, des essais de perméation ont été simulés par la méthode des éléments finis, en modélisant le matériau comme un composite formé d'une phase intra-associée aux grains et deux phases intergranulaires, avec des propriétés de diffusion différentes. Nous avons montré, en caractérisant la topologie et la connectivité du réseau des joints de grains, qu'il existe des fortes corrélations entre les paramètres de connectivité et le coefficient de diffusion effectif. Il a été démontré également que ces corrélations sont plus importantes dans les matériaux nanocristallins. De plus, en utilisant une approche d'homogénéisation, il a été mis en évidence que le coefficient de diffusion effectif est contrôlé par le caractère percolant du réseau des joints de grains, sans pour autant avoir le même seuil de percolation que ces dernies. Une seconde étude, utilisant des microstructures de nickel obtenues par cartographies EBSD, a permis d'évaluer l'écart entre la connectivité des modèles simplifiés et les structures réelles. Cette étude a permis également de confronter les coefficients de diffusion effectifs obtenus par la simulation à des données de la littérature. En parallèle, une étude expérimentale a été conduite sur le nickel pour analyser l'influence des joints de grains sur la distribution locale de l'hydrogène. Les résultats ont montré des corrélations importantes entre la nature du joint de grains et le profil de concentration de l'hydrogène autour de ce joint, qui ne peuvent pas être expliquées uniquement par le processus de diffusion.

Mots clés : joints de grains, hydrogène, connectivité, diffusion, éléments finis, matériaux hétérogènes, homogénéisation.

Modelling of hydrogen diffusion in heterogeneous materials: implications of the grain boundary connectivity

Abstract:
The diffusion of hydrogen in metals is a key factor for understanding the basic mechanisms of hydrogen embrittlement. However, the contribution of grain boundaries to the hydrogen diffusion is not well established. In this this work, we first investigated the effects of a heterogeneous grain boundary networks on the effective diffusivity in polycrystalline materials, using finite elements modeling. To do so, hydrogen diffusion through heterogeneous materials, modeled by a ternary continuum composite media, was simulated. We showed, by characterizing the grain-boundary connectivity, that there are strong correlations between the grain-boundary connectivity parameters and the effective diffusivity. It was found also that these correlations are more significant for nanocrystalline materials. Moreover, by using a homogenization method, it was evidenced that the percolation behavior of the effective diffusivity is controlled by the grain-boundary network evolution, without exhibiting the same percolation threshold than the latter. A second approach, using EBSD-based microstructures, was conducted to evaluate the effect of microstructural constraints on the grain boundary connectivity and to compare the effective diffusivity numerically obtained with experimental data on polycrystalline nickel from literature. In parallel, experimental analyses were performed to analyze the effects of the grain boundaries on the local hydrogen concentration. This highlighted the significant impact of grain-boundary character on the hydrogen distribution around grain boundaries, which can not be explained by the only diffusion process.

Keywords: grain boundaries, hydrogen, connectivity, diffusion, finite elements, heterogeneous materials, homogenization.

Laboratoire des Sciences de l'Ingénieur pour l'Environnement

UMR-CNRS 7356

Bat. Marie-Curie, av. Michel Crépeau

17042 LA ROCHELLE CEDEX